SAPIENZA
UNIVERSITÀ DI ROMA

Sub-GeV Positron Channeling in Silicon Bent Crystal

Facoltà di Scienze Matematiche, Fisiche e Naturali

Corso di Laurea Magistrale in Fisica

Candidate

Davide Annucci
ID number 1746367

Thesis Advisor

Prof. Paolo Valente

Co-Advisors

Prof. Mauro Raggi
Dr. Marco Garattini

Academic Year 2020/2021

Thesis defended on 22/03/2022
in front of a Board of Examiners composed by:

Prof. Vincenzo Marinari (chairman)
Prof. Giacomo Artoni
Prof. Filippo Cesi
Prof. Michele Ortolani
Prof.ssa Annalisa Paolone
Prof. Mauro Papinutto
Prof. Enzo Pascale

Sub-GeV Positron Channeling in Silicon Bent Crystal
Master's thesis. Sapienza – University of Rome

This thesis has been typeset by LaTeX and the Sapthesis class.

Author's email: annucci.1746367@studenti.uniroma1.it

A me!
Questa tesi possa essere un solido punto di inizio
Della mia carriera scientifica da ricercatore

Alla mia famiglia
Che mi ha sempre sostenuto

Ai miei amici
Coi quali condivido il mio interesse per la Fisica

Abstract

In this thesis I will discuss a feasibility study for the SHERPA project. My activity is based on the Geant4 simulations of the bent crystal and the characterization of the detector used as beam-monitor.

In the first chapter I discuss the physics of coherent processes in a bent single crystal. In the second chapter I introduce the DAΦNE complex, the Beam Test Facility and the PADME experiment. Resonant and the Non-Resonant positron extraction are discussed in the third chapter, where the POSEYDON project for DAΦNE is also described. Chapter four describes the simulations of the bent crystal performed in Geant4. Results of tests at SPS and MAMI are used to benchmark the routine. Then the simulation is used to optimize the experimental setup for SHERPA. In chapter five I discuss the TimePix3 detector and its characterization with radioactive sources, as well as the preparatory work done in BTF to operate the detector in a future test-beam. All the key results are summarized in the conclusions.

Acknowledgments

Vorrei ringraziare sinceramente i miei relatori Proff. ***Paolo Valente****,* ***Mauro Raggi*** *(INFN Roma) ed il relatore esterno Dr.* ***Marco Garattini*** *(INFN LNF) per il prezioso supporto che mi hanno offerto durante il corso della mia attività, sia in Sapienza che a Frascati. Con immensa disponibilità, passione e dedizione mi hanno avviato verso un percorso di ricerca che vorrei proseguire in un prossimo futuro. Tramite il continuo confronto reciproco, ho avuto modo di perfezionare le mie conoscenze e metterle in pratica andando a lavorare fisicamente su rivelatori di tipo pixel in silicio (TimePix3). Tali detector sono poi stati utilizzati per caratterizzare il fascio di particelle fornito dal LINAC. Un cordiale ringraziamento va anche a tutti i fisici acceleratoristi e rispettivo staff dipendente, che hanno lavorato sodo per poterci permettere di svolgere tale attività nei tempi previsti. Tra essi,* ***Luca Foggetta*** *mi ha dato l'adeguata formazione in merito alle procedure per operare in sicurezza nella sala sperimentale della Beam Test Facility. Ringrazio la Dr.ssa* ***Clara Taruggi*** *per l'indispensabile aiuto fornitomi nel centrare con precisione il detector sul fascio. Avendo organizzato in maniera efficiente ed ineccepibile l'attività di calibrazione del SAC di PADME, ha permesso di rendermi disponibile uno slot orario di fascio, consentendomi di condurre un test beam importante per la caratterizzazione del TimePix3 il 2 Dicembre.*
Ringrazio anche la Dr.ssa ***Paola Gianotti*** *(INFN LNF), Responsabile locale di PADME; senza la sua approvazione e la sua cordiale disponibilità nulla di tutto ciò sarebbe stato possibile. Ringrazio anche i Drr.* ***Matteo Bauce****,* ***Francesco Collamati*** *ed il Prof.* ***Emanuele Leonardi*** *(INFN Roma) per il prezioso aiuto che ci hanno dato nel capire e sistemare la routine del channeling in Geant4 quando le simulazioni ancora erano in stato embrionale e non funzionavano come ci aspettassimo.*
Ringrazio molto il Prof. ***Marco Vignati*** *(Sapienza) per avermi consigliato di partecipare al bando 22319/2020 INFN RM-1 Concorso per il conferimento di N.5 borse di studio per attività di formazione scientifica per studenti universitari.*
Un cordiale ringraziamento per la cordiale disponibilità e cortesia nell'aiutarmi a portare avanti tutte le pratiche burocratiche va anche al Direttore di Sezione INFN Roma ***Aleandro Nisati*** *e tutto lo staff della Segreteria Amministrativa:* ***Giovanna Vacri*** *e* ***Sonia Mozzillo*** *a Roma;* ***Maria Cristina D'Amato*** *a Frascati.*

Last but not the least... Vorrei ringraziare di cuore gli amici che mi hanno sostenuto e supportato durante questi anni, aiutandomi qualora ne sentissi il bisogno e viceversa. Con voi ho intrecciato la mia carriera accademica, tracciando sentieri per proficue ed importanti eventuali collaborazioni future. Non posso scrivere tutti i vostri nomi su questa lista, siete veramente 'na cifra. I più stretti sono: Carlotta, Chiara, Daniele, Elena, Eleonora, Elisa, Elisabetta, Emanuela, Flavia, Francesco, Gianluca, Giulia, Laura, Lorenzo, Leonardo, Mattia, Michela, Pier, Sara, Sofia, Stefano, Yasmine, Valeria e Valerio.
Questa tesi è dedicata anche a te, Andrea, che non sei più tra noi. Le chiacchierate fuori da Fisica, il caffè prima di affrontare impegnative lezioni o esami alle 8, la tua ironia e simpatia rimarranno indelebili.

Alla mia famiglia, che mi ha sempre sostenuto nelle mie scelte di vita più importanti, dedico questa tesi!

A mio padre
Perché durante questi anni ha vissuto l'università assieme a me. Romani di nascita ma trasferiti altrove, riviviamo ogni giorno il piacere del "rientro a casa Roma" in modo allegro e leggero, preparandoci ad affrontare le nostre giornate impegnative!

A mia madre
Perché durante questi anni mi è sempre stata vicina, sostenendomi in ogni modo e contribuendo al raggiungimento di questo mio traguardo e nuovo punto di partenza!

A mia sorella
Che ogni sera mi aspetta a casa chiedendomi come sia andata la giornata e che in questi ultimi periodi condivide i nostri viaggi con papà! Io ti ho visto crescere e tu mi hai visto progredire lungo questa via di soddisfazioni. Da studentessa universitaria, mi hai fatto vedere le cose da un altro punto di vista e ciò ha contribuito in modo importante alla mia formazione. Grazie!

Ai miei zii, Antonio, Graziella e Paolo; a mia nonna Angela
Che hanno contribuito alla mia formazione mettendosi a disposizione nel momento del bisogno. Vi voglio bene e ricambio di cuore la vostra gentilezza ed il vostro affetto. Grazie a voi non mi è mai mancato nulla, meritate molto!

Ai nonni che non sono più tra noi, Igea, Luigi e Michele
Sempre presenti nei miei pensieri e vicini nelle mie scelte e azioni. A voi dedico un abbraccio grande come il mondo, ricordando i bei momenti trascorsi assieme!

Ai miei zii, Franco e Lucia
Veterani della Sapienza ai tempi del "Vecchio Ordinamento" e laureati eccellenti. Vi ho sentiti vicini durante la preparazione dell'ultimo esame e della tesi. Anche voi avete seguito da vicino il mio percorso accademico, con tutte le gioie e le fatiche che ne derivano!

A voi va il mio più sincero ringraziamento
Il vostro caro Dottore Magistrale

Davide

Contents

Chapter 1

Coherent process in bent single crystal

This chapter aims to briefly introduce the coherent processes a particle can undergo when passing through a single bent crystal.

1.1 Crystal physics and channeling

In a crystalline material the atoms are disposed in an ordered structure, the crystalline lattice (denoted also as Bravais Lattice). In order not to burden the discussion, the interested reader can study the theory underlying Solid State Physics in this book [1], in which Bravais and Reciprocal Lattice are defined, introducing then Miller indices. In this thesis, my interest is focused on the bent Silicon crystal channeling. In its standard, straight configuration, Si atoms are arranged in a "diamond" cubic crystal structure with a lattice parameter (a) of 0.543 nm. The nearest neighbor distance is 0.235 nm. The diamond cubic crystal structure is described by a Face-Centered-Cubic Bravais Lattice with a basis of two silicon atoms, one displaced 1/4 of the bulk diagonal with respect to the other [1]. The Silicon crystal primitive cell is shown in Fig. 1.1.

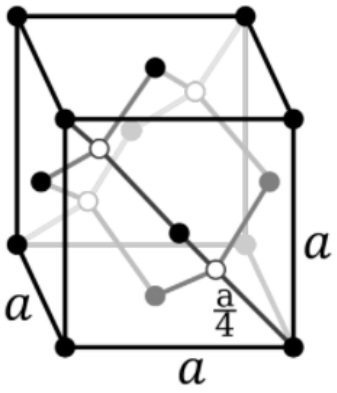

Figure 1.1. Silicon elementary cell. It is a FCC Bravais Lattice with basis.

A family of lattice planes is determined by three integers h, k, and l the Miller

indices. They are denoted (hkl), and each index denotes a plane orthogonal to a direction (h,k,l) in the bases of the Reciprocal Lattice vectors [1]. By convention, negative integers are reported with a slash above. Integers are usually written by reporting the least terms, i.e., the greatest common divisor should be 1. Miller's index (100) represents a plane orthogonal to the h direction, index (010) represents a plane orthogonal to the k direction, and index (001) represents a plane orthogonal to l direction. The Silicon (110) and (111) planes, widely mentioned in this thesis, are represented in Figure 1.2. The silicon crystal with the (110) orientation represents a regular structure with equal distances $d_p = 1.92$ Å between planes. In the crystal with the (111) orientation the large distance $d_p^L = 2.35$ Å between atomic planes changes periodically into a small one d_p^S, where $d_p^L = 3d_p^S$ [7].

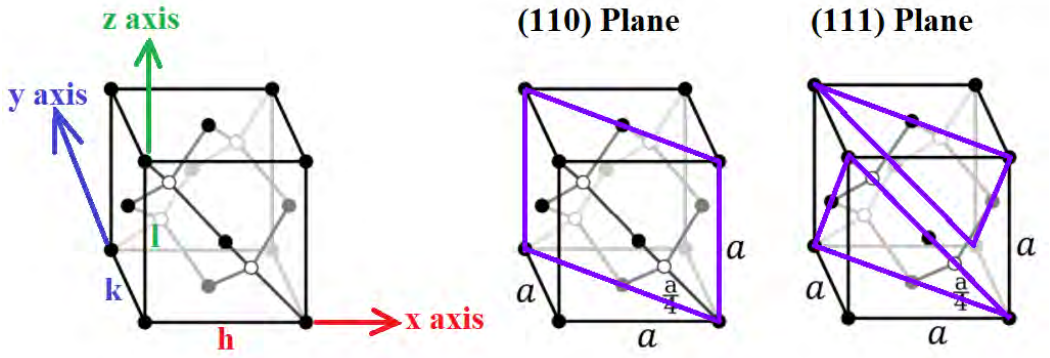

Figure 1.2. Miller indices nomenclature. The (110) and the (111) Si planes are shown.

According to [7], in a crystal the particle moves in a potential that is the sum of the potentials of the single planes (the two nearest atomic layers dominate). Here x is defined already with respect to the mid-plane coordinate between the two atomic planes, and we have defined U(0)=0. Examples of the potential for the (110) and (111) planes of silicon are shown in Fig. 1.3. The harmonic approximation plotted with a dashed line, fits the inter-planar potential rather well, and is often used for analytic estimates.

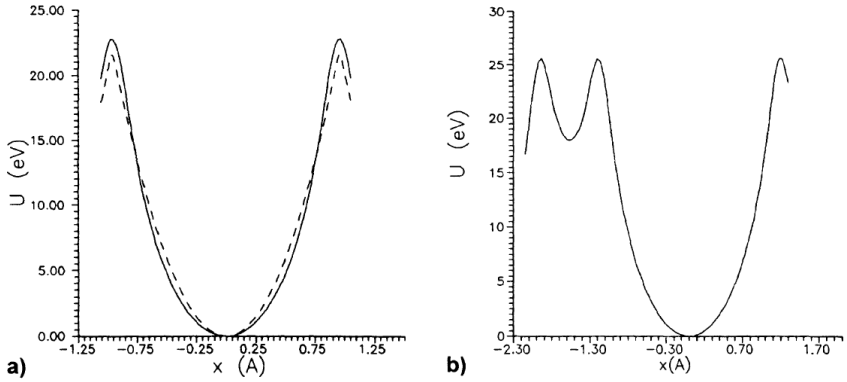

Figure 1.3. The interplanar Moliére potential for (a) the Si channels (110) and (b) the Si channels (111). The dashed line is the harmonic approximation [7].

The process normally used in particle beam steering with a crystal is the so-called Planar Channeling. Also Axial Channeling exists, but it is out of the scope of this thesis. The interested reader can find a rigorous description of Axial Channeling on Ref. [7], which is the reference book consulted in order to write-down this part.

When the transverse component P_x of the particle momentum p is much smaller than the longitudinal component p_z, i.e., the angle $\theta = p_x/p_z$ is small), the law of conservation of the total energy can be rewritten as

$$\frac{p_x^2 c^2}{2E_z} + U(x) + E_z = const \tag{1.1}$$

where $E_z = \sqrt{p_z^2 c^2 + m^2 c^4}$. The sum of the first two terms in (1.1) is called the transverse energy E_T . For motion in the potential $U(x)$. the longitudinal component of the momentum is conserved, implying the conservation of E_T.

$$E_T = \frac{p_x^2 c^2}{2E_z} + U(x) = \frac{p_z^2 c^2 \theta^2}{2E_z} + U(x) = const \tag{1.2}$$

Assuming $E_z \sim E$, $p_z \sim p$ and using the relation $pc^2 = vE$, where v is the particle velocity, it is possible to rewrite the (1.2) as

$$\frac{pv}{2}\theta^2 + U(x) = const \tag{1.3}$$

The particle trajectory for an arbitrary $U(x)$ may be obtained by integration of the expression

$$dz = \frac{dx}{\sqrt{\frac{2}{pv}(E_T - U(x))}} \tag{1.4}$$

that follows directly from the (1.3). Differentiating eq. (1.2) with respect to z, taking into account that $\theta = dx/dz$, and using the same substitutions, it can be obtained

$$pv\frac{d^2x}{dz^2} + U'(x) = 0 \tag{1.5}$$

For the one-dimensional transverse motion in the potential $U(x)$. It describes the particle oscillation in the potential well of the planar channel. In the harmonic potential given by

$$U_h(x) = U_0\left(\frac{2x}{d_p}\right)^2 \tag{1.6}$$

the solution of eq. (1.5) is a sinusoidal oscillation:

$$x = \frac{d_p}{2}\sqrt{\frac{E_T}{U_0}}sin\left(\frac{2\pi z}{\lambda} + \phi\right) \tag{1.7}$$

$$\theta = \sqrt{\frac{2E_T}{pv}}cos\left(\frac{2\pi z}{\lambda} + \phi\right) \tag{1.8}$$

with

$$\lambda = \pi d_p\sqrt{\frac{pv}{2U_0}} \tag{1.9}$$

The condition for the capture of the particle into the Channeling mode is

$$\frac{E_0\theta^2}{2} + U(x) \leq U_0 \tag{1.10}$$

where E_0 is the particle energy, $U(x)$ is the potential function, and $\theta < \theta_c$ is the incident particle angle with respect to the z axis. The critical angle, denoted also as Lindhard angle, is defined as the maximum angle that an impinging particle can assume in order to undergo planar Channeling and can be calculated as follows.

$$\theta_c = \sqrt{\frac{2U}{E_0}} \tag{1.11}$$

In order to keep simple the description, let's focus on a perfect straight crystal. Such atomic configuration doesn't show dislocations, missing atoms or other imperfections. A lattice can be thought as a "grid" of ordered atoms. The straight crystal presents an uniform atomic density and thus its potential wells share the same height. If the crystal is bent, the atomic density in no more uniform: a region will become more densely populated, because the mean inter-atomic distance will be shorter; meanwhile at the opposite side of the crystal, the inter-atomic distance will increase due to the strain induced by the crystal bending. This induced unbalancing in the atomic density leads to a different conformation of the potential wells. This effect of crystal bending is shown in Fig. 1.4, where is clearly evident that the two maxima of the potential in the straight configuration assume different values in the bent configuration. In the depicted case, the left maximum decreases its energy and the right maximum increases its energy due to the centrifugal force induced by the bending.

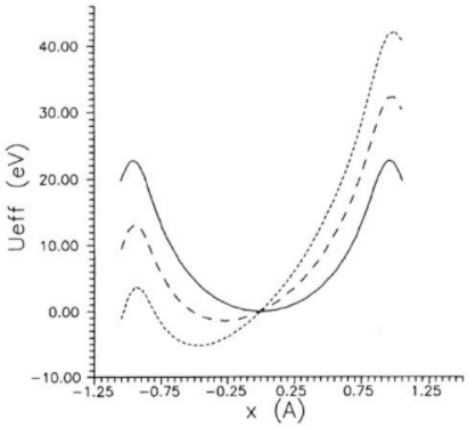

Figure 1.4. The straight crystal potential is indicated with a solid line. The effect of crystal bending manifests as a symmetry-breaking in the $U_{eff}(x)$. The dashed line indicates a centrifugal force contribution of $pv/R = 1$ GeV; the dotted line is for a $pv/R = 2$ GeV contribution.

In this case, the effective potential becomes

$$U_{eff} = U(x) + \frac{pv}{R} \tag{1.12}$$

In order to induce the crystal bending, an holder is used to clamp the crystal. The microscopical shape of the holder clamps induce a strain on a side of the crystal and thus it assumes the configuration depicted in Fig. 1.5.

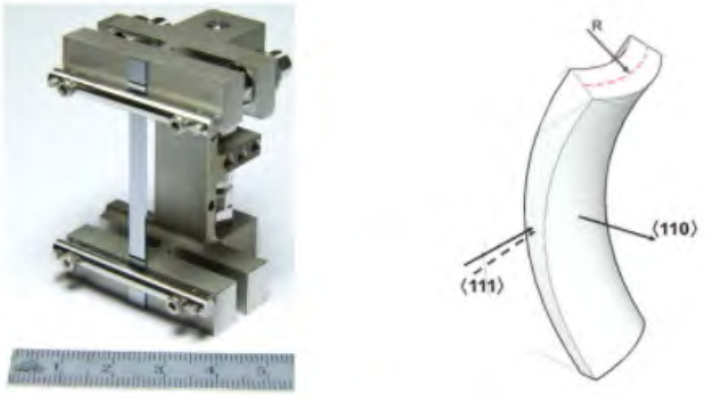

Figure 1.5. (Left): A typical crystal holder used for High-Energy Channeling applications at SPS [16]. (Right): Schematic picture of a silicon strip crystal with anticlastic curvature along the (110) planes [17].

1.1.1 Planar Channeling

In order to achieve Channeling, it is necessary to apply a mechanical stress on a crystal. This bending is induced by the holder clamps geometry, as reported earlier. A schematic picture of a bent crystal is given in Fig. 1.6, where the lattice planes and the bending angle are shown. R is the bending radius, w and l are the crystal thickness and length.

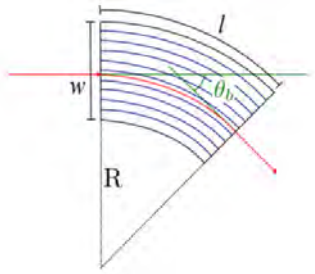

Figure 1.6. Bent crystal Channeling. The Channeling bending angle, θ_b is indicated in green. Reproduced from [16].

In order to not induce defects on the crystalline lattice, the bending radius must be much bigger than the crystal thickness ($R \gg w$), otherwise there can be the presence of dislocations, missing atoms or other imperfection. In this thesis this condition always holds true.
While bending the crystal, the atomic density unbalancing modify the potential barrier as depicted in Fig. 1.4.
A particle impinging the crystal with an angle $\theta < \theta_c$ (where θ_c is the Lindhard

angle yet defined in Eq. 1.11) can undergo Planar Channeling.
Once channeled, a particle follows the bent crystal channel trajectory, oscillating according to the 1.5, where the $U(x)$ is replaced with the new $U_{eff}(x)$. In order not to burden this work, all the further calculations will be skipped. The interested reader can take as a reference the usual [7, 16].

A particle impinging on a crystal with a specific direction, i.e. parallel to the vector of the Reciprocal Lattice described by the Miller Indices (hkl), will be trapped by the strong interplanar electrostatic field, thus undergoing planar Channeling. Channeled particles oscillate between the lattice planes until some other coherent processes described in this Chapter become eventually dominant.
Under channeling conditions positive particles penetrate deeper into the crystal relative to the un-aligned orientation because the trajectory is repelled from the nuclei. On the other hand, negative particles interact more frequently because of their attraction to zones with high densities of nuclei [2].

1.1.2 Dechanneling, Rechanneling and Volume Capture

While a channeled particle approaches to the lattice plane due to its oscillation around the minimal-potential trajectory, it can interact with the atoms of the crystalline lattice, and this causes non-conservation of the transverse energy E_T. If the channeled particle goes too close to an atom of the lattice plane it can undergo Multiple Scattering or other incoherent processes, gaining straightforwardly a little quantity of energy that is sufficient to overcome the potential well heigth. As illustrated in Fig. 1.7, if the the particle energy is enough to overcome the potential barrier U_b^{max}, it can escape the crystal channel, undergoing Dechanneling.
The coherent process of Dechanneling manifests as well in straight and bent crystals, as depicted in the top two Subfigures of Fig. 1.7.

Due to these considerations, the dechanneled particles will be deflected by a smaller angle than the channeling deflection angle of the crystal θ_c. Assuming the Dechanneling to be a coherent process with a decreasing exponential distribution, the number of dechanneled particles as a function of the crystal depth $N_{Dech}(z)$ will take the form:

$$N_{Dech}(z) = N_0 \cdot exp(-\tfrac{z}{L_D})$$

where N_0 is the initial number of channeled particle, z is path travelled by the particle into the crystal and L_D is the Dechanneling Length, defined in [7].

In particular conditions, a dechanneled particle can re-enter the channel; this process is called Rechanneling. In some cases the particles oscillating close to the lattice planes can undergo multiple Dechanneling and Rechanneling cycles and this effect is crucial when studying low energy leptons. In order to reinforce this statement, is important to recall the Figure 4.10(a), reproduced from Ref. [14]. In that plot is evident that for low energy electrons the Rechanneling gives a substantial contribution to the Channeling efficiency.

Another interesting coherent process that can occour in a bent crystal is the Volume Capture. As reported earlier, Dechanneling occours when an oscillating particle interact with an atom of the lattice planes, undergoes incoherent scattering

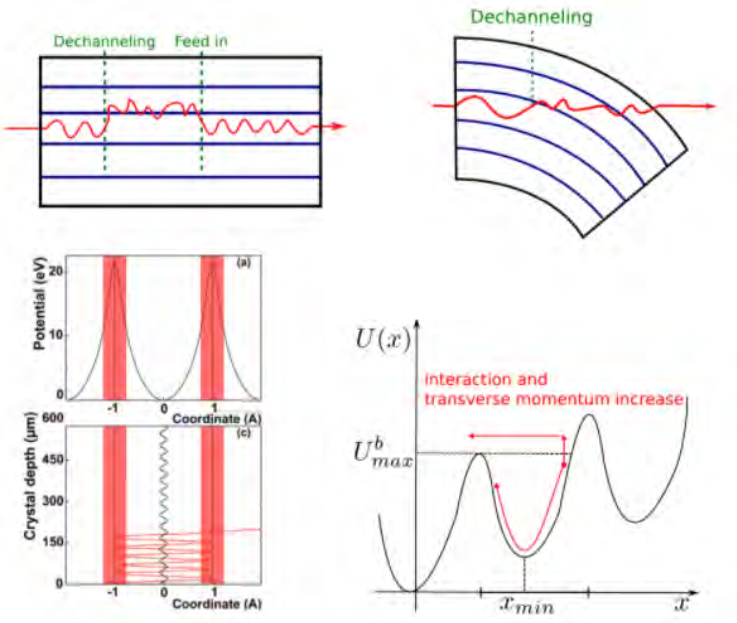

Figure 1.7. Particle Dechanneling in (Top Left) a straight crystal and (Top Right) a bent crystal. (Bottom Left) Dechanneling can happen as the channeled particle approaches the lattice planes and (Bottom Right) if a particle oscillating in the channel gains an energy sufficient to overcome the potential barrier, it can exit the Channeling condition.

phenomena and gains an energy sufficient for escaping the potential well. Volume Capture is someway the "inverse" process: a particle impinging the crystal with an impact angle $\theta > \theta_c$ can interact with an atom of the lattice plane, decreasing its energy and being subsequently trapped in a crystal channel. The bent crystal is aligned with respect to the incoming particle beam in such a way that the beam trajectory becomes tangent to the atomic planes inside the crystal. The comparison between Dechanneling and Volume Capture is reported in Fig. 1.8.

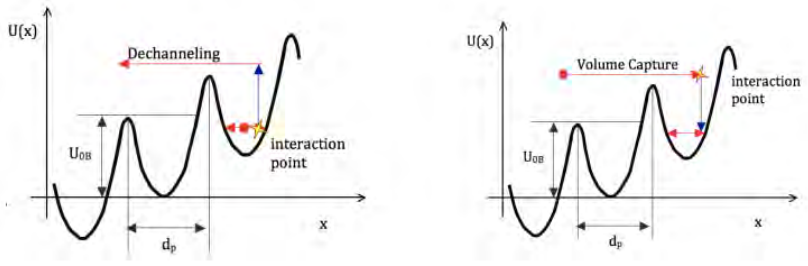

Figure 1.8. Comparison of two coherent processes: (Left) Dechanneling and (Right) Volume Capture.

1.1.3 Volume Reflection

Not all particles impinging the crystal with an impact angle $\theta > \theta_c$ can undergo Volume Capture. If the particle is "mirrored" with respect to the tangent line at the interaction point with the crystal, they can undergo Volume Reflection. Whereas the Volume-Captured particles interaction is not at the boundary of the potential well, the Volume Reflection consists essentially of an almost-elastic scattering of the particle by the lattice plane; in this case the deflection is opposite to the crystal bending and the exit angle is negative. Also in this case, the bent crystal is aligned with respect to the incoming particle beam in such a way that the beam trajectory becomes tangent to the atomic planes inside the crystal. The comparison between Volume Capture and Volume Reflection is depicted in Fig. 1.9.

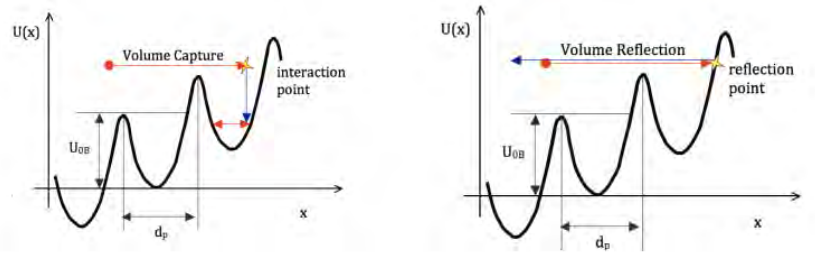

Figure 1.9. Comparison of two coherent processes: (Left) Volume Capture and (Right) Volume Reflection.

Particles undergoing Volume Reflection have a higher probability to interact with lattice nuclei, as they cross atomic planes. The Volume Reflection deflection angle is obviously lower than the Channeling bending angle, because the particles cannot exploit the full-channel length path.

1.1.4 Amorphous behavior

A particle impinging on a bent crystal in the wrong direction, i.e., not aligned with the reciprocal vector of the lattice described by Miller's indices h, k, l, does not perceive the electrostatic field generated by the crystalline channels. In this case, the crystal behaves as an amorphous material and the angular distribution of the deflected particles is the Multiple Scattering distribution. According to PDG, at lowest order this distribution is gaussian, with expectation value equal to zero and RMS MS deflection angle given by the following [20]:

$$\theta_0^{MS} = \frac{13.6\ MeV}{\beta cp} \cdot \sqrt{\frac{x}{X_0}}$$

where $X_0 = 9.7$ cm is the Si radiation length, $p = \sqrt{E^2 - m^2}$ and $c = 1$ in natural units.

1.1.5 High Energy Hadrons VS Low Energy Leptons

Due to their intrinsic rigidity, high energy hadrons show a more penetrative power than low energy leptons. This is also due to the conformation of such particles: hadrons (for example, protons used at SPS) are composite particles, made up of quarks; leptons, instead, are point-like particles. Proton mass exceed electron mass by ∼2000 times ($m_p \sim 1$ GeV, $m_e \sim 0.500$ MeV). The bent crystals suitable for high-energy purposes present a Bending Radius much greater than their low energy counterparts; because high energy particles will be less deflected than low energy ones. Moreover, the crystal depth is bigger in case of high energy applications. Due to these simple considerations, a crystal designed for Multi-GeV application shows a tiny deflection angle (i.e. 50 μrad for the H8 SPS crystal used in Ref. [17]) with respect to a crystal designed for Sub-GeV application (i.e. 910 μrad for the H8 SPS crystal used in Ref. [17]).

1.1.6 Positive VS Negative particles

As reported before, under channeling conditions positive particles penetrate deeper into the crystal relative to the un-aligned orientation because the trajectory is repelled from the nuclei. On the other hand, negative particles interact more frequently because of their attraction to zones with high densities of nuclei [2]. This different behaviour of positive and negative particles has important consequences and drawbacks while considering the coherent processes the particles themselves could undergo in the crystal.

In Figure 1.10, reproduced from [2], there are reported some interesting features of the Geant4 simulation, further described in Chapter 4. I decided to report them in this Chapter because the Geant4 routine documentation describes quite well the Channeling in the case of positive particles (red lines in the Figure) and negative particles (blue lines).
In the top panels, four condition are repersented.

- Curve 1 and 2: Channeled positive and negative particle trajectory in the crystal. The particles are channeled in the lattice planes because they are catched by the electrostatic field and their energy is less than the maximum of the $U(x)$.
- Curve 3 and 4: Overbarrier positive and negative particle trajectory in the crystal. Those particles feel the electrostatic field generated by the lattice planes of the crystal, but aren't trapped in the potential wells because their energy is higher than the potential computed at the lattice plane position.

For positive particles, the Channeling condition is satisfied for a large fraction of particles. The channeled particles usually will reach the endpoint of the channel, thus Dechanneling is strongly suppressed. Rechanneling is almost not present, due to the almost-lack of Dechanneling. Volume Reflection and Volume Capture can manifest as well.
On the other hand, for negative particle it is easier to escape the Channeling condition, due to the different conformation of the interatomic potential. Dechanneling and

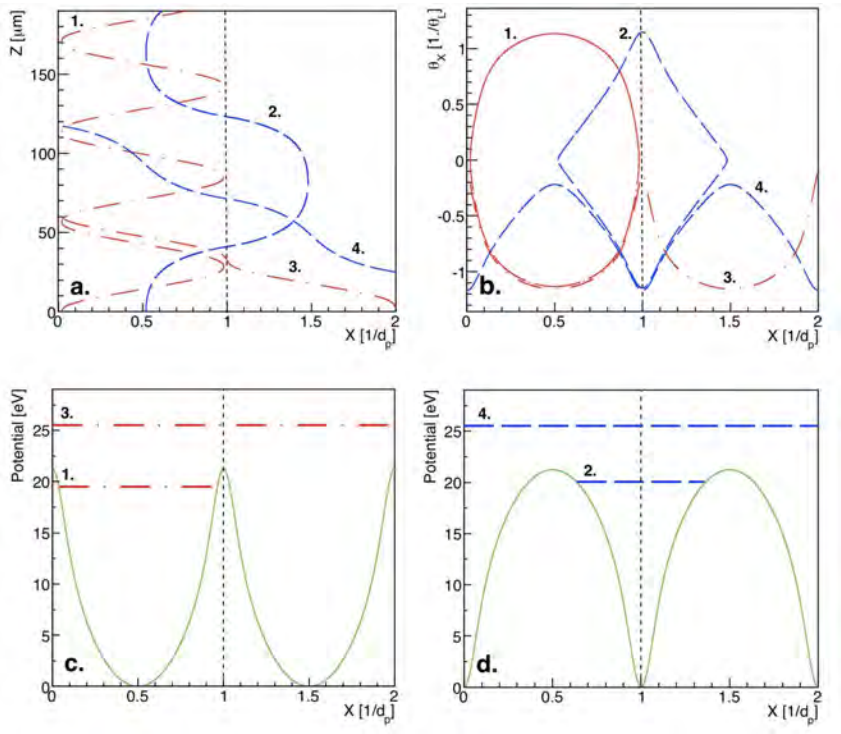

Figure 1.10. 400GeV particles interacting with Si (110) planes (dotted lines). Curves 1 and 2 refer to channeled particles while curves 3 and 4 refer to overbarrier particles. Dashed (dot-dashed) lines represent negative (positive) particles. (a) Trajectories as a function of transverse position (X) and penetration depth (Z). (b) Trajectories as a function of transverse position (X) and transverse angle (θ_x). Continuum planar potential (continuous line) and transverse energies for (c) positive and (d) negative particles.

Rechanneling are more frequent; it is possible also to have multiple-times Dechanneling/Rechanneling alternations, as reported ealier, in Subsec. 1.1.2. Volume Capture is a very efficient process, and this will be clearly visible when introducing the Geant4 simulations in Chapter 4.

Chapter 2

LNF accelerators complex

The DAΦNE double-ring collider in Frascati National Laboratory (LNF) is designed in order to run at the Φ meson resonance center of mass energy of ∼1 GeV. The layout of the complex, including facilities like synchrotron radiation laboratories and beam-test is shown in Fig 2.1, and will be described in this chapter.
One possibility for extending the life of such a precious machine would be to use the stored electrons (or positrons, as in the case of the CESR storage ring at the Cornell University) for producing synchrotron light. However, the availability of a rare resource like a high quality positrons and electrons beam also opens new research opportunities [19].

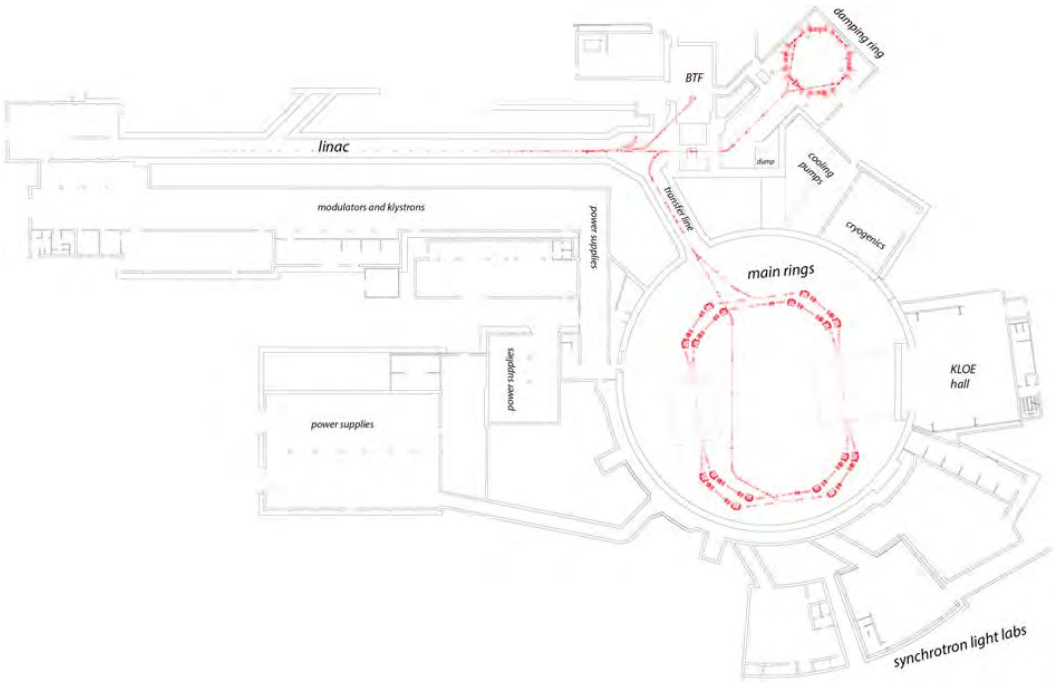

Figure 2.1. The LNF DAΦNE accelerator complex layout.

Ultra-relativistic positron (≫ MeV) are generally produced by high-current electron Radio-Frequency (RF) LINAC's, with repetition rate up to hundred Hz, and beam pulse duration in a very wide range, from below ps (in the case of photo-

injectors) up to few μs range (in case of thermoionic guns and uncompressed RF power); charge usually ranges from pC to few nC per pulse. Positrons are generally produced by Bremsstrahlung onto high-Z targets with a very high emittance, and then focused by strong magnetic fields; this methods is succesfully used at LNF. An alternative production method is by means of the intense photon flux generated by electrons in an undulator. The relatively short number of accelerators running with positrons is further reduced when considering externally extracted beams, either directly from the LINAC or from the storage ring.

2.1 Electron-positron LINAC

Linear or circular accelerators can be classified according to the Radio-Frequency used to accelerate particles. Today, as in the '40s - '50s, the accelerator band naming complies with the nomenclature initially used to distinguish the different radar operative frequencies ranges. The most used bands for particle accelerators are the following, reported in Table 2.1. S-, C- and X-Bands are widely used in accelerators.

Band name	Frequency [GHz]	Wavelength [cm]
L	1 - 2	30 - 15
S	2 - 4	15 - 7.5
C	4 - 8	7,5 - 3,75
X	8 - 12	3,75 - 2,5
K	18 - 24	1.67 - 1.11

Table 2.1. Some of the Radar and LINAC frequency bands.

The injector of the DAΦNE accelerator complex is an S-Band 2856 MHz LINAC that alternately produces and accelerates the electron and positron beams up to the collider operation energy of 510 MeV.

The triode thermoionic gun working principle is based on the emission of electrons by a heated metallic wire. This gun typology is suitable for high-current applications, while for low emittance other gun types are preferred, i.e. photoinjectors. The thermoionic electron gun emittance depends on the accelerating field applied just downstream the heated wire. The LNF electron source cathode and power supply are shown in Figure 2.2 and a more complete description of the electron gun can be found in Ref. [9].

The electric field between the electrodes cannot be arbitrarily high because if the potential difference is greater than the threshold value, the electrons of the electrodes can be torn off by the electric field generated between the electrodes, damaging them irreparably.

The field gradient in the accelerating sections of the LINAC is limited to max 17 MV/m. This value is not so high if compared to C- or X-Band accelerators field gradients (that can be higher than a S-Band accelerator field gradient by approx. a magnitude order). The maximum energy reached by the particles when accelerated depends on the field gradient: in order to increase the particle energy (without

Figure 2.2. On the left: Electron Gun cathode. On the right: Gun High Voltage power supply.

increasing the accelerator length), it is necessary to put a SLED (SLAC Energy Doubler Device) between the Klystrons and the accelerating cavities. More details will be given further, in this chapter, when speaking about RF power distribution.

In the DAΦNE LINAC, positrons are produced by striking ∼5.5 A, ∼200 MeV electrons on a ∼2-radiation lengths 75:25% Tungsten-Rhenium target (positron converter, see Fig. 2.3). Electrons are produced by the thermoionic gun, bunched (prebuncher and buncher cavities, PB and B in Fig. 2.3), and accelerated in the first five accelerating sections (E1-E5). Downstream of the converter, strong solenoids collect emitted positrons, which are captured by a high-gradient section (capture section, CS), followed by a standard one (P1), and are then separated from electrons by a four-dipoles achromatic bump. Half of the RF power, provided by two modulators and 45 MWp klystrons is used in this first half of the LINAC. The remaining 8 accelerating sections, fed by two additional RF stations (identical the former ones), bring positrons to a maximum energy of 530-550 MeV. Typically, with 10 ns long pulses, up to 1 nC charge is produced [19].

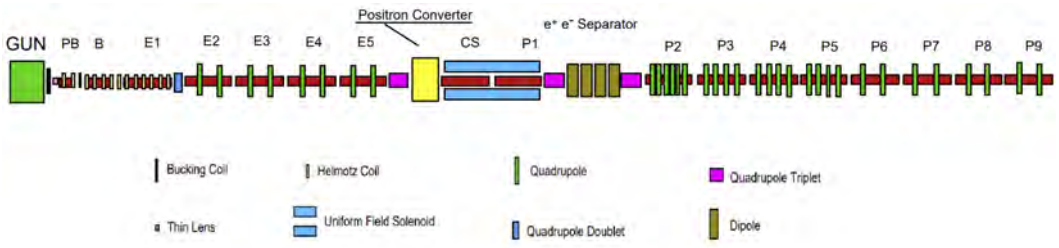

Figure 2.3. Scheme of the DAΦNE LINAC and focussing system.

Alternatively, positrons can be also produced in the Beam-Test Facility (BTF) transfer line, by selecting positive secondary particles emerging from the beam-attenuating target. Electrons or positrons pulses from the LINAC can be diverted to the BTF line by means of a pulsed 3° dipole; during standard running of the collider, all LINAC pulses not used for injection in the DAΦNE rings are available for the BTF (excluding pulses used for monitoring purposes, once or twice per second). In this case the energy of the positrons can be adjusted (by means of a dipole and a collimator system) from the primary LINAC energy down to few tens of MeV, but a

significantly lower intensity beam can be produced (from "single particle" regime to $10^6/s$, depending on the energy). The layout of the transfer-lines for delivering electrons and positrons from the LINAC to the BTF and to DAΦNE rings is shown in Fig. 2.4

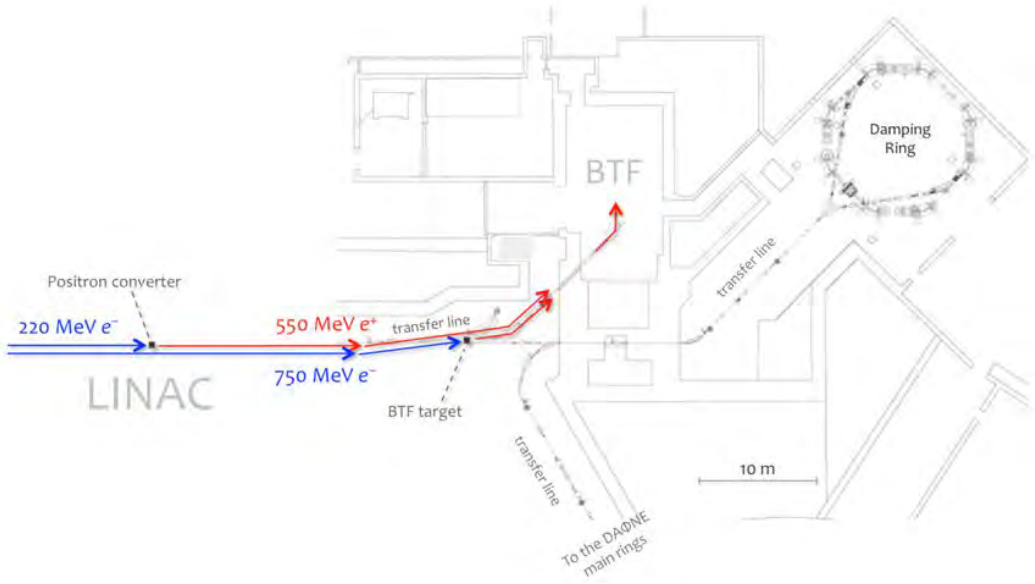

Figure 2.4. The BTF transfer line and the two possible positron beams: LINAC primary positrons from the converter, or secondary beam from the BTF target.

The 3° pulsed dipole is not meant only to direct leptons towards the BTF. This magnet can switch the leptons to three different lines, as visible in Figure 2.5.

- The first line goes towards a spectrometer magnet, used in order to characterize the beam energy.
- The second line goes towards the DHSTB001 dipole magnet and thus towards the Beam Test Facility. This line feds the PADME experiment and is used also for beam diagnostics. Just few meters before PADME, a new dipole has been installed and the BTF line splits in two sections: the original BTF and a new line BTF-II.
- The third line goes towards the Damping Ring. While performing DAΦNE operations the beam must pass through this intermediate ring because the positron production rate is much less than the electron-on-target rate.

The DAΦNE LINAC RF power distribution is schematized in Figure 2.6. A 2856 MHz S-Band Radio-Frequency Source signal is amplified with a RF Amplifier. After that, the electromagnetic wave power is amplified by a Klystron. It work exactly as particle accelerators (but LINACS use Radio-Frequencies to accelerate the leptons, in the Klystrons the electrons stream amplifies the RF wave that will then be used to fed the LINAC RF Cavities). In the Klystron, a stream of electrons are emitted via thermoionic effect, accelerated and bunched. This bunch movement generates a Radio-Frequency electromagnetic wave travelling synchronously with the beam, so a

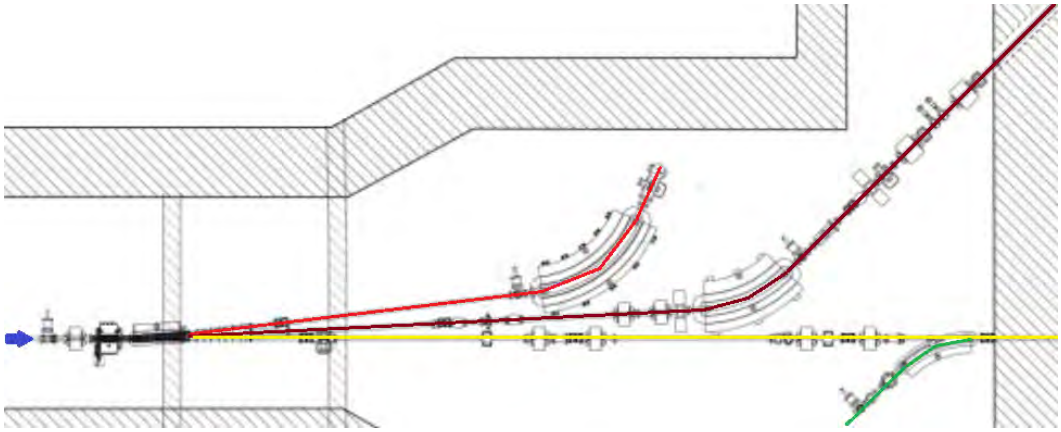

Figure 2.5. Transfer lines layout downstream the last accelerating section. Electrons (or positrons) pass through the 3°pulsed dipole magnet. In red, the transfer line of the spectrometer magnet. In bordeaux, the Beam Test Facility transfer line. If the pulsed dipole is kept off, the leptons are transported to the Damping ring, not visible in this figure, via the yellow transfer line. After re-circulation in the DR, the leptons can be transported to DAΦNE via the green line.

RF wave guide is built around the vacuum tube of the Klystron.

The LINAC length is limited by the dimensions of the structure in which it is operating. Moreover, the peak gradient achievable in S-Band accelerators are relatively low if compared to the typical values of gradient proper of other band type accelerators: the maximum gradient achievable for an S-Band LINAC is ∼17 Mv/m. Due to those limitations, the only way to further amplify the accelerating field is to put an appropriate device, the SLED.
In order to amplify the output power of the Klystrons, doubling the Energy, after each one of them there is a SLAC Energy Doubler Device (SLED). It is essentially a H-shaped RF wave guide with two extremity closed in such a way to reflect back the electromagnetic wave. The input electromagnetic wave is split in two components, each going towards a reflector. The path difference allows a recombination at the output flange in such a way to have a 90° phase shift, and so, constructive interference. The signal outgoing from the SLAC is driven directly towards the accelerating resonant cavities and thus particles can be accelerated. Each Klystrons fed 4 RF cavities and gives them a global power suitable to induce a 250 MeV energy gain (along the whole 4 RF cavities stack). It is important to remark that Klystron A fed the prebuncher and the buncher, so the 4-section 250 MeV energy kick is not fully exploited.

The LINAC can operate in different modes. When LINAC operates in electron mode, all the 4 accelerating sections are used and the particles can reach an energy up to 800 MeV with a beam current of 150 mA (peak). In this configuration the Positron Converted is not inserted. When LINAC operates in positron mode, the first accelerating section gives an energy of 250 MeV to the electrons. After this pre-acceleration the particles undergo Bremsstrahlung on the $2X_0$ 75:25% Tungsten-Rhenium target; if the energy of the radiated photon is greater than $2m_e$ (where m_e

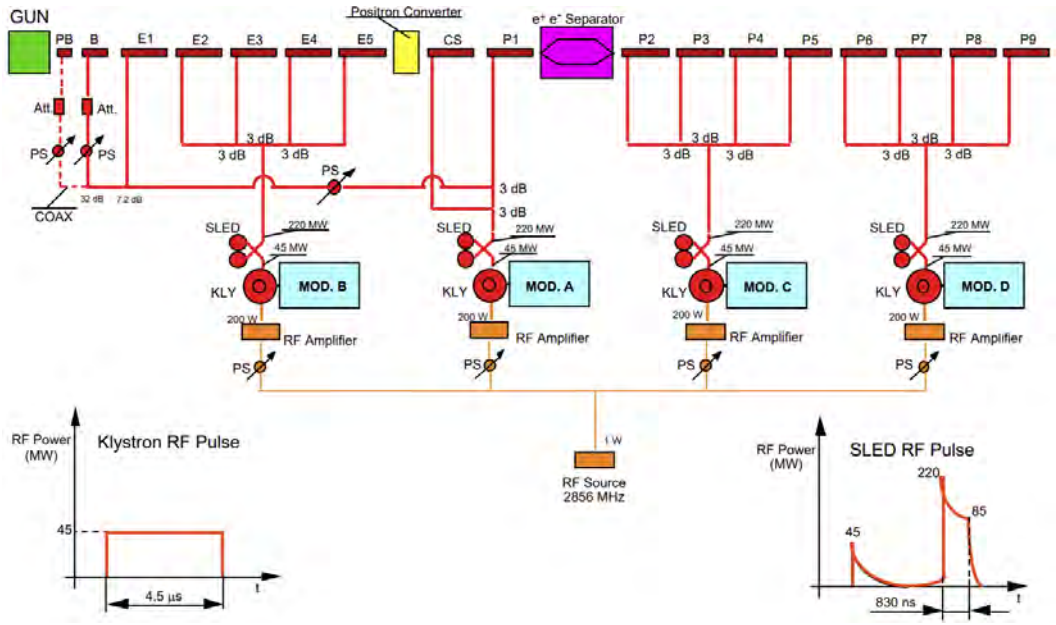

Figure 2.6. DAΦNE LINAC Radio-Frequency Power distribution.

is the electron mass), an electron-positron pair can be produced. The e^+ and e^- are produced with small momenta and must be re-accelerated by the P1 section. After being separated with a Dipole Chicane (violet in Fig. 2.6), 2 accelerating sections are used and the particles can reach an energy up to 550 MeV with a beam current of 36 mA (peak).

At the Frascati LINAC, the main limitation to the luminosity is the duty-cycle, i.e. the combination of two factors: the limited repetition rate of the LINAC (50 Hz, actually 49 usable pulses/s) and the limited macro-bunch length. The ideal beam would be a continuous, low intensity positron beam, making possible to reconstruct each individual interaction in the PADME target; this would allow an almost-zero-background experiment. However, a significantly long beam pulse structure, i.e. comparable to the inter-bunch of 20 ms, would be very interestingly close to the ideal beam. The SHERPA project is intended to close this gap between actual and almost-ideal working conditions.

2.2 Damping Ring

When the DAΦNE LINAC operates in positron mode, the bunch population is much less than the bunch population while operating in electron mode by a factor ∼1000. This is due to the fact that the electrons emitted by the thermoionic gun are accelerated until the end of the LINAC, while the positrons are accelerated towards a Positron Converter Section. In this region, some of the electrons undergo Bremsstrahlung on a high-Z target and from the originated photon it is possible to have pair-production of an electron/positron pair. In order to populate the positron bunches, it is necessary to store them along a circular path and synchronously re-inject positrons from the LINAC. In this early phase, the RF cavity of the Damping

Ring compensates the Synchrotron Energy Losses due to Bremsstrahlung-photons emitted by the positron while constraint along a curved path. When the bunch is sufficiently populated, the RF cavity is tuned in such a way to give more energy to the particles and not simply compensate Synchrotron Losses.

The Damping Ring configuration is shown in Figure 2.7. It has an octagonal shape; eight dipoles are used to bend the beam by 45° each. Horizontal and vertical focusing and defocusing are performed using twelve quadrupoles. Eight sextuploes are interposed between the quads for chromaticity correction. Four scrapers adsorb the off-trajectory particles. Two septa are used for injection/extraction and the RF cavity gives the energy to the circulating lepton beam. Four kickers (two in the RF cavity neighbourhood and two in the opposite side, 90° off the septa) are used to put the particles off-trajectory in order to have sufficient lateral displacement needed to enter the septum extraction region (or vice versa for the injection: off-trajectory particles must be "kicked" into the rigth orbit and overlap synchronously with the right bunch of the circulating beam).

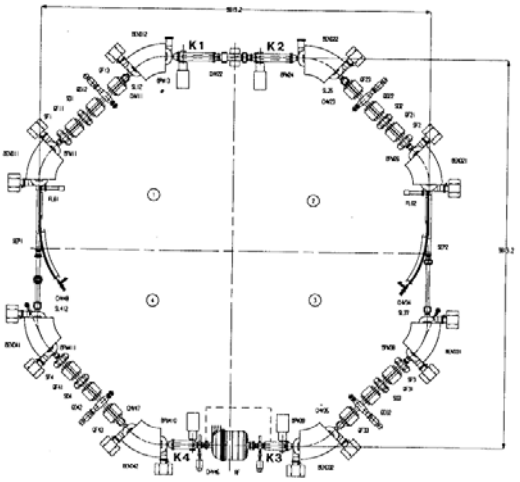

Figure 2.7. Damping Ring configuration.

Each quarter of the ring is composed by a FODO (Focusing-Drift-Defocusing-Drift) lattice arranged as follows:

- 45° bending Dipole
- Sextupole
- Quadruplole, Horizontal focusing and Vertical defocusing
- Sextupole
- Quadruplole, Horizontal defocusing and Vertical focusing
- Scraper or Beam monitor used for diagnostic purposes
- Quadruplole, H+V defocusing and H-V focusing or viceversa

- 45° bending Dipole

Two septa, one for injection and one for extraction, direct the particles from and towards the injection/extraction common line, indicated in yellow in Figure 2.5. The septa configuration is visible in Figure 2.8.

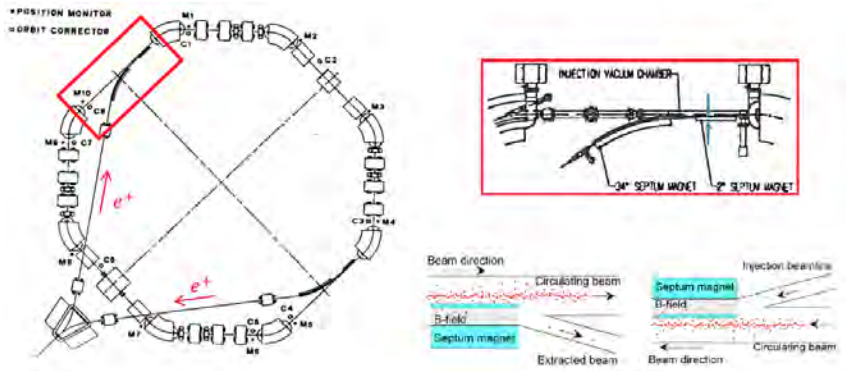

Figure 2.8. Damping Ring Septum configuration and position.

After being stored and populated to the desired number of particles, the electrons/positron bunches can be transported to the DAΦNE double ring collider. It is important to remark that the Damping Ring length is exactly one third of the DAΦNE Main Rings length and the Radio-Frequency of the Damping Ring is 1/5 of the DAΦNE RF.

2.3 DAΦNE Rings

The DAΦNE electron-positron collider (Double Annular Φ-Factory for Nice Experiments) has been designed for reaching a target luminosity of $5 \cdot 10^{32}\ cm^{-2}s^{-1}$ at the relatively low center of mass energy of 1 GeV. In order to achieve such high luminosity, the choice has been to have separated electron and positrons storage rings and 120 bunches, very closely spaced along the ∼97 m long machine, reaching currents in excess of ∼2 A and with very squeezed beams at the interaction point [19].

The available charge in a single LINAC pulse is of ∼1 nC, and in order to improve the emittance of order 10^{-5} m·rad prior to injecting in the main ring, positrons are stacked and damped in a smaller ring. In this configuration, the pulse width is ∼10 ns at the injection into the accumulator, from where positrons are extracted and injected at 2 Hz in the main ring. Up to 120 bunches circulate in the DAΦNE rings, running at an RF of 368.26 MHz, i.e. with a separation of 2.7 ns and a RMS length increasing with the current from <1 cm up to ∼3 cm. The same procedure is applied for filling the electron ring [19].
Since 2008 the Crabbed-Waist collisions scheme was implemented, allowing to reach a luminosity of $> 4 \cdot 10^{32}\ cm^{-2}s^{-1}$, based on increasing the horizontal crossing angle (reducing the horizontal beam size at the interaction point), and suppressing synchro-betatron oscillations by means of sextupoles.
The full magnetic layout of the rings with only one interaction region is shown

in Fig. 2.9: electron (blue) and positron (red) rings cross in the middle of two ∼10 m long straight sections, where the two interaction points are placed: IP1, used for KLOE and SIDDHARTHA experiments, and IP2 used for the FINUDA experiment [19]. The KLOE Experiment was devoted to the study of the Φ meson decay into Kaons (in particular K_L and K_S) at a center of mass energy of 1.02 GeV. The Branching Ratio of this process is ∼85% [20]. FINUDA has been replaced with a vertical separation of the two beams and a quadrupole triplet, for implementing the crabbed waist scheme. There are a short and a long arc for each ring, each with four 45° bending dipoles. Arc halves – each containing two dipoles and one wiggler – are connected by short straight sections where the Radio-Frequency cavities (short arc) and the injection septa (long arc) are placed [19].

In order to perform DAΦNE operations, electrons and positrons are transported by the line indicated in green in Fig. 2.5. The Transfer Line setup (Fig. 2.9) consists in two parts: the first is common for electron and positrons; then a dipole switches positrons in the clockwise ring and electrons in the counterclockwise ring.

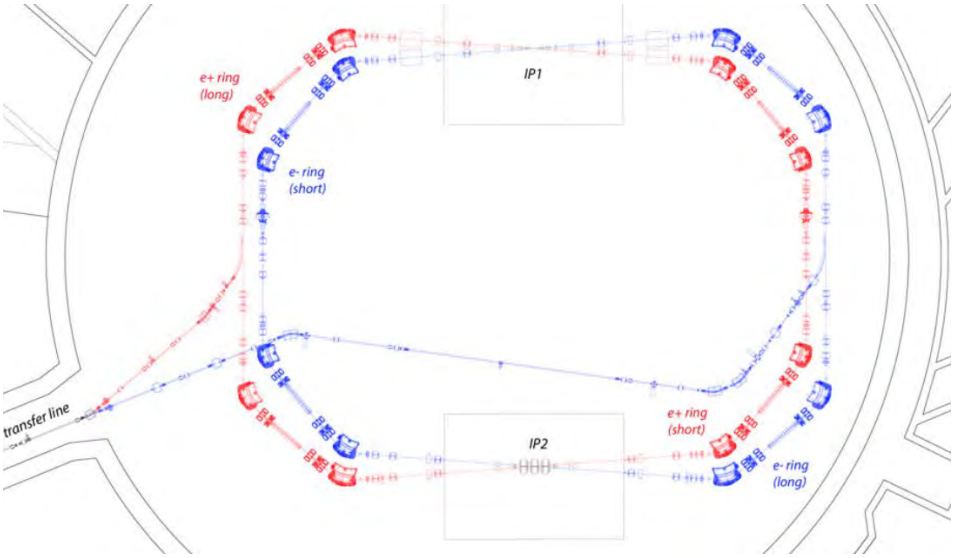

Figure 2.9. DAΦNE configuration. After re-circulation in the Damping Ring, the extracted electrons or positrons are transported to DAΦNE via the Transfer Line. A pulsed dipole switches electrons or positrons along different paths. In blue: electron ring, counterclockwise circulation. In red: positron ring, clockwise circulation.

A schematic view of the DAΦNE collider is reported in Figure 2.10. In this CAD 3D representation, the electron ring has green dipoles and positron ring has orange dipoles. For the sake of clarity, the transfer lines have not been reported. Figure 2.11 shows one of the two RF cavities during the assembly phase and after the installation of the Higher-Order Mode Adsorbers.

Figure 2.10. DAΦNE 3D view. Green dipoles are fot the electron ring, orange dipoles for positron ring. In this artwork is visible also the KLOE detector, used for Φ decay experiments. Courtesy of Paolo Valente and Mauro Raggi.

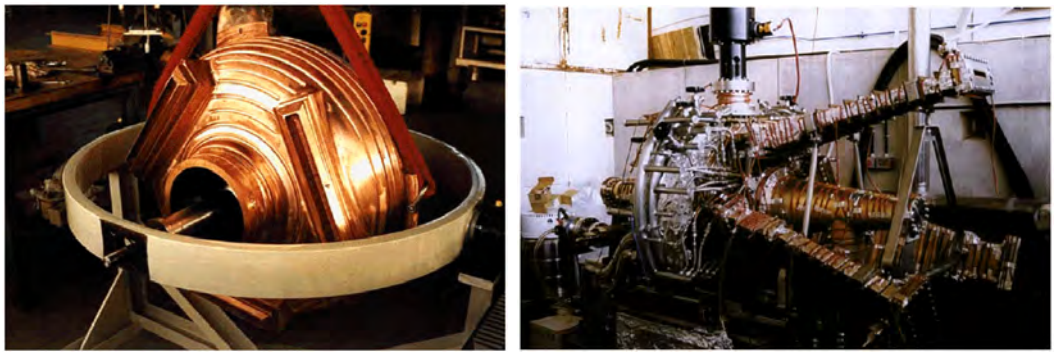

Figure 2.11. Left: DAΦNE RF cavity prototype assembly. Rigth: DAΦNE RF cavity assembled, with Higher-Mode Adsorbers. Images taken by LNF website http://www.lnf.infn.it/acceleratori/dafne/main.html.

2.4 BTF and BTF-II

In this section the Beam Test Facility setup is described. The original BTF setup has recently been modified in order to have a second beamline (BTF-II) for general test purposes, due to the fact that the first BTF line is currently serving the PADME experiment from 2015. The old BTF line and the new BTF+BTF-II configurations are represented in Figure 2.12 (a) and (b) respectively [8].

The DAΦNE BTF is a beam transfer line from the DAΦNE LINAC, capable of providing up to 50 bunches per second of electrons or positrons with 800/550 MeV maximum energy with a variable bunch width from 1.5 to 350 ns. Usually the 50 Hz are not delivered because 1-2 Hz are dedicated to the beam diagnostics and energy characterization with the spectrometer magnet (see Figure 2.5). Each bunch consists of micro-bunches with total length of 350 ps with 140 ps flat-top and the typical emittance of the electron/positron beam is of 1(1.5)mm·mrad [19]. The RMS

beam spot size is variable between few hundreds μm to 1 mm in x and y directions, while the typical beam divergence is in the range 1-2 mrad for BTF primary line. The beam divergence could be reduced down to $\sim$ 0.5 mrad in particular conditions.

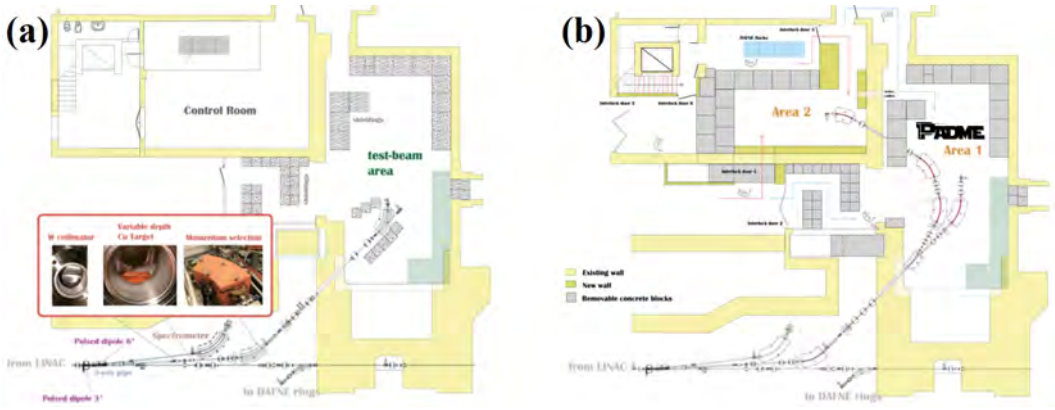

Figure 2.12. (a) Layout of the old BTF line and area. The pictures inserted represent the Tungsten collimators pair, Copper beam-attenuating target and energy-selecting dipole magnet DHSTB001 [8]. (b) The new BTF-II line has been added in 2021 and thus the building for hosting two separated experimental areas modified layout is shown [8].

The BTF can operate from single particle regime up to 10^9 particle per bunch. This is due to the fact that a 75:25% Tungsten-Rhenium target with variable thickness between 1.7 to 2.3 X_0 used to reduce the beam intensity is put downstream the 3° pulsed dipole. The target spreads the momentum distribution of the incoming beam, then secondary electrons/positrons are selected by their momentum with a 45° dipole and collimators in the horizontal plane. The beam intensity is thus greatly reduced, depending on the chosen secondary beam energy central value (from about 50 MeV up to almost the primary beam energy) and spread (typically better than 1%, depending on the collimators settings) [8]. The BTF beam main parameters achieved in different operation modes are reported in Tab. 2.2

Parameter	Parasitic Mode		Dedicated Mode	
	With Target	Without Target	With Target	Without Target
e^+, e^-	selectable at BTF	depending on DAFNE injection	selectable at BTF	selectable at LINAC
E (MeV)	30-500	510	30-700	250-750,e^- 250-550,e^+
En.spread $\sigma(E)/E$	1% at 500 MeV	0.5% fixed	1% at 500 MeV	0.5 - 1% fixed

Table 2.2. : BTF Beam Main Parameters achieved in different operation modes [8].

The sensitivity estimate for the PADME experiment assume that the DAΦNE LINAC will be able to provide 50 bunches/s of 350 ns duration with $10^4 - 10^5$

positrons in each. The present maximum positron energy of 550 MeV is assumed. In these conditions a sample of $2 \cdot 10^{13}$ positrons on target can be obtained in one year ($\sim 10^7 s$) of data taking [15].

2.5 The PADME experiment luminosity limits

High-energy, high-intensity positrons beams are of utmost importance for fundamental physics. In particular, e^+ fixed target annihilations experiments for dark sector particle searches can profit of a quasi-continuous, high-energy positron beam. The first experiment searching for light dark matter particles with the missing mass technique in positron fixed-target annihilations is PADME at the INFN National Laboratory of Frascati. The experiment uses the Beam Test Facility extracted beam line. In each second 49 bunches of 10^4–10^5 positron per pulse, of 150-200 ns length and 550 MeV energy, are send on a very thin, active diamond target. The Run I and Run II data taking periods of 4-6 months, allowed the experiment to collect $\sim 10^{13}$ positrons on target. The projected sensitivity is $\epsilon \approx 10^{-3}$, i.e. already in the interesting band favoured by the muon g-2 anomaly, as shown in Fig. 2.13. The potential physics reach of PADME for a integrated statistics of $4 \cdot 10^{13}$ positrons on target is also shown [15].

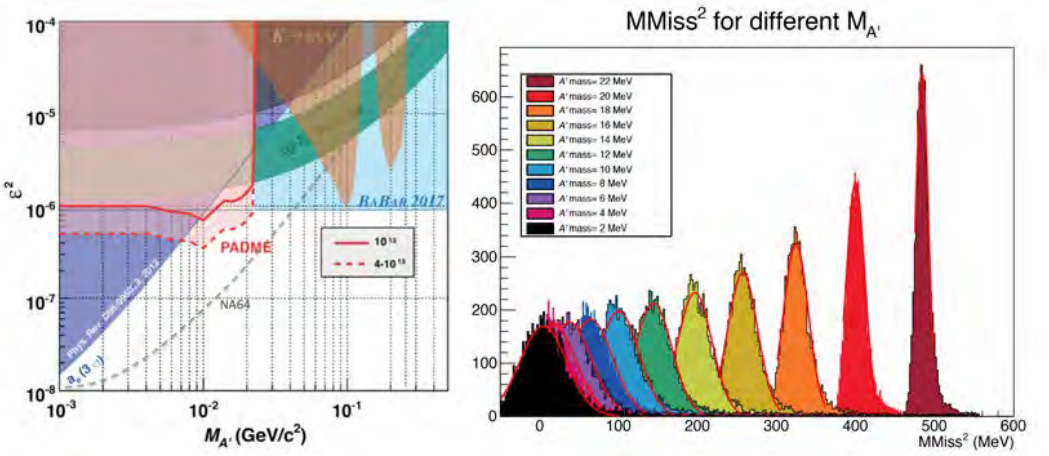

Figure 2.13. Left: Expected sensitivity of the PADME experiment for 10^{13} (full line) and $4 \cdot 10^{13}$ (dashed line) positrons on target; the exclusions in invisible decays are also shown (see text). Rigth: Missing mass for different dark photon A' squared masses [19].

The PADME experiment will exploit the possibility of positively looking for a peak in the missing mass spectrum (Fig. 2.13, right) in events $e^+e^- \to \gamma +$ invisible particles , in a clean and model-independent way, up to ∼24 MeV mass, thanks to a finely segmented, high-resolution inorganic crystals calorimeter, and a number of veto detectors (see Fig. 2.14).

This model-independent technique is sensitive not only to dark vector (dark photon), but also to more exotic dark sector candidates, like the proto-phobic boson claimed to be responsible for the anomaly in the internal pair angular distribution in ^{8}Be radiative transitions, or to the axion-like particles.

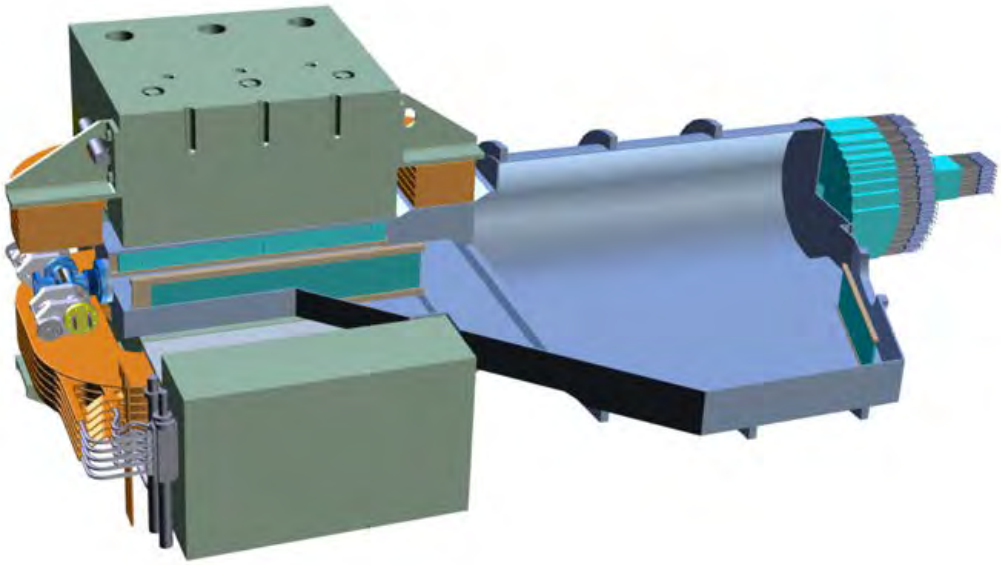

Figure 2.14. PADME setup view, showing the target area, the dipole magnet with embedded scintillators as positron veto, the vacuum vessel with the additional scintillator detector and the main cylindrical BGO crystal calorimeter, followed by the fast small angle photon detector [19].

The main limitation to the PADME sensitivity comes from the time structure of the positron source. Due to the pile-up and beam background in the detectors, the maximum intensity (and hence the luminosity) is limited to $\sim$100 e^+/ns.

The divergence and energy spread of the beam are also crucial, since the precise knowledge of the positron 4-momentum impacts the missing mass resolution. Another limiting factor in the fixed-target approach is of course the maximum beam energy E_{e^+}, giving access to a range in the center of mass ($M_2 < 2m_e E_{e^+}$).

The duty-cycle is in general low in the case of warm LINAC's, on the contrary, continuous-wave beams are produced using superconducting cavities, but with much higher cost and complexity. The production of intense positron beams, both polarized and unpolarized, is very interesting for fundamental physics (like the dark sector experiments), so that currently is being studied at large accelerator facilities using cold technology, like MESA in Mainz, LCLS-II at SLAC and CEBAF at JLAB, and is under consideration also for the proposed electron-ion collider.

In the case of DAΦNE the duty factor is limited to $\sim 10^{-5}$, since the 50 Hz LINAC is only capable of accelerating pulses up to few hundreds of ns. The compression of the RF power by means of the SLAC Energy Doubler device (SLED), enables to reach a maximum energy of 750 MeV/550 MeV for electrons/positrons with the relatively low power. This limits the possibility of increasing the beam macro-pulse length, in order to get a higher luminosity, while keeping the pile-up probability in the recoiling photon detector to a manageable level.

A possibility at the BTF would be to use the LINAC without the SLED compression: thanks to the new electron gun pulsing system, beam pulses can be produced and accelerated up to the maximum klystron pulse length of 4.5 μs, however in this case the maximum energy is lowered to approximately one half, i.e. up to 250–280 MeV for positrons.

Increasing the duty-cycle of the extracted positrons lines at Laboratori Nazionali di Frascati, by extracting positron from the DAΦNE ring, will allow the PADME experiment to reach luminosity gains of the order of 1000 to 10000.

Chapter 3

Beam extraction

The main goal of this chapter is to introduce the different extraction methodologies, comparing them and highlighting their main applications. The fast and slow extraction techniques are analyzed at the beginning of this chapter; then, focusing on slow extraction, resonant and non-resonant methods are explained. A new and barely explored type of slow non-resonant extraction is the crystal-assisted one. This methods is based on the fact that a particle entering a crystal (within an acceptance angle limited by the Lindhard angle) can be deflected by the strong electrostatic field generated by the atoms of the crystal lattice itself. The DAΦNE positron extraction is further described, introducing also the POSEYDON project. At the end of the chapter the SHERPA project is described, including its application to the Pile-Up mitigation for the PADME experiment.

3.1 Fast and Slow extraction

While circulating in a synchrotron, for example the Large Hadron Collider at CERN, the particle beams interact in several Interaction Points (IP). In those collisions, new physics event could be produced and the property of the quantum final states obtainable in such collisions can be recorded with our electronic eyes: the detectors. Protracting the collisions in time means that the beam, after many interactions, will be progressively depopulated and spoiled, degrading it turn by turn. Moreover, the beam losses are mainly due to imperfections in the collider, in particular the collimators and the adsorbers installed along the collider rings. When the beam properties are not within the operative design parameters, the beam has to be replaced totally before a new re-injection into the rings. This process must be as fast as possible, thus the fast extraction technique is used. Furthermore, this extraction can be safely performed while the beam is not in the designed orbit. If the beam is not reported in its design trajectory, it could damage the machine because of the stored energy within each bunch-train. If the beam impacts on the collider components, the consequences can be disastrous.

In the most ideal and simple picture, the fast extraction is performed by two elements: a kicker and a septum Magnet. The kicker is needed in order to "kick" the circulating beam off its design orbit using an intense electrostatic or magnetic fields

and thus deflecting the particles. Depending on the particles energy, the kicker will induce a lateral displacement that is bigger in the case of low-energy particles with respect to high energy ones.
The septum magnet is built in such a way to collect the particle previously deflected by the kicker. In the inner septum region there is a magnetic field that enhances the particle bending, deflecting them towards a specific line used for the extraction. In the septum external region, magnetic field is not present in order not to deflect erroneously the particle beam travelling in its design orbit.
The fast extraction technique is shown in Figure 3.1, see Ref. [4].

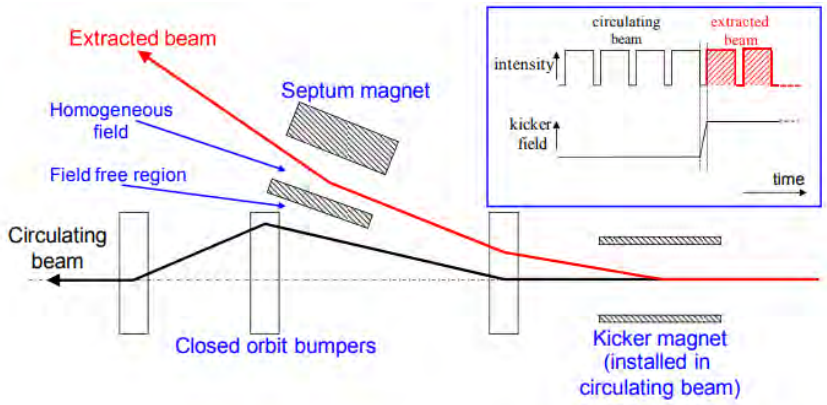

Figure 3.1. Fast beam extraction [4].

Fast extraction is mainly used when there is the necessity of a beam dump, meanwhile slow extraction is intended mainly for injection in a bigger collider, i.e. the beam circulating in the LNF Damping Ring is slowly-extracted toward the DAΦNE Main Rings. Furthermore, the slow methodology is particularly useful when delivering particles on a fixed-target experiment that requires low Pile-Up, i.e. the PADME experiment described in Sec. 2.5.
The slow extraction can be performed in several ways: the most used method is the resonant extraction. In this configuration, some magnetic element create an instability in the phase space of the particle beam. Another technique adopted in order to slowly extract the beam is the non-resonant methodology.

3.1.1 Resonant and Non-Resonant Slow extraction

The resonant multi-turn extraction is widely used in order to extract slowly particles from a synchrotron. This technique is based on the creation of controlled instability regions in the particles phase space, so the particles can be displaced off their nominal trajectory and thus can be furthermore deflected by electrostatic or magnetic fields generated by kickers and septum magnets. Usually the tune (number of oscillation in the phase space for one revolution in the machine) is set to a value closest to 1/2, 1/3 or 1/4 of integer. The 1/3 of integer resonance can be obtained acting on the local magnetic field generated by the sextupole magnets; meanwhile a less usual choice, which produces shorter extraction times, is the 1/2 of integer resonance. Usually there is not convenient to go beyond 1/4 of integer resonance, due to separatrices

proximity.
In a linear machine, where linear is due the fact that only linear elements are used (dipoles to bend the beam and quadrupoles to focus/defocus), the phase space (x,x') is described by an ellipse that doesn't change its area. Despite the emittance remains the same, the particle phase space can change its shape and it can also rotate, according to the machine tune. The ellipse axis can even be renormalized in order to represent the phase space as a circle [19]. Sextupoles are used for higher-order chromaticity corrections and thus introduce non-linear effect. The (x,x') phase space corresponding to the 1/2 of integer extraction setting is similar to the linear case only along the beam design trajectory. The more far from the beam orbit, the more deformation of the particles phase space is induced. In the Figure 3.2, the region of stable motion is delimited by the separatrices (green lines). The 1/3 of integer phase space assumes a triangular shape, and three separatrices can be identified. The stability region of the phase space is the one enclosed within the separatrices. Particles out of the stability region boundary will be further moved outward the beam core turn by turn, following the separatrices trajectories, denoted with arrows in Fig. 3.2. The stable triangle does not change area when moving along the machine at a position s from the sextupole, it will just get rotated (clockwise) by the betatron phase advance [19].

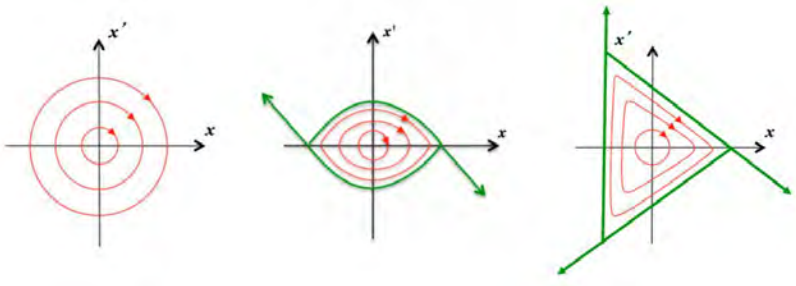

Figure 3.2. Phase space distributions (x,x') for a linear machine (left) and in case of tune close to 1/2 (middle) and 1/3 of integer resonance (right, $\delta Q>0$) at the sextupole. If the tune is below the resonance the rotation in phase space is reversed, if the strength of the sextupole is reversed the triangle is mirrored with respect to the x' axis. Reproduced from Ref. [19].

In Figure 3.3, the Resonant Extraction is visualized. The Synchrotron tune makes the phase space rotate without changing its area, according to Liouville's Theorem. Assume the particle is just out the stability region at turn n. After 1 turn, the particle travelling along the separatrix will be shifted outward, following a spiralizing trajectory in the (x,x') plane meanwhile the curvilinear abscissa (s), describing the particle position in the Synchrotron, increases. At (n+2)-th turn, the particle has been furthermore shifted outward following the separatrix. Finally, at (n+3)-rd turn, the particle has been sufficiently deflected to be able to enter the Septum region, thus receiving a kick by the Septum itself.

Exactly at resonance no stable trajectory in the horizontal phase space (x,x') exists. As the betatron tune approaches towards the resonance, the phase space stability region shrinks and particles with smaller amplitudes become unstable, as

illustrated in Figure 3.4, where for example the resonant slow extraction at the Cornell University Synchrotron is proposed [11].

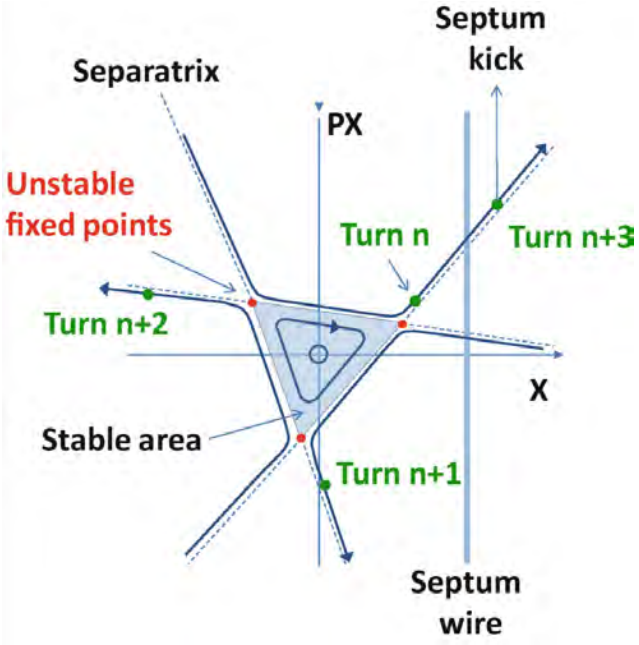

Figure 3.3. Resonant Extraction dynamics.

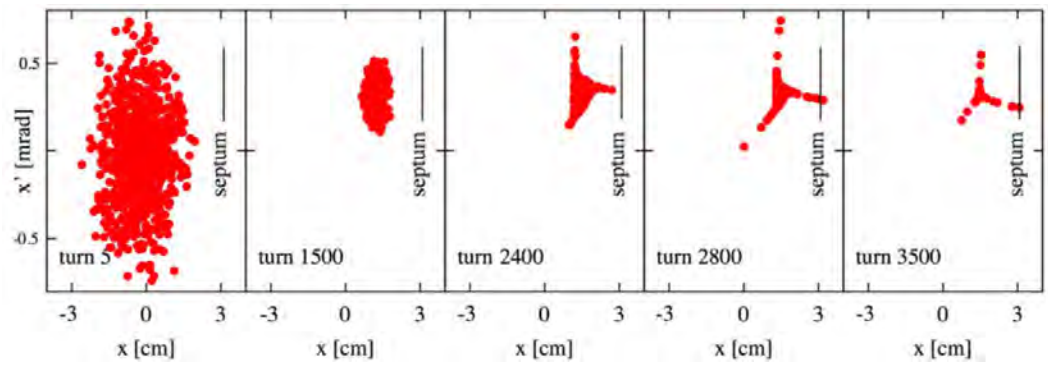

Figure 3.4. Beam phase space at five points during the acceleration and extraction cycle, illustrating the third order resonance extraction from the Cornell synchrotron. Reproduced from [11].

Other Slow Extraction techniques exist, in particular some variants of the standard Resonant Extraction, partially described and cited in Ref. [19]. Non-Resonant Extraction can be performed both in Fast and Slow variants.
The Fast Non-Resonant Extraction, described in Section 3.1, is performed deflecting the whole bunch using a Kicker and a Septum Magnet, arranged in the configuration reported in Figure 3.1. On the other hand, while performing Slow Non-Resonant Extraction, a bent crystal can be used. Some of the impinging particles entering the crystal within the critical angle can be channeled by the high inter-planar electrostatic field.

3.2 Crystal-assisted extraction

The crystal-assisted extraction is a slow non-resonant technique currently under investigation and studies are ongoing because it is foreseen to use this methodology for the High-Luminosity LHC beam collimation. SPS beam extraction with crystals has proven to be feasible, with promising results described in [17].
While using this methodology for collimation, the crystal is put widely off-beam-trajectory, in order to deflect a fraction of the particle populating the beam halo. In the case of solid-state collimators, the beam halo particles perform Multiple Scattering in the material and thus could be deflected in such a way to re-enter the beam core trajectory. Moreover, the high-energy particle impinging on the collimator could even undergo electromagnetic or hadronic shower. The crystal-assisted collimation strongly reduces this issue because the particles impinging the crystal can undergo Channeling and thus can be deflected to a solid-state adsorber. Crystal collimation strongly reduces also the machine impedance with respect to a standard kicker-septum configuration. Moreover, this technique is a cheaper and less complex alternative to the standard used extraction layout.
The solid-state and the crystal-assisted collimation methodologies are shown in 3.5.

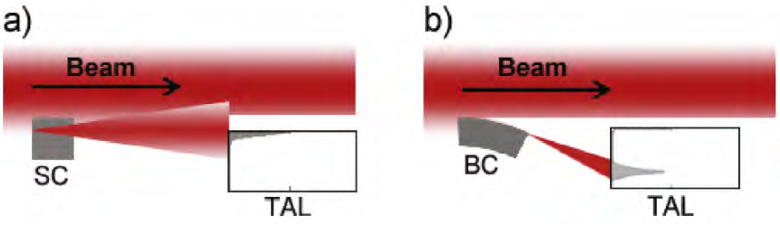

Figure 3.5. (a) Collimation scheme using a solid state primary collimator–scatterer (SC). (b) Collimation scheme with a bent crystal (BC) as a primary collimator. Halo particles are deflected and directed onto the absorber (TAL — Target Aperture Limitation) far from its edge. Reproduced from Ref. [17].

While the crystal-assisted technique is used for extraction, the same setup described previously is used. The Channeled particles, deflected by the crystal bending, will be further put off-trajectory by a kicker magnet. After that, the deflected particles enter the septum region, being deflected towards the Extraction Line. This extraction technique, in the non-local configuration is represented in Figure 3.6. Local and non-local crystal-assisted extraction share the same methodology, but it is important to remark that:

- In the local extraction scheme, the kicker and the septum are placed just downstream the bent crystal, so a relatively high deflection angle is needed.

- In the non-local extraction scheme, the kicker is placed just downstream the bent crystal, meanwhile the septum quitely distant. In this case a relatively low deflection angle is sufficient. The SHERPA project (described in Subsec. 3.3.2) uses this extraction scheme, represented in Fig. 3.7.

3.3 DAΦNE positron extraction

The aim of this section is to describe the possibility to extend the life of the DAΦNE collider Main Rings after the end of the Kaon Physics Program. An important opportunity could be to use the Main Rings to accomodate new facilities aiming to reduce the Pile-Up at the PADME experiment. In this direction, the POSEYDON and the SHERPA project have been developed by P.Valente and M.Garattini respectively.
The POSEYDON project aims to convert DAΦNE Main Rings into a High Duty-Cycle Pulse Stretcher and a Positron Storage Ring. A complete description can be found in the Proposal [19], by P. Valente.
The SHERPA project ("Slow High-efficiency Extraction from Ring Positron Accelerator") [10] aims to extract a positron beam form DAΦNE using a bent Si crystal, without touching the general layout and configuration of the Main Rings. It requires less modifications with respect to the POSEYDON project, thus it could be simpler to implement the crystal solution in (one of) the DAΦNE Main Rings.

3.3.1 The POSEYDON project

The POSEYDON project could give a unique possibility to obtain an intense, high-duty-cycle, narrow-band and low-emittance ultra-relativistic positron source, for a wide range of scientific and technological applications, realized improving the available accelerator complex of DAΦNE at Frascati National Laboratories (LNF) [19]. One of the two Main Rings can be used as a positron beam Pulse-Stretcher. As said in Section 2.1, the main limitation to the luminosity is the duty-cycle, i.e. the combination of the limited repetition rate of the LINAC (50 Hz) and the limited macro-bunch length. After being stretched, the particle bunch can be extracted to a dedicated transfer line, optimizing the use of the existing infrastructure. The other Main Ring will be mantained as is now, providing Synchrotron Radiation to the DAΦNE-Ligth Laboratories, both in the UV and X-ray spectral regions.

In order to define the project details, the main parameters for the stretched beam should be defined [19]:

- Energy: the maximum achievable energy is fixed by the Radio Frequency power and the Main Ring length (∼100 m). The dipoles can be pushed up to 750–800 MeV before reaching iron saturation and the maximum positron energy outgoing from the LINAC is presently limited to ∼550 MeV [19].

- Energy spread: improving the 1% level achieved using the BTF line for the PADME experiment would allow a more precise reconstruction of Dark Photon candidates events, where the precise definition of the kinematics is very important. Nevertheless, the improvement in energy resolution would be also beneficial to all other potential applications of the high-energy positron source [19].

- Emittance: it defines a good quality of the beam in terms of angular and spatial spread. At the endpoint of the BTF "old" line, the emittance is equal

to 10^{-6} $m \times rad$ at 500 MeV. In order not to spoil the beam quality, the emittance must be preserved [19].

- Duty-Cycle: the most important parameter in order to have a high average intensity source. The D.C. is defined as the fraction of time of the beam spill over the total time of a period. High peak intensity can be obtained using intense and short beam pulses, but this kind of time structure is not desirable when the Pile-Up of very close in time events is a limiting factor, like in fixed-target annihilation experiments (as PADME). The DAΦNE LINAC Duty-Cycle is of the order of 10^{-5} (200 ns spill over 20 ms period). It can be increased to 2×10^{-4} if accelerating positrons to an energy <300 MeV [19].

3.3.2 The SHERPA project

In order to perform the ultra-slow particle extraction, it is necessary to deflect off-trajectory, turn-by-turn, a small fraction of a particle bunch stored in a synchrotron. Within the framework of the SHERPA project, described in Ref. [10], we have studied the possibility to perform non local ultra-slow positron extraction assisted by a bent Si crystal, from one of the three rings composing the DAΦNE complex: the Damping Ring (DR) or one of the two Main Rings (Electron or Positron Main Ring).
The positrons impinging on the bent crystal within small angles relative to the lattice planes move oscillating between two neighboring planes can undergo planar Channeling, and consequently can be deflected by the crystal bending angle.
Crystal-assisted extraction via coherent processes in bent crystals have been under investigation and experimentally verified for high-energy hadrons in CERN Super Proton Synchrotron and U-70 IHEP Protvino Russian Synchrotron (Ref. can be found in [10]).
Reproducing this extraction scheme in DAΦNE is possible using crystals with micrometric thickness, in order to reduce the Multiple Scattering, due to the low energy of the positrons circulating in the DAΦNE accelerator.
Nowadays there exist a published previous experimental results of particle Channeling through a bent crystal with 855 MeV electrons, performed at Mainz Mikrotron by Bagli et al. [14]. The best performance of a silicon bent crystal of 30 μm thickness along the beam direction is about 1 mrad of deflection angle. In Ref. [14], the Channeling Efficiency was measured to be at the level of 20% for electrons. With positrons, the Channeling efficiency is expected to be even higher [7].
In the non-local extraction, a bent crystal is used to deflect the particles by a small angle (as reported earlier, 1 mrad deflection angle is suitable for the crystal used in DAΦNE accelerator complex). After this deflection, the kicker puts the particle further off-trajectory and turn by turn this displacement will increase until the particle reaches the septum and is deflected towards a dedicated extraction line (see Figure 3.6).

In the following Figure 3.7, it is shown the location of the bent crystal and extraction septa in the two cases of the Damping Ring and the DAΦNE positron Main Ring.
In the Damping Ring setup, positrons with an energy of -1.0 %, with respect to the

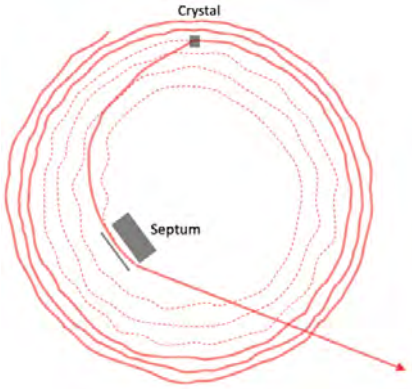

Figure 3.6. Non–local extraction of a particle using the deflection produced by channeling in a bent crystal. The particle oscillates in the storage ring until it interacts with the crystal, changing its trajectory towards an extraction section represented by a septum.

nominal one will arrive at the crystal location with an horizontal displacement of -7.5 mm. The positrons in the accumulator ring loose 1.0 % of energy by synchrotron radiation in 1000 turns, thus the extraction time is estimated to be 100 μs after injection at nominal energy, given that the Radio Frequency cavity is kept off. Those particles could interact with the crystal and thus be kicked by about 1 mrad, producing a larger horizontal displacement of about -11 mm at the septum position [10].
The best configuration for DAΦNE Main Ring extraction is the one with the crystal positioned just before the rings crossing point (IP2), shown in Fig. 3.7 and the extraction septum placed just downstream the IP2. The extraction would be thus performed only a few meters downstream the crystal, in the same straight section of the positron Main Ring. In this configuration, a positron with an energy offset of the order of -0.7% will encounter the crystal, positioned at 8 mm from the circulating beam axis, at the 6^{th} turn in the machine, and will be extracted in the same turn [10].

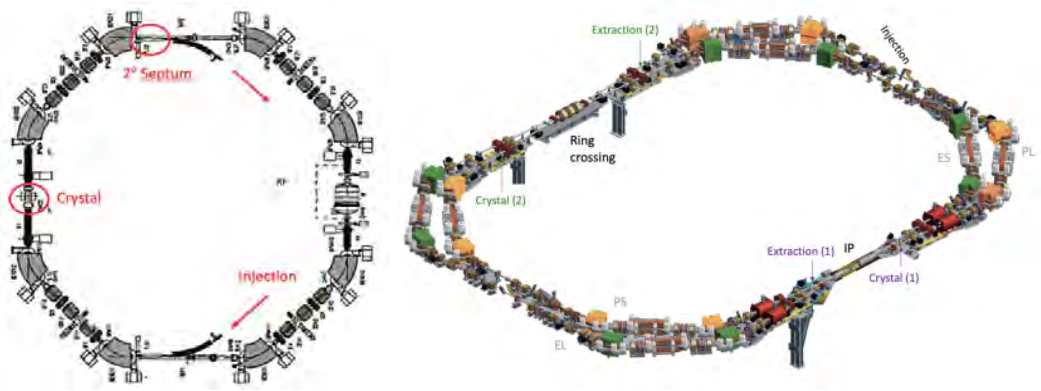

Figure 3.7. (Left): Damping Ring non-local extraction. (Right): DAΦNE extraction.

3.3.3 SHERPA test setup requirements and constraints

The SHERPA experimental setup is almost ready to be assembled in the BTF-II hall, fed by the new BTF-II line built in 2021 and described in the Section 2.4. The beam provided by the BTF has a typical beam spot of 0.5-1.5 mm radius and a divergence ranging from 500 μrad to 2000 μrad, thus the BTF can provide a particle beam with a typical emittance of 250-3000 $mm \times \mu rad$. The Geant4 simulations, described in the next Chapter, are used in order to give a constraint on BTF spot size and divergence needed by the SHERPA experiment to be successful. In order to make a narrow RMS beam-spot size at fixed emittance, the divergence will increase. What it is limited by emittance is the sum of the squares of X and Y RMS beam spot sizes. A possible solution to get better visibility for the channeling effect, is to reduce the X divergence while increasing the Y divergence. In fact the bending is only in the horizonthal plane where we are interested in having as small as possible beam dimensions.

In order to measure the Channeling efficiency, it is necessary to work with the crystal in the correct position because a misalignment can lead to erroneous outcomes and thus efficiency underestimate. The "angular scan" to asses the alignment in between the beam and the crystal planes, should be performed as Mazzolari et al. did in [14]. The crystal orientation angle should span from -1000 μrad to +1500 μrad, in order to find the maximum Channeling efficiency corresponding to aligned crystal position.
The experimental setup is strongly constrained by the space available in the BTF-II hall II and the SHERPA setup dimension: given the size in Figure 2.12(b), only ∼3 m distance between the bent crystal and the sensors will be possible.
The crystal used for he SHERPA project will be very similar to the one used at MAMI in 2014 by Mazzolari et al in Ref. [14]. The Si crystal should have a thickness of $\sim$ 30 μm, with a Bending Radius of $\sim$ 33.5 mm. The Channeling deflection angle should be of the order of $\sim$ 1000 μrad. The SHERPA experimental setup is described in Picture 3.8.

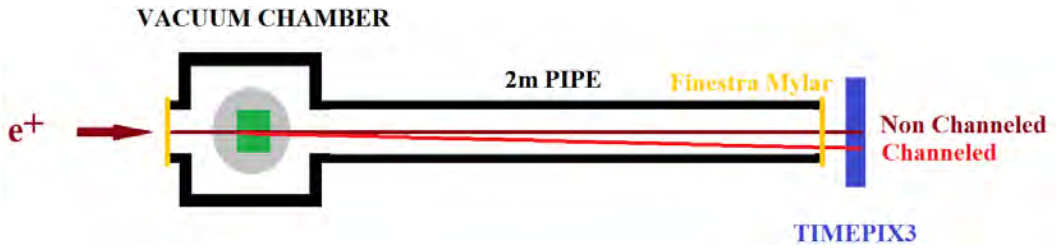

Figure 3.8. Geometry of the SHERPA experiment. In yellow: two vacuum-resistent Mylar windows. In grey, the goniometer that moves the holder on which is fixed the bent crytal, in green. In blue: the TimePix3 detector.

Chapter 4

Geant4 simulation of Coherent Processes in bent crystal

In order to understand the beam parameters necessary to observe the Channeling process with a ∼500 MeV positron beam, in this thesis work we started to benchmark and validate the existing implementation in a dedicated Geant4 routine of the Channeling process.

In this chapter the simulations of different experimental setups are described. The simulation are carried out using the Geant4 Channeling Routine, implemented by E. Bagli et al. [3], present only in the Geant4 Version 10.05.p01.

This routine was specifically optimized in order to reproduce the CERN UA9 H8 transfer line experimental setup, and will be modified in order to reproduce other experimental setups of our interest, such as the Mainz Mikrotron at Mainz University, Germany, and the SHERPA setup at the Beam Test Facility in Frascati National Laboratories. The simulations presented in this thesis are aimed to study the crystal Channeling, that is the key feature underlying this analysis.

To our knowledge this routine has never been used before in practical applications, and no publication exist on its performance while simulating leptons. All Monte Carlo results presented in [14], [2] articles are obtained via analytical simulations: the equation of motion of the particles travelling into the crystal and the physics underlying the coherent processes illustrated in Chapter 1, are solved analytically. The aim of this Chapter is to summarize the main results of the simulations we performed, and to compare them with the experimental data when available.

As a first check of the Geant4 Channeling Routine, we used, as reference data samples, the SPS (400 GeV protons) [17] and MAMI (855 MeV electrons) [14] configurations. The MAMI configuration has in addition been simulated with positrons instead of electrons, in order to check if low energy positrons simulation behave as well as high energy protons ones. The results will further be compared with Prof. V. Biryukov analytical simulations. The code used by Biryukov is described in [5, 6]. After this benchmark phase, we understood that the Routine is producing

reasonably good results, compatible with the phenomenology observed. Finally we started to study the SHERPA LNF BTF-II configuration, with both 511 MeV electrons and positrons.
The main goal is to define requirements for the beam spot size and divergence, in order to successfully observe the channeling effect at LNF. This work can be also useful in the future for integrating the simulation in the DAΦNE MAD-X code.

4.1 The Geant4 implementation of the crystal channeling properties

In the Geant4 10.05.p01 routine, developed by Bagli et Al. at INFN-Ferrara [3], the physics of Channeling and Volume Reflection has been added to the standard Geant4 physics list. The Rechanneling process has not been yet implemented. This effect is particularly relevant for electrons and will be of crucial importance when comparing Geant4 simulations with respect to the analytical MAMI ones [7,14]. The description of the Channeling model implemented in Geant4 can be found in the paper [3]. In this simulation the only available Channeling lattice plane is described by the Miller Indices (110). With this crystallographic configuration the Channeling efficiency are expected to be different with respect to the one obtained with the (111) plane, and this is a direct consequence of the fact that in the two configurations the inter-atomic potential wells are different [2,18]. Moreover, in the crystal with the (111) orientation the large distance $d_p^L = 2.35$ Å between atomic planes changes periodically into a small one d_p^S, where $d_p^L = 3d_p^S$ [7].

4.1.1 The Geant4 example code architecture

In the Geant4 demonstrator of the channeling routine a setup inspired to the UA9 experiment setup at H8 is implemented. The geometry, shown in Figure 4.1, consist of a Gun Particle Source (GPS) and 3 pixel detectors: 2 of them (T1-T2) are interposed between the Gun Particle Source and the bent crystal (further denoted also XTAL), the other detector (T3) is placed downstream the crystal. These detectors allow to measure incoming and outgoing angle of the impinging particles, before and after the interaction with the Si bent crystal. In order to minimize the Multiple Coulomb Scattering, the geometry is under vacuum and the thickness of the detectors is a small fraction of the Silicon radiation length X_0. In the thesis the HEP convention will be used: the particle beam is directed along the positive direction of the z axis, meanwhile the x and the y axis define the transverse plane.

In the data cards files of this example, there are some parameters that allow to adjust the size and angle of the crystal. The deflection of the crystal is in the x direction, towards right for positive curvature radius. The curvature is dictated by the Bending Radius (BR), which is related to the angular deflection that the particles will undergo as:

$$\theta_{Deflection} = \frac{XTAL_{z-dimension}}{BR}$$

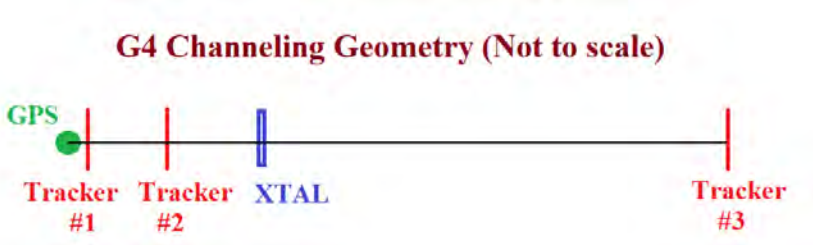

Figure 4.1. Geant4 geometry of the GPS, Trackers and Crystal. The reference frame is centered on the geometric center of the crystal.

In the standard Geant4 example the bending (Channeling) angle is:

$$\theta_{Deflection} = \frac{1.94\ mm}{38.416\ m} = 50.5\ \mu rad$$

The angle is adjusted via the command '/xtal/setAngle' which defines the rotation of the crystal around the axes (x, y, z). In the simulation the crystal is positioned so that the curvature appears as shown in Figure 4.2 (not to scale). It is rotated along the y-axis (vertical), by an angle equal to $0.5 \cdot \theta_{Deflection}$ (negative sign for the orientation of the y-axis). In this way the particles travelling along z-axis, will impinge the crystal on the convex face.
Using data cards is also possible to change the beam particle energy, the particle type (proton, electron or positron), the beam divergence along the x, y axis, (σ'_x and σ'_y) and the RMS of the beam spot size.

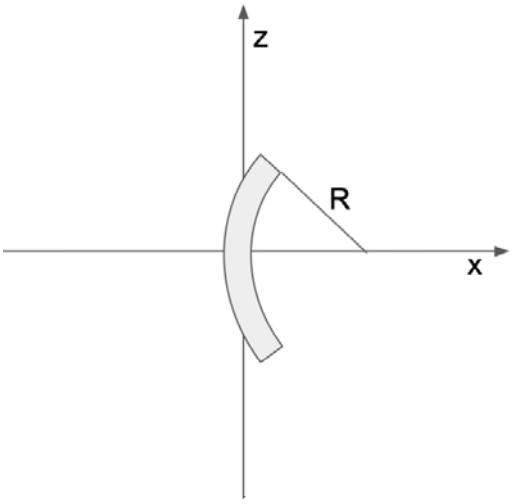

Figure 4.2. Crystal positioning in the reference frame. This position defines the Zero-Orientation Crystal angle.

The physical observable are stored in a 6-branches root Tree containing:

- **angXin** (**angYin**): the horizontal (vertical) angular distribution of the impinging beam.

- **posXin** (**posYin**): the horizontal (vertical) position distribution of the impinging beam.
- **angXout** (**angYout**): the horizontal (vertical) angular distribution of the beam after crossing the crystal.
- **angCry**: the crystal rotation angle with respect to the position indicated in Figure 4.2. Positive sign for counterclockwise rotation, negative sign for clockwise rotation.

The crystal rotation angle was not present in the original Geant4 Channeling example, and has been added in order to recreate the 2D-Plot similar to the one in Figure 2a of [14]. The channeling efficiency computation is based on the analysis of the data stored into the angXout branch and it is described in the next Section 4.2. As an important remark, is it necessary to underline that the angular distributions are measured directly by Geant4 impact coordinate on the detectors. No detector related digitization process is performed. As said earlier, the trackers (T1, T2 and T3 of Fig. 4.1) allow to measure incoming and outgoing angle of the impinging particles, before and after the interaction with the Si bent crystal. This is obtained for the incoming angle using the coordinate at T1 and T2 to interpolate the particle direction, while for the outgoing angle the crystal and T3 impact coordinates are used.

4.2 Efficiency calculation procedure

A particle can undergo planar Channeling if it enters in the crystal within a specific angle with respect to the normal of the crystal surface; the Channeling region is by convention defined within $-\frac{\theta_c}{2}$ and $+\frac{\theta_c}{2}$. Note that this is only one among all the possible conventions defined while studying Channeling; nevertheless, this convention and this approach is the most commonly used.
The critical angle θ_c, or Lindhard Angle, depends on the particle energy E and the Silicon inter-planar potential Well, which takes a value of U=22.5 eV [17]. It can be computed as follow:

$$\theta_c = \sqrt{\frac{2U}{E}}$$

Not all the particles respecting this condition will undergo Channeling because of the efficiency of the process. To measure the efficiency we developed the following technique which will be used for protons, electrons and positrons.

The MC angular distribution of the deflection angle, evaluated only at zero-orientation Crystal angle, is represented on an histogram; thus a global Signal plus Background fit is performed and the efficiency is computed analytically. In order to perform the global Signal plus Background interpolation some intermediate steps must be taken (because a single three-function eight-parameter fit performed directly on the histogram would not have easily converged). First of all, the contribution due to Non Channeling, Multiple Scattering and Divergence effects is fitted standalone and the three parameters obtained are used to give a constraint on a second fit, that includes also the Dechanneling contribution. After the second interpolation, five

parameters are fixed and used to give a constraint on the Global fit, which includes the Channeling component. The Global fit is made out of three functions: f_{nc} that describes the Non Channeling, f_{dc} that describes the Dechanneling and f_{ch} that describes the Channeling.

$$f_{nc}(x) = A_{nc} \cdot e^{-\frac{(x-\mu_{nc})^2}{2\sigma_{nc}^2}}$$
$$f_{dc}(x) = e^{A_{dc}+B_{dc}\cdot x}$$
$$f_{ch}(x) = A_{ch} \cdot e^{-\frac{(x-\mu_{ch})^2}{2\sigma_{ch}^2}}$$

For convention, in this work the Region of Interest (ROI) for the Background is chosen in such a way to include all the particles (either Channeled or not), while the ROI for the Channeling signal is defined between $\mu_{ch} - 3\sigma_{ch}$ and $\mu_{ch} + 3\sigma_{ch}$.

In order to compute correctly the efficiency, three quantities must be computed. I_{Tot} is the Global function integral over all the space considered, that spans from -1000 μrad to +1500 μrad

$$I_{Tot} = \int_{-1000}^{+1500} (f_{nc} + f_{dc} + f_{ch})dx$$

I_{Bkg} is the Background function integral over all the space considered, that spans from -1000 μrad to +1500 μrad as in the former case. It includes the contribution due to Non Channeling, Multiple Scattering, Divergence effects and Dechanneling

$$I_{Bkg} = \int_{-1000}^{+1500} (f_{nc} + f_{dc})dx$$

I_{Ch}^{Int} is the integral of the function representing the channeling over the Channeling ROI, defined earlier as the angular positions between $\mu_{ch} - 3\sigma_{ch}$ and $\mu_{ch} + 3\sigma_{ch}$

$$I_{Ch}^{Int} = \int_{\mu_{ch}-3\sigma_{ch}}^{\mu_{ch}+3\sigma_{ch}} f_{ch}dx$$

I_{Ch}^{Diff} is the difference of the total integral and the Background estimate

$$I_{Ch}^{Diff} = \int_{-1000}^{+1500} f_{ch}dx = I_{Tot} - I_{Bkg}$$

If the estimates are correct, $I_{Ch}^{Int} \approx I_{Ch}^{Diff}$. In this approximation a percent-order systematic error will be committed, so the relative error between these two values is

$$\frac{I_{Ch}^{Int} - I_{Ch}^{Diff}}{I_{Ch}^{Int}} = 1 - \frac{I_{Ch}^{Diff}}{I_{Ch}^{Int}} = 1 - \frac{\int_{-1000}^{+1500} f_{ch}dx}{\int_{\mu_{ch}-3\sigma_{ch}}^{\mu_{ch}+3\sigma_{ch}} f_{ch}dx}$$

The latter term can be decomposed, multiplying and dividing by 1 written as the full-domain integral of the gaussian function. After some calculation we get:

$$\frac{\int_{-1000}^{+1500} f_{ch}dx}{\int_{\mu_{ch}-3\sigma_{ch}}^{\mu_{ch}+3\sigma_{ch}} f_{ch}dx} = \frac{\int_{-1000}^{+1500} f_{ch}dx}{\int_{-\infty}^{+\infty} f_{ch}dx} \cdot \frac{\int_{-\infty}^{+\infty} f_{ch}dx}{\int_{\mu_{ch}-3\sigma_{ch}}^{\mu_{ch}+3\sigma_{ch}} f_{ch}dx} = 0.9987 \cdot 0.9973 = 0.9960$$

So, the percentual error between I_{Ch}^{True} and $I_0 - I_{Bkg}$ is the following

$$\frac{I_{Ch}^{Int} - I_{Ch}^{Diff}}{I_{Ch}^{Int}} = 1 - 0.9960 = 0.0040 = 4‰$$

This procedure helps in order to perform the background-disentanglement, because not all particles deflected with an angle comparable to the Bending Angle are necessary in Channeling: other background effects can give a "false positive" and spoil the further analysis, making such efficiency results unreliable. The efficiency $\mathcal{E}$ is straightforwardly calculated as follow and it has been proven that the value of I_{Ch}^{Diff} is greater than the value of I_{Ch}^{True} by 4 ‰

$$\mathcal{E} = \frac{I_{Ch}^{True}}{I_{Tot}} \approx \frac{(I_{Tot} - I_{Bkg})}{I_{Tot}}$$

Moreover using the two techniques at the same time will allow to crosscheck the validity of the background and signal fits.

4.3 400 GeV Protons from SPS

The aim of this section is to describe the experimental setup and the key results obtained for the Channeling efficiency in 2015 by UA9 collaboration at the SPS H8 extracted line with 400 GeV proton beam. These results will then be compared with those we obtained using the Geant4 simulation. With this crystallographic configuration the Channeling efficiency is expected to be different than the one obtained with the (111) plane. The (111) plane consists of wide and narrow planes. The barrier potential U_0 is equal to 22.5 eV and 7.6 eV for the wide and narrow planes respectively [7].
In these simulation, the Geant4 Channeling example is compiled, built and run. The data cards are used to define the correct crystal parameters, and the beam characteristics.

4.3.1 Channeling measurement with protons at CERN H8 SPS Extraction Line

The experiment was carried out at the H8 beam line of the CERN SPS using a 400 GeV proton beam. The layout of the experiment is shown in Figure 4.3. A high precision goniometer was used to orient the crystal planes with the respect to the beam axis with an accuracy of 2 μrad [17]. Five pairs of silicon microstrip detectors, two upstream and three downstream of the crystal, were used to measure incoming and outgoing angles of particles with an angular resolution of about 3 μrad. The geometric parameters of the incident beam were measured with the help of the detector telescope. The width of the beam along the horizontal and vertical axes was a few millimeters. The angular divergence of the incident beam in the horizontal and vertical planes was $\sim$10 μrad for the proton beam. The system of microstrip detectors in its normal configuration provides measurements only for particle deflection angles smaller than 1.5 mrad because at larger angles deflected particles would miss the last downstream detector [17].

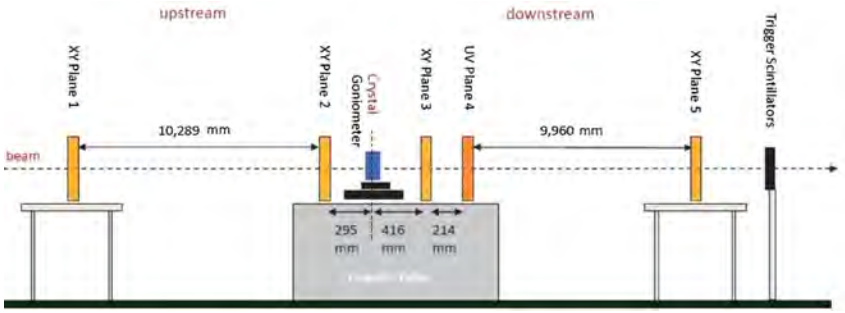

Figure 4.3. 400 GeV protons H8 CERN Transfer Line experimental setup. XY Plane 1–5 are the silicon strip detectors. The bent crystal mounted on the goniometer is installed between strip detectors 2 and 3 [17].

Particles incident on the crystal at a small angle (less than the critical angle for Channeling, θ_c) relative to the (111) crystallographic plane have a high probability to be captured into the Channeling regime.
The total capture probability for the (111) plane in a silicon crystal and large bending radii was defined in the following way. As is known, the (111) plane consists of wide and narrow planes. The potential barrier U_0 equals 22.5 eV and 7.6 eV for the wide and narrow planes, respectively. To capture particles into the channeling regime, it is necessary to fulfill the condition

$$\frac{E_0\theta^2}{2} + U(x) \leq U_0$$

where E_0 is the particle energy, $U(x)$ is the potential function, and $\theta < \theta_c$ is the incident particle angle with respect to the z axis.

4.3.2 Configuration and geometry of the Geant4 simulation

A simplified geometry description of the CERN SPS H8 experimental setup is available in the Geant4 release 10.05.p01 as a test example. It includes the main tracker telescope components, the crystal and the particle gun.

The geometry includes the bent Si crystal with three Si detectors placed at -9.998 m (T1), -0.320 m (T2) and 10.756 m (T3) with respect to bent crystal position. The primary events are 400 GeV protons, outgoing from a Gun Particle Source placed at -10.500 m from the crystal with $\sigma'_x = 13.36\ \mu rad$ and $\sigma'_y = 11.25\ \mu rad$ divergence. The geometry is shown in the Figure 4.4.

In SPS configuration the energy of the particles impinging on the crystal is E=400 GeV and the Silicon Potential Well takes a value of U=22.5 eV. The crytical angle can be computed as follow:

$$\theta_c = \sqrt{\frac{2U}{E}} = \sqrt{\frac{2 \cdot 22.5\ eV}{400 \cdot 10^9\ eV}} = 10.6\ \mu rad$$

In order to verify how the simulation reproduces the Channeling with 400 GeV protons, we simulated the H8 experimental setup. We performed a single simulation,

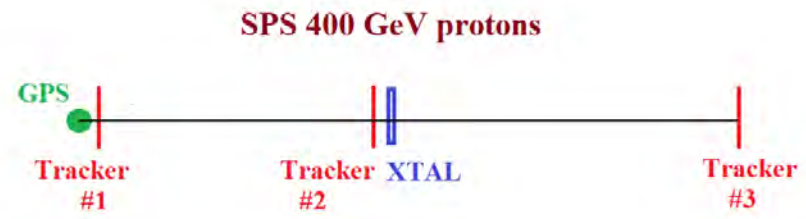

Figure 4.4. Geant4 geometry for SPS-H8 setup with 400 GeV protons Transfer Line simulations.

consisting of 50000 protons, with the crystal oriented in Channeling. In order to replicate the angular cut imposed by W. Scandale and A.M. Taratin in [17], we decided to set $\sigma'_x = 2.5\ \mu rad$, in such a way to have the 95.4% of the beam in the angular region delimited by $|\theta_{x0}| < 5\ \mu rad$. The Deflection Angle distribution is reported below, in Fig. 4.5.

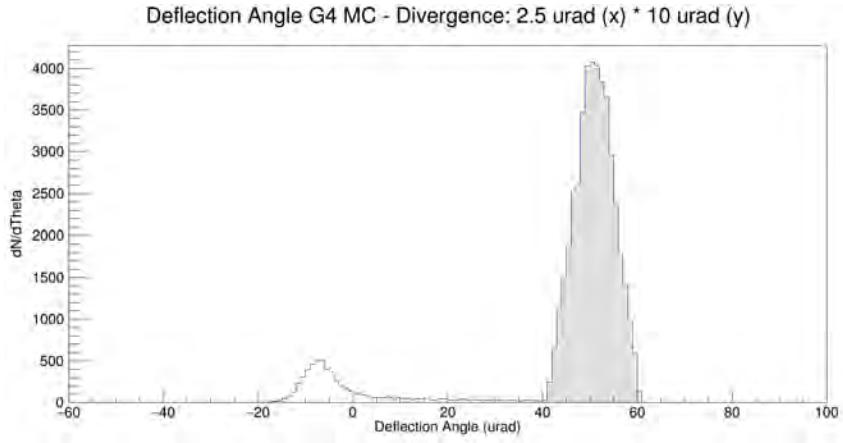

Figure 4.5. Deflection Angle distribution for 400 GeV protons obtained with Geant4 simulation performed with $\sigma'_x = 2.5\ \mu rad$ and $\sigma'_y = 10\ \mu rad$.

The Channeling efficiency value, computed with the method described in Sec. 4.2, is the following:

$$\mathcal{E} = \frac{I_{Ch}^{True}}{I_0} = 75.30 \pm 0.68\%$$

4.3.3 Comparison with H8 Extraction Line Data

The experimental Channeling measurements results are shown in Figure 4.6, reproduced by the original article [17] by W. Scandale and A.M. Taratin. An angular cut on the impinging particles was performed offline at analysis level: the Channeling efficiency claimed for 400 GeV protons in [17] is obtained imposing the condition $|\theta_{x0}|, |\theta_{y0}| < 5\ \mu rad$ before the analysis. In Fig. 4.6 the Deflection Angle distribution is reported in linear scale (a) and logarithmic scale (b).

The peak on the left side in Fig. 4.6(a) and 4.6(b) is due to particles which were not captured into the channeling states at the crystal entrance. Particles with

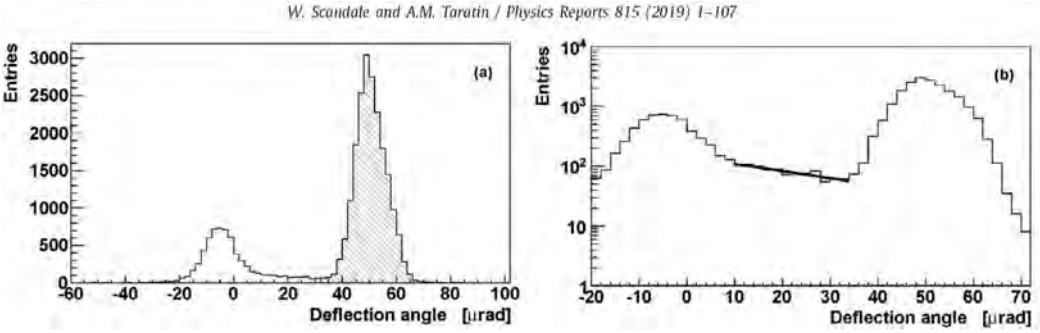

Figure 4.6. Deflection Angle distribution for 400 GeV protons in the silicon crystal bent along (110) planes. The crystal length is 1.94 mm. Only particles hitting the crystal with the horizontal and vertical angles $|\theta_{x0}|, |\theta_{y0}| < 5\mu rad$ were selected. (a) The deflected fraction 76.6% is hatched. (b) Logarithmic scale along Y axis. Reproduced by [17].

deflection angles between the two maxima in Fig. 4.6 are the dechanneled ones [17]. The Channeling efficiency claimed by W. Scandale and A.M. Taratin is referred to selected particles after an angular cut, meanwhile no cuts and/or other limiting factor over the Geant4 simulations were put, so we expect to have comparable efficiencies.
A further useful comparison can be given putting side-by-side our plot obtained with Geant4 and W. Scandale plot.

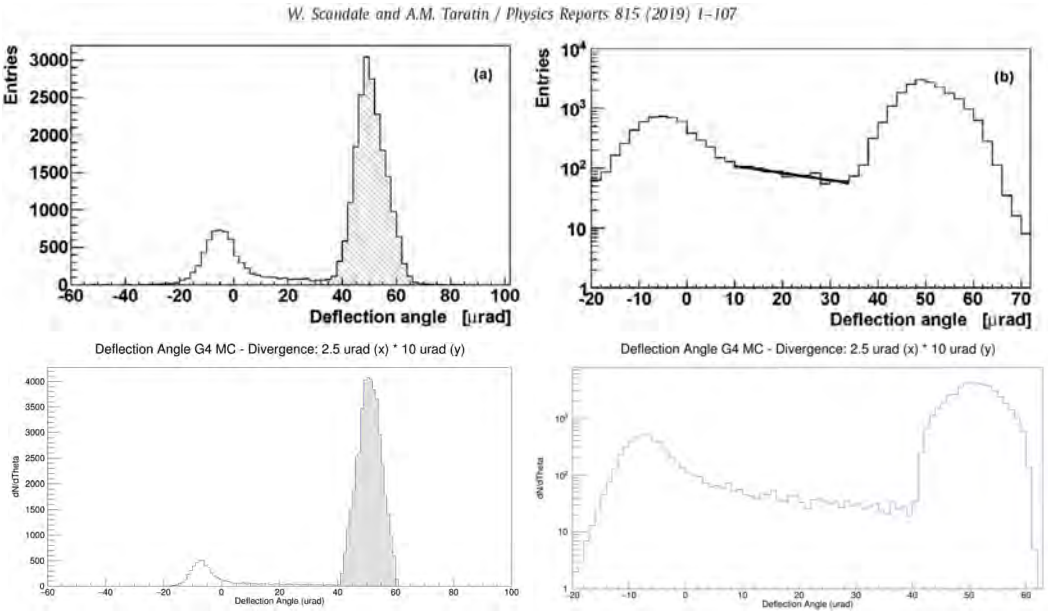

Figure 4.7. Deflection Angle distribution for 400 GeV protons by Scandale/Taratin data (Top) and Geant4 simulation (Down).

It is evident that the 400 GeV p Geant4 simulation matches well the data for protons as expected. The efficiencies values obtained $\mathcal{E}_{G4} = (75.30 \pm 0.68)\%$ and $\mathcal{E}_{ST} = 76\%$ respectively also show a very good agreement.

4.4 Leptons Channeling at Mainz Mikrotron

The aim of this section is to describe the experimental setup and the results on Channeling efficiency obtained with electrons in 2014 by the INFN Ferrara team [14] at the Mainz Mikrotron. These results will then be compared with those obtained by our Geant4 simulation, as already reported in Section 4.1, Rechanneling effects have not been implemented yet in the Geant4 10.05.p01 routine and the simulation is carried only for the (110) plane. With this crystallographic configuration the Channeling efficiency is expected to be different with respect to the one obtained with the (111) plane.
The crystal critical angle can be computed as follow:

$$\theta_c = \sqrt{\frac{2U}{E}} = \sqrt{\frac{2 \cdot 22.5\ eV}{855 \cdot 10^6\ eV}} = 217\ \mu rad$$

In order to have a clean Channeling peak disentangling, the background must be reduced as much as possible. Due to geometrical and dynamical consideration, the beam divergence must be smaller than the critical (Lindhard) angle defined earlier. If the divergence of the beam is greater than θ_c:

- Some of the particles entering with an angle $\theta < \theta_c$ can undergo Channeling and the process has an efficiency $\mathcal{E} < 1$.

- The particles entering with an angle $\theta > \theta_c$ wouldn't be in the "acceptance region" and thus won't undergo planar Channeling. In this case the particle suffers Multiple Coulomb Scattering. The outgoing particle angular distribution is gaussian, with an RMS deflection angle given by [20]:

  $$\theta_0^{MS} = \frac{13.6\ MeV}{\beta cp} \cdot \sqrt{\frac{x}{X_0}}$$

  where $X_0 = 9.7$ cm is the Si radiation length, $p = \sqrt{E^2 - m^2}$ and $c = 1$ in natural units.

In addition, due to the fact that Multiple Scattering particles angular distribution is superimposed to the Channeling one, if the beam divergence is greater than the Lindhard angle, many particles under the Channeling Peak would be misidentified as channeled particles, despite undergoing just Multiple Scattering.
In the MAMI configuration the divergence was 70 and 30 μrad, along the horizontal and vertical directions respectively, much lower than the planar critical angle, 217 μrad at 855 MeV, and of the predicted Multiple Scattering RMS angle in the crystal, $\sim$270 μrad. Being the beam divergence much smaller with respect to the critical angle, all of the beam particles are considered to be in the channeling acceptance. For this reason trying to use a tracker before the crystal to measure their direction will be counterproductive, because its presence will induce Multiple Scattering, thus spoiling the excellent beam properties.

4.4.1 Channeling measurement with electrons at MAMI

The test described in this section were carried out in 2014 by the INFN-Ferrara group using a (111) quasimosaic bent Si crystal and microstrip Silicon INSULAB telescope tracker [13]. To study the crystallographic plane (111) the INFN-Ferrara group used a silicon crystal 30.5 $\pm$ 0.5 μm thick, with crystallographic orientations as in Figure 4.8a. The crystal was fabricated by starting with a 500 μm thick (211) Si wafer, and characterized by high-resolution x-ray diffraction, measuring a deflection angle of 905 $\pm$ 15 μrad for the (111) planes, corresponding to a radius of 33.5 mm (23 times the critical radius). The deflection angle was much higher with respect to the multiple scattering one. The experimental setup is shown in Figure 4.8.

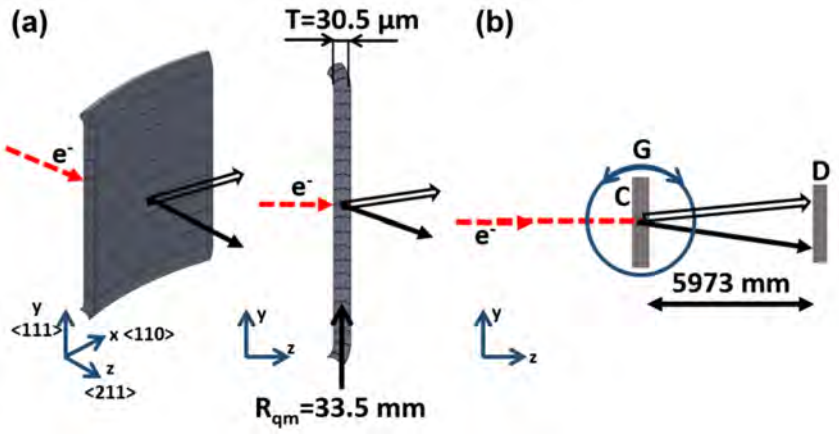

Figure 4.8. (a) Bending of a silicon platelike crystal with properly chosen crystallographic orientations generates the quasimosaic effect, resulting in a secondary bending of the planes lying in the crystal thickness. (b) Sketch of the experimental setup. The dashed arrow indicates the incoming beam, impinging on the crystal mounted on a high-precision goniometer (G). The solid-black arrow indicates particles deflected thanks to planar Channeling, while solid-white arrow correspond to overbarrier particles. A silicon detector, (D), reconstructs the beam profile after interaction with the crystal [14].

A 855 MeV electron beam, available at the Mainz Mikrotron (MAMI) facility, was steered to a beam size of 200 $\times$ 70 μm^2 and a divergence of 70 and 30 μrad along the horizontal and vertical directions, respectively. A Si detector INSULAB telescope, see Ref. [13] for its description, has been used to reconstruct the beam profile after the interaction with the crystal. The detector was placed 5973 mm downstream of the crystal and has an intrinsic spatial resolution better than 10 μm. The entire experimental setup was kept under vacuum to avoid Multiple Scattering of the beam by air. In order to perform an "angular scan", the crystal was rotated around the x axis and, for each angular position, the particle distribution after interaction with the crystal was recorded. The particle distribution after interaction with the crystal as a function of the crystal-beam angle is shown in Figure 4.9.

The crystal holder was mounted on a high-precision goniometer equipped with 5 degrees of freedom. Translations along the x and y axes were used to geometrically align the crystal with the beam with an accuracy of 1 μm, while rotations around

the x, y and z axes with an accuracy of 50, 9, and 175 μrad, respectively, were used to achieve angular alignment of the crystal planes with the electron beam.

In Figure 4.9a, the results of the crystal alignment scan performed at MAMI in 2014 are shown. The scan covers the angular region in between -700 μrad and +1500 μrad. Six different regions can be distinguished:

- The regions (1) and (6) are the Non-Channeling regions, where the crystal behaves as an amorphous material.
- The region (2) is the Channeling region, around to zero alignment angle. It indicates that the crystal has been correctly aligned in Channeling. In Fig. 4.9b the orange arrow represents this configuration. Under barrier particles are captured in the Channeling regime (CH) and deflected of the entire bending angle.
- The region (3) is the Dechanneling region, in which the leptons exit from the Channeling condition, obtaining a reduced deflection angle with respect to the Channeling bending angle. A fraction of dechanneled particles experiences Rechanneling (RCH). This effect is clearly visible in Fig. 4.9b.
- The region (4) is the Volume Reflection region, in which the leptons are mirrored by the crystal interplanar potential, as shown in the Fig. 4.9c by the green arrow. In this case the deflection is opposite to the crystal bending and the exit angle is negative.
- The region (5) is the Volume Capture region, in which the leptons are captured within the crystal planes, even if they entered with angles outside the the channeling admitted range as shown in the Fig. 4.9c by the blue arrow.

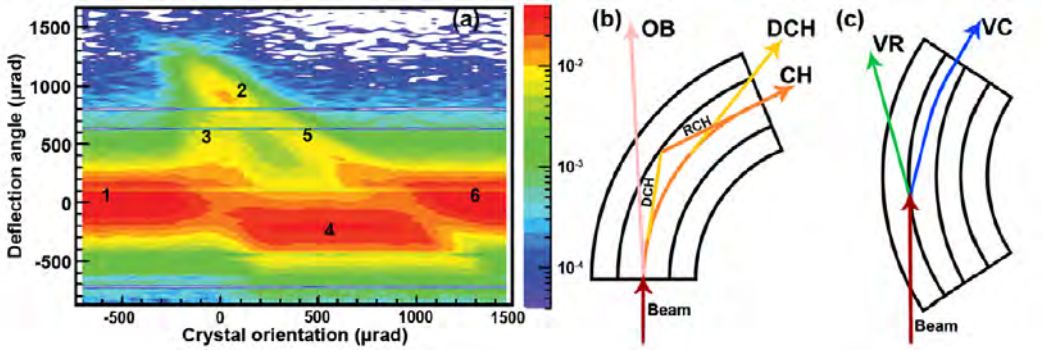

Figure 4.9. (a) An "angular scan" recorded during the interaction between the crystal and the electron beam at MAMI. (b) The bent crystal is aligned with respect to the charged particle beam to excite planar Channeling. (c) Bent crystal is aligned with respect to the incoming particle beam (red-dashed arrow) in such a way that the beam trajectory becomes tangent to the atomic planes inside the crystal [14].

Using MC authors of [14] have been able to estimate the different contribution to the channeling peak. Figure 4.10a illustrates the contributions of both single and

multiple Rechannelings to build up the "Channeling peak" shown in Figure 4.9a. In Fig. 4.10a the red line represents the whole distribution; black line the particles that have never been rechanneled; green, blue, and light blue lines the distribution of the particles rechanneled 1, 2, and 3 times, respectively. Figure 4.10b shows the fraction of channeled particles with and without taking into account the fraction of rechanneled electrons. Analysis of Monte Carlo simulation shows that about 55% of the particles recorded under the "Channeling peak" has been recycled once at least through Rechanneling. This strong contribution of Rechanneling to particle dynamics is a peculiarity of channeling with negatively charged particles. Because of crystal bending the fraction of channeled particles at the crystal entry face is not equal to unity because the centrifugal force renders asymmetric the potential, and some of the particles (impact parameter between 0 and 0.6 Å) are not channeled [14].

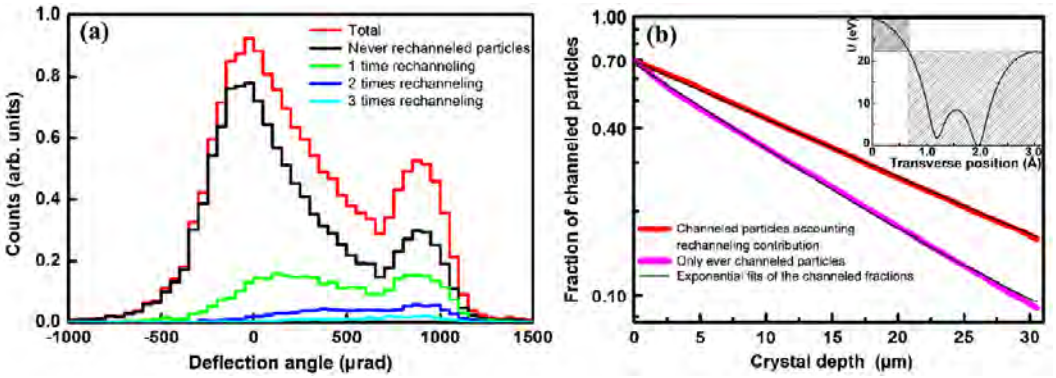

Figure 4.10. (a) Monte Carlo simulation of the contributions to the angular distribution originated from rechanneled particles. (b) The red curve represents the fraction of channeled particles summing up the contribution of never dechanneled particles and rechanneled particles. The magenta curve represents the fraction of never dechanneled particles [14].

In Figure 4.11, shows the measured Deflection Angle during the MAMI data taking together with simulations. The (a) curve corresponds to the particles deflected in Volume Reflection and Volume Capture conditions when crystal was rotated of $\sim$500 μrad with respect to Channeling alignment angle. The (b) curve represents the Channeling distribution, obtained with the crystal correctly aligned.

A Gaussian fit of the distribution was used to estimate the deflection angle of 910 ± 5 μrad [14]. The fraction of deflected particles within $\pm 3\sigma$ around the Channeling peak was $\mathcal{E} = 20.1 \pm 1.2\%$, a value in agreement with the simulation results $\mathcal{E}_{MC} = 21.2\%$ [14]. The left peak of the black curve of Fig. 4.11a is due to deflection of overbarrier particles, whose distribution is centered to the opposite direction as that of Channeling. The distribution is asymmetric because of the contribution of rapidly dechanneled particles on the right side. VR occurs with lower efficiency with respect to higher-energy experiments (like H8 SPS one) because of a larger probability of competitive VC at lower energies. In fact, VC is aided by incoherent scattering, which favors the transition from overbarrier to Channeling states, and that becomes stronger at lower energies, especially for negatively charged particles [14].

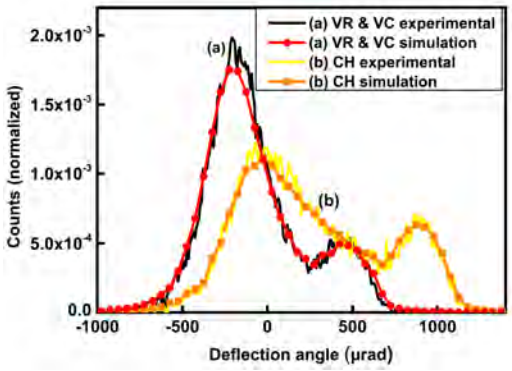

Figure 4.11. (a) Beam profile with the crystal aligned for VR and VC: solid line for experimental and dash line with dots for simulation. A largest fraction of the beam is steered toward the direction opposite of Channeling (left peak). VR efficiency is limited by VC (smaller right peak), deflecting particles along the crystal bending. (b) Beam profile with the crystal aligned for Channeling (solid line experimental, line with squares simulation). A large fraction of the beam is deflected to the nominal deflection of the crystal (right peak). Particles found in over barrier states at the crystal entry face populate the left peak in the distribution, while the region between the two peaks is populated by particles suffering Dechanneling. [14].

4.4.2 Configuration and geometry of the simulation

In order to reproduce the observations described in the previous section, we implemented the MAMI test beam setup inside the Geant4 10.05.p01 Channeling Example.

The geometry implemented and shown in the figure 4.12, consists of a bent Si crystal with three Si detectors placed at -0.190 m (T1), -0.100 m (T2) and 1.00 m (T3) with respect to bent crystal position. The bent crystal parameters were set up according to the MAMI crystal parameters (Bending Radius, thickness, transverse dimensions and impinging angle of the beam). The Geant4 primary particles were 855 MeV electrons or positrons, generated by a Gun Particle Source placed at -0.2 m from the crystal with $\sigma'_x = 70\ \mu rad$ and $\sigma'_y = 30\ \mu rad$ divergence.

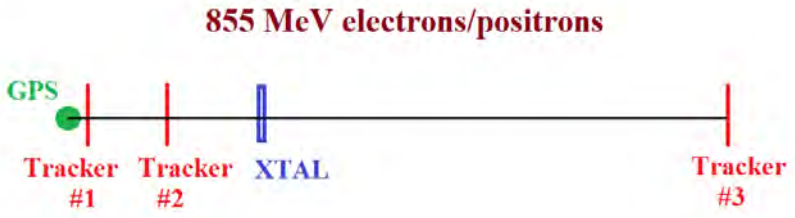

Figure 4.12. Geant4 geometry for Mainz Mikrotron setup with 855 MeV electrons and positrons simulations.

The geometry implemented is slightly different with respect to the one actually used by Bagli et al in [14]. Nevertheless the differences doesn't affect the results, because the beam spot was very small and we just use the outgoing angle measurement (angXout) in Geant4, which is independent from the actual position of the silicon

detectors.

4.4.3 855 MeV e^- simulation

In order to reproduce the angular scan shown in Fig. 4.9 we performed and extensive simulation campaign, changing the crystal alignment angle. The crystal angle ranges form -500 μrad to +1500 μrad, in steps of 10 μrad. Each configuration of the simulations consist of 250000 electrons. The Deflection Angle Histogram and the Deflection Angle VS Crystal Orientation 2D-Plot are shown in Figure 4.13, (c) and (a) respectively. In order to have a quick comparison with MAMI experimental data, the plots of the article [14] are put aside the Geant4 simulation ones.

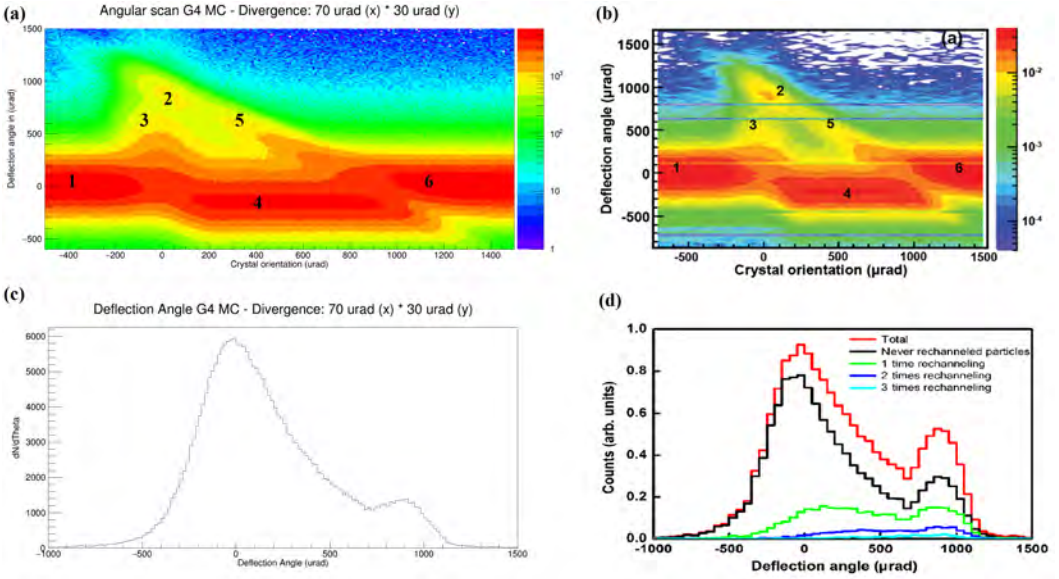

Figure 4.13. (a) Geant4 angular scan simulation for 855 MeV electrons in MAMI configuration. (b) MAMI angular scan recorded during the interaction between the crystal and the electron beam [14]. (c) Geant4 Deflection Angle Histogram. (d) MAMI Deflection Angle Histogram of final state particles. Only the "Never Rechanneled Particles" plot must be considered [14]. Simulation (a) and (c) performed with $\sigma'_x = 70$ μrad and $\sigma'_y = 30$ μrad 855 MeV positrons beam in MAMI configuration. The numbers superimposed to (a) and (b) 2D-Plots have the same meaning as in Figure 4.9a.

The results of Geant4 simulation in Figure 4.13c show a qualitatively very good agreement with the data collected at MAMI in Figure 4.13d. All of the effects are well reproduced including the Channeling deflection angle. The value obtained using the Geant4 simulation is (900 ± 4) μrad, in good agreement with the value 910 ± 5 μrad obtained in Ref [14]. Concerning the six regions previously described in Figure 4.13a/c, there are some differences in particular in the region between 2 and 3 where the separation appears to be less pronounced in the Geant4 simulation. This is confirmed by the Channeling peak in Figure 4.13c/d which is also less pronounced with respect to simulation in Ref [14].
This discrepancy was in fact expected due to the absence in the Geant4 modeling of the Rechanneling effect, which helps in populating the Channeling peak, as visible

also in the Figure 4.13d.

The efficiency, computed with the method described in Sec. 4.2, is the following

$$\mathcal{E} = \frac{I_{Ch}^{True}}{I_0} = 14.6 \pm 1.3\%$$

lower than the value $\mathcal{E} = 20.1 \pm 1.2\%$ declared by [14].

4.4.4 Comparison with e^- MAMI data and Analytical Simulations

The plots do not have the same relative scale but the same color code. In [14] the simulation is carried out using the the (111) plane, while in Geant4 the (110) lattice plane is the only one available. The fraction of deflected particles within $\pm 3\sigma$ around the Channeling peak declared by E. Bagli et al. is equal to $\mathcal{E} = 20.1 \pm 1.2\%$ for the MAMI electrons configuration, a value in agreement with their MAMI simulation results (21.2%) [14].
In the Geant4 simulations, we obtain $\mathcal{E} = 14.6 \pm 1.3\%$. This difference is due to the fact that Rechanneling has not been implemented.
As reported in Section 4.1, about 55% of the particles recorded under the "Channeling peak" have been recycled at least once through Rechanneling (see Fig. 4.10b). The hypothetical Geant4 channeling efficiency, when Rechanneling will be implemented, should be upscaled by a factor 1.5 times the actual value, thus reaching $\mathcal{E} = 1.5 \cdot (14.6 \pm 1.25)\% = (21.9 \pm 1.9)\%$. The rescaled value is in good agreement with the Channeling efficiency measured experimentally (20.1 ± 1.2 %) and the MAMI simulation result 21.2%. The results are fully compatible despite the fit on the Deflection Angle Histogram does not reproduce very well the Dechanneling region between 200 μrad and 700 μrad (see Figure 4.14). In addition the Geant4 simulation is carried on the (110) plane. With this crystallographic configuration the Channeling efficiency is different with respect to the one obtained with the (111) plane.

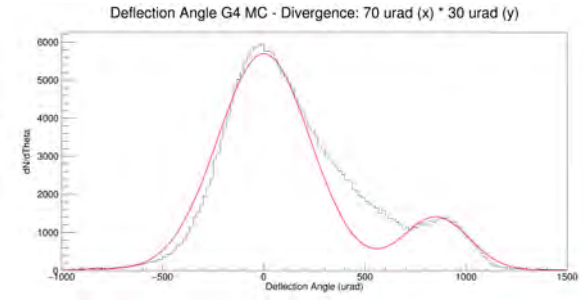

Figure 4.14. Fit of the Deflection Angle Histogram reported in Figure 4.13c.

Given the above described differences the simulations show a good compatibility with data and we can consider the Geant4 Channeling Routine benchmark with MAMI data satisfactory.

It is also useful to compare these results with the one obtained another independent simulation code developed by Prof. V. Biryukov on the (111) plane. His code [5, 6] includes Rechanneling as in the case of the MAMI simulation in [14].

Despite the fact that the results are still unpublished, we received them privately by prof. V. Biryukov himself.
V. Biryukov results are reported in Figure 4.15. All the relevant Deflection Angle Histograms are normalized with respect to their channeling peaks.

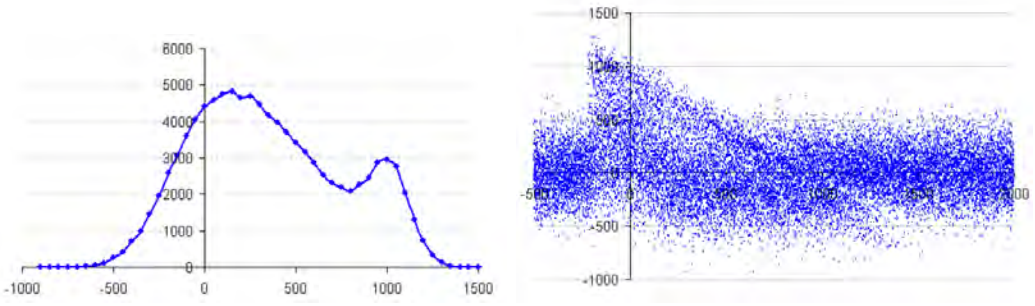

Figure 4.15. (a) Deflection Angle Histogram and (b) 2D-Plot Deflection Angle VS Crystal orientation Angle. Simulation performed with $\sigma'_x = 70\ \mu rad$ and $\sigma'_y = 30\ \mu rad$ 855 MeV electrons beam in MAMI configuration.

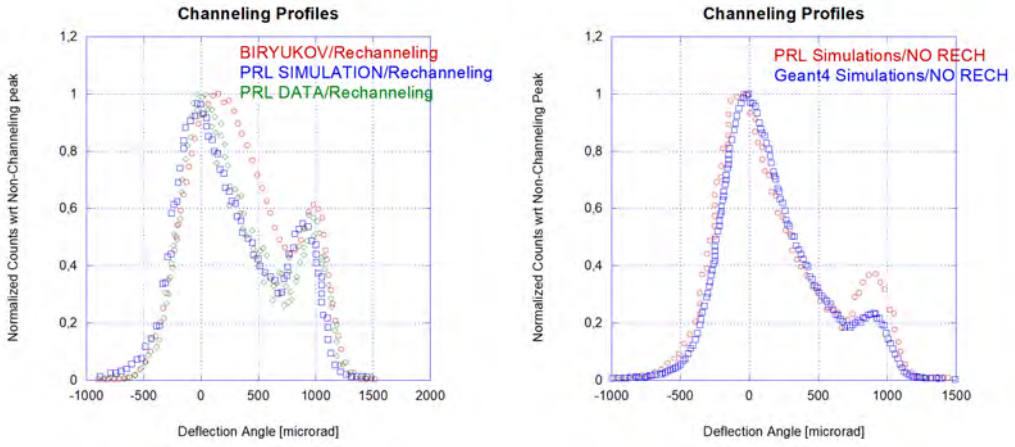

Figure 4.16. (a) Comparison of the results concerning the simulations in which Rechanneling has been implemented. In red, Biryukov simulations (see Fig. 4.15a). In green and blue, MAMI experimental data (Fig. 4.11b, orange dotted line) and MAMI simulations are reported (Fig. 4.10a, red line). (b) Comparison of the results concerning the simulations in which Rechanneling has not been implemented or not considered. In blue, Geant4 simulations carried along the (110) lattice plane. In red, MAMI simulations without Rechanneling (Fig. 4.10a, red line).

The fraction of deflected particles within $\pm 3\sigma$ around the Channeling peak declared by V. Biryukov is equal to $\mathcal{E} = 12 \pm 1\%$ for MAMI electrons configuration, a value in disagreement either with the Geant4 simulation results and the experimental MAMI result, despite V. Biryukov simulations shows an efficiency slightly lower than the MAMI and Geant4 ones. After these considerations (lack of Rechanneling in Geant4, use of the (110) instead of (111) planes), it can be stated that the

Geant4 simulations for electrons in MAMI configuration are compatible with MAMI simulations in which Rechanneling was not considered. Meanwhile, the simulations performed by Prof. V. Biryukov, show lower Channeling efficiency. As already mentioned the code used by Biryukov is described in [5, 6].

4.4.5 855 MeV e^+ simulation

In order to study the effect of Sub-GeV Channeling with positrons, never explored before to our knowledge, we simulated an experiment using the same beam of the MAMI measurement but made of positrons instead of electrons. We performed an extensive simulation campaign also for this configuration for which no data exist. The crystal orientation angle was changed form -500 μrad to +1500 μrad, in steps of 10 μrad. Each configuration of the simulations consist of 250000 positrons. The Deflection Angle Histogram and the Deflection Angle VS Crystal Orientation 2D-Plot are shown in Figure 4.17, (a) and (b) respectively.

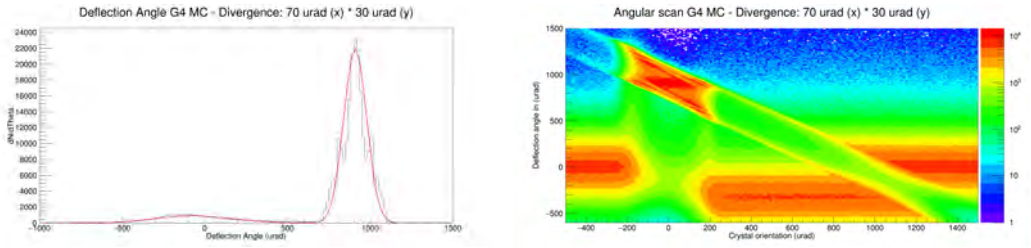

Figure 4.17. (a) Deflection Angle Histogram and (b) 2D-Plot Deflection Angle VS Crystal orientation Angle. Simulation performed with $\sigma'_x = 70$ μrad and $\sigma'_y = 30$ μrad 855 MeV positrons beam in MAMI configuration.

The Channeling efficiency has been computed just defining as the number of "channeled particles" (N_{Ch}) the integral of the distribution in Fig. 4.17a from 650 μrad to 1500 μrad and dividing this value by the total number of simulated events (N_{Tot}=250000)

$$\mathcal{E} = \frac{N_{Ch}}{N_{Tot}} = 86.20 \pm 0.25\%$$

The Channeling angle has been determined fitting the Channeling peak with a gaussian. We obtained the value $\theta = (907 \pm 1)$ μrad. This is comparable with the $\theta = (915 \pm 1.2)$ μrad obtained at MAMI [14].

4.4.6 Comparison with e^+ Analytical Simulation by V. Biryukov

To our knowledge nobody tried to search for Sub-GeV positron Channeling, therefore no data exist to benchmark the simulations in this case. In order to check the Geant4 results, only simulations by Prof. V. Biryukov can be used as comparison. Also in this case his results are based on the code described in [5, 6]. The distribution of the positrons angle after crossing the crystal is shown in Figure 4.18.

Qualitatively, the two plots shows the same physical effects related to the coherent processes in the bent crystal. Also in this case the Geant4 simulation is on the (110) lattice plane. Applying the same method described in the previous

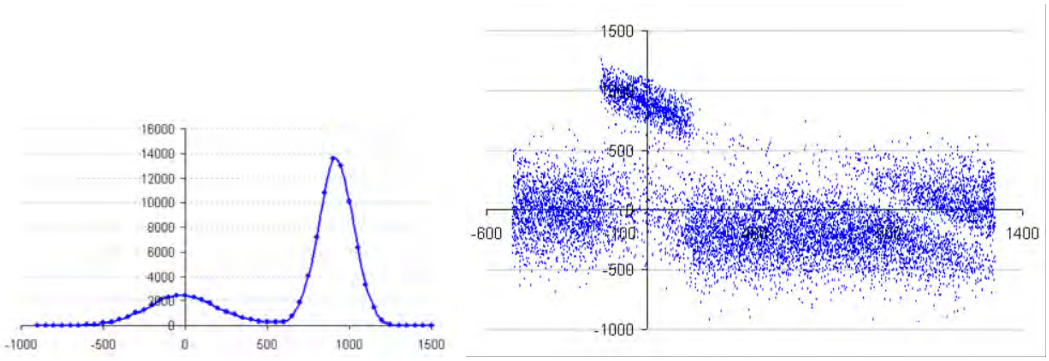

Figure 4.18. (a) Deflection Angle Histogram and (b) 2D-Plot Deflection Angle VS Crystal orientation Angle. Simulation performed with $\sigma'_x = 70\ \mu rad$ and $\sigma'_y = 30\ \mu rad$ 855 MeV positrons beam in MAMI configuration.

Section, we obtained for Prof. V. Biryukov simulations, a Channeling efficiency of $\mathcal{E} = 88.8 \pm 0.3\%$ for MAMI positrons configuration. This value is just a little higher with respect to the one obtained in Geant4 simulation: $\mathcal{E} = 86.2 \pm 0.3\%$.

It is important to remark that all the errors are only statistical and we don't expect the results to be the same due to the fact that Prof. V. Biryukov performed the simulations with (111) crystallographic plane, while in Geant4 the (110) lattice plane was used.

Based on this considerations, we are now ready to use the Geant4 simulations to study the SHERPA setup.

4.5 Leptons channeling with SHERPA at LNF BTF-II

The aim of this section is to describe the simulations performed in order to constrain the BTF beam RMS spot size and divergence needed to allow the SHERPA test beam to successfully observe Channeling at LNF. The main goal is to observe the channeling with positrons, and eventually also with electrons. The experimental configuration simulated represents the present geometry of the SHERPA beam test setup. Nonetheless the simulations program we prepared can in the future be used also to study the bent-crystal assisted DAΦNE ring configuration [10].

In the simulations, the beam divergence angle σ'_x will be changed in order to study its relation with the Channeling efficiency. Due to the fact that the planar Channeling manifests itself as an x-axis displacement, the vertical beam divergence σ'_y is not relevant for this study and will be kept fixed.
In addition, to take into account the fact that SHERPA will not be able to measure the incoming angle and position of the particles, we added to the simulation the dimension of the beam spot to be $1 \times 1\ mm^2$ RMS.

The obtained results will then be compared with those of Prof. V. Biryukov, for both positrons and electrons.

4.5.1 Configuration and geometry of the SHERPA setup

We have implemented in the Geant4 code a simplified version of the SHERPA experimental setup.
The geometry consists of a bent Si crystal with three Si detectors placed at -0.190 m (T1), -0.100 m (T2) and 2.00 m (T3) with respect to bent crystal position. The primary events are 511 MeV electrons or positrons, produced by a Particle Gun placed at -0.2 m from the crystal with a vertical angle divergence of $\sigma'_y = 300\ \mu rad$ and a variable horizontal divergence that ranges from $\sigma'_x = 0\ \mu rad$ to $\sigma'_x = 1000\ \mu rad$ in step of $\Delta\sigma'_x = 100\ \mu rad$. The geometry is shown in Figure 4.19.

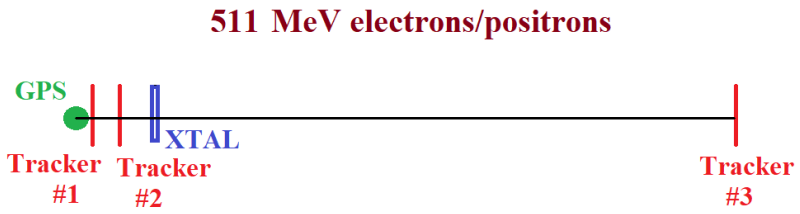

Figure 4.19. Geant4 geometry for LNF Beam Test Facility setup with 511 MeV electrons and positrons simulations.

Being the energy of the particles E=511 MeV the value of the the Lindhard angle will be for SHERPA:

$$\theta_c = \sqrt{\frac{2U}{E}} = \sqrt{\frac{2 \cdot 22.5\ eV}{511 \cdot 10^6\ eV}} \approx 300\ \mu rad$$

In this conditions, an incoming beam divergence less than 500 μrad would be ideal to avoid important acceptance loss for the channeling process due to particles impinging the crystal with $\theta > \theta_c$.
Having an higher beam divergence and trying to use a tracker to measure incoming direction and select in Channeling particles at analysis level would not work. In fact, at so low energies, the Multiple Scattering angle induced by even just 100 μm thick silicon sensor, will be as big as 470 μrad. Using a tracker the information on the impinging direction of the particle on the crystal surface will be in any case spoiled, while the incoming beam angular dispersion increased. Furthermore, the available free space in BTF-II hall is limited, thus putting 4 tracker planes less than a meter apart makes no sense as the angular resolution would be too large. Assuming i.e the planes are put 25 cm each other, the angular resolution $\sigma(\theta)$ is given by the pixel detector position resolution $\sigma(x)$ divided by the tracker distance d. Given the detector pixel size, p, the angular resolution is given by:

$$\sigma(\theta) = \frac{\sigma(x)}{d} = \frac{p}{\sqrt{12}}\frac{1}{d} = \frac{55 \cdot 10^{-6}\ m}{\sqrt{12} \cdot 0.25\ m} = 63\ \mu rad$$

So, it is unnecessary to have a telescope in the SHERPA configuration.

4.5.2 511 MeV e^+ simulation

In order to put constraints on LNF BTF beam RMS x and y size and divergence, the simulations have been performed with different divergence values and for each value the angular scan changing the crystal orientation has also been made. Each configuration of the simulations consist of 50000 positrons. For σ'_x =0, 100, 200, 300, 400, 500, 600, 700, 800, 1000 μrad, the Deflection Angle Histogram and the Deflection Angle VS Crystal Orientation 2D-Plot are shown in Figure A.1, A.2, A.3, A.4, A.5, A.6, A.7, A.8, A.9, A.10, (a) and (b) respectively. In order not to make the discussion too heavy, the Figures are reported in the Appendix A. In the Figure 4.20 only the cases $\sigma'_x = 200\ \mu rad$, $\sigma'_x = 500\ \mu rad$, $\sigma'_x = 1000\ \mu rad$ are shown.

The divergence effect is clearly visible in both plots. As the σ'_x increases, the Amorphous peak variance increases, because it is the sum in quadrature of the divergence itself and the 470 μrad Multiple Scattering contribution. If the beam divergence is greater than $\theta_c = 300\ \mu rad$, some of the particles entering with an angle $\theta < \theta_c$ can undergo Channeling and the process has an efficiency $\mathcal{E} < 1$. The particles entering with an angle $\theta > \theta_c$ wouldn't be in the "acceptance region" and thus won't undergo planar Channeling. In this case the particle suffers Multiple Coulomb Scattering.

If we analyze the 2D-Plots, it is even more evident that the bigger the divergence, the worse the Channeling peak. In Fig. 4.20 Top/Right, corresponding to $\sigma'_x = 200\ \mu rad$, the Channeling peak is visible and well-separated from the Background and the Dechanneling region is not too much populated. This is due to the fact that positrons suffer much less Dechanneling with respect to electrons, as reported in Chapter 1.1.6. When the divergence is increased, the Channeling peak is less populated, meanwhile the Non-Channeling/Amorphous region accounts for divergence effects (Fig. 4.20 Mid/Rigth, corresponding to $\sigma'_x = 500\ \mu rad$). In Fig. 4.20

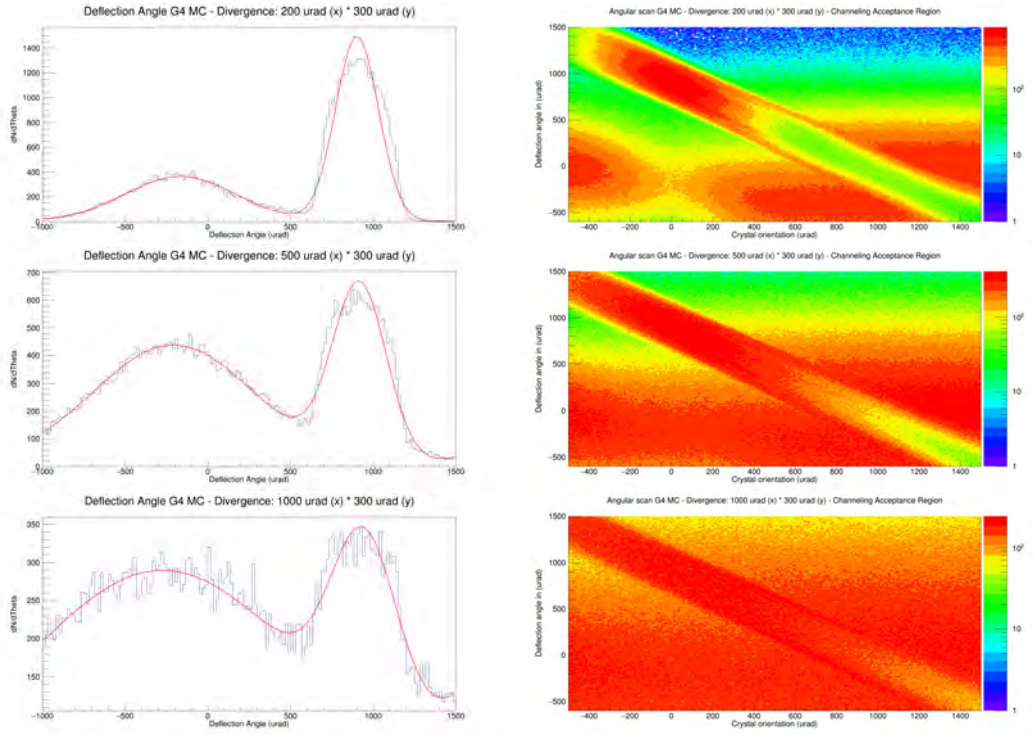

Figure 4.20. (Left column) Deflection Angle Histogram and (Right column) 2D-Plot Deflection Angle VS Crystal orientation Angle. Simulation performed with $\sigma'_y = 300$ μrad 511 MeV positron beam in SHERPA LNF BTF configuration. (First row) $\sigma'_x = 200$ μrad; (Second row) $\sigma'_x = 500$ μrad; (Third row) $\sigma'_x = 1000$ μrad.

Bottom/Rigth, corresponding to $\sigma'_x = 1000$ μrad, it is still relatively easy to identify the Channeling peak and the detection efficiency is still high with respect to the electron case. Also in this case, while performing the analytical detection efficiency calculation, the fitting algorithm must be very accurate to disentangle the signal against the background.

For each set of simulations the Channeling detection efficiency $\mathcal{E}$ is computed with the method described in Sec. 4.2. The results are given in the Table 4.1.

The Channeling detection efficiency is expected to be lower than product of the number of particles inside the angular region $\pm\theta_c$ (acceptance Acc) and the channeling efficiency at zero divergence.

$$\mathcal{E}^{max}(\sigma') = Acc \times \mathcal{E}(\sigma'_x = 0\ \mu rad) = \frac{\int_{-\theta_c}^{+\theta_c} g(x|\mu, \sigma')dx}{\int_{-\infty}^{+\infty} g(x|\mu, \sigma')dx} \times 0.85 \qquad (4.1)$$

The difference is due to the Multiple Scattering which can change the acceptance of the channeled particles and consequently their Channeling detection efficiency. The simulation shows that the Channeling detection efficiency for positrons stays high (>20%) for any divergence lower than 1 mrad.

The Acceptance, defined earlier, takes the following values reported in Table 4.1. The detection efficiencies $\mathcal{E}^{max}(\sigma')$ scaled by the Acceptance are also reported. The

tabulated value of the detection efficiencies are shown in a Scatter-Plot, in Figure 4.22. Red points on the plot represent positron simulations, green points are the maximal detection efficiencies computed according to the eq. (4.1).

$\sigma'_x[\mu rad]$	Det. Ch. Eff. $\mathcal{E}$ [%]	Acc= $\frac{\int_{-\theta_c}^{+\theta_c} g(x\|\mu,\sigma')dx}{\int_{-\infty}^{+\infty} g(x\|\mu,\sigma')dx}$	$\mathcal{E}^{max}(\sigma')$ [%]
0	85.03 ± 0.66	1	85.03
100	80.89 ± 0.67	0.9973	84.80
200	61.38 ± 0.73	0.8664	73.67
300	46.53 ± 0.79	0.6827	58.05
400	37.52 ± 0.86	0.5467	46.49
500	33.37 ± 0.89	0.4515	38.39
600	27.02 ± 0.97	0.3829	32.56
700	23.48 ± 1.03	0.3318	28.21
800	21.99 ± 1.05	0.2923	24.85
1000	18.89 ± 1.12	0.2358	20.05

Table 4.1. Channeling detection Efficiency for positrons. In the second column, the detection efficiency obtained fitting the angXout histogram. In the third column, the geometrical acceptance corrective factor. In the third column, the renormalized maximal detection efficiency computed according to the Equation 4.1.

4.5.3 511 MeV e^- simulation

In order to asses the possibility to observe electron channeling with SHERPA, we performed and extensive simulation campaign with electrons as well. For σ'_x =0, 100, 200, 300, 400, 500, 600, 700, 800, 1000 μrad, the Deflection Angle Histogram and the Deflection Angle VS Crystal Orientation 2D-Plot are shown in Figure A.11, A.12, A.13, A.14, A.15, A.16, A.17, A.18, A.19, A.20, (a) and (b). The Figures are collected in the Appendix A. In the Figure 4.21 only the cases $\sigma'_x = 200$ μrad, $\sigma'_x = 500$ μrad, $\sigma'_x = 1000$ μrad are shown.

It is important to remark that the fitting algorithm must be very accurate to disentangle the signal against the background due to the low Channeling detection efficiency of electrons, and therefore the uncertainties on the measured efficiency are higher. It appears that the observation with electrons will be much more challenging for SHERPA due to the low channeling efficiency of negatively charged particles. As a matter of fact we need to stress that in the real experiment the separation will appear slightly better, due to the absence of the Rechanneling effect in our simulation. In fact Rechanneling will in the real life help to populate the Channeling peak.

For each set of simulations the Channeling detection efficiency $\mathcal{E}$ is computed with the method described in Sec. 4.2. The results are given in the Table 4.2.

The Channeling detection efficiency is expected to be lower than product of the number of particles inside the angular region $\pm\theta_c$ (acceptance Acc) and the Channeling efficiency at zero divergence. The Rechanneling, not implemented in Geant4, makes the detection efficiency higher by a factor $C_{Rech} = 1.5$ (see Section

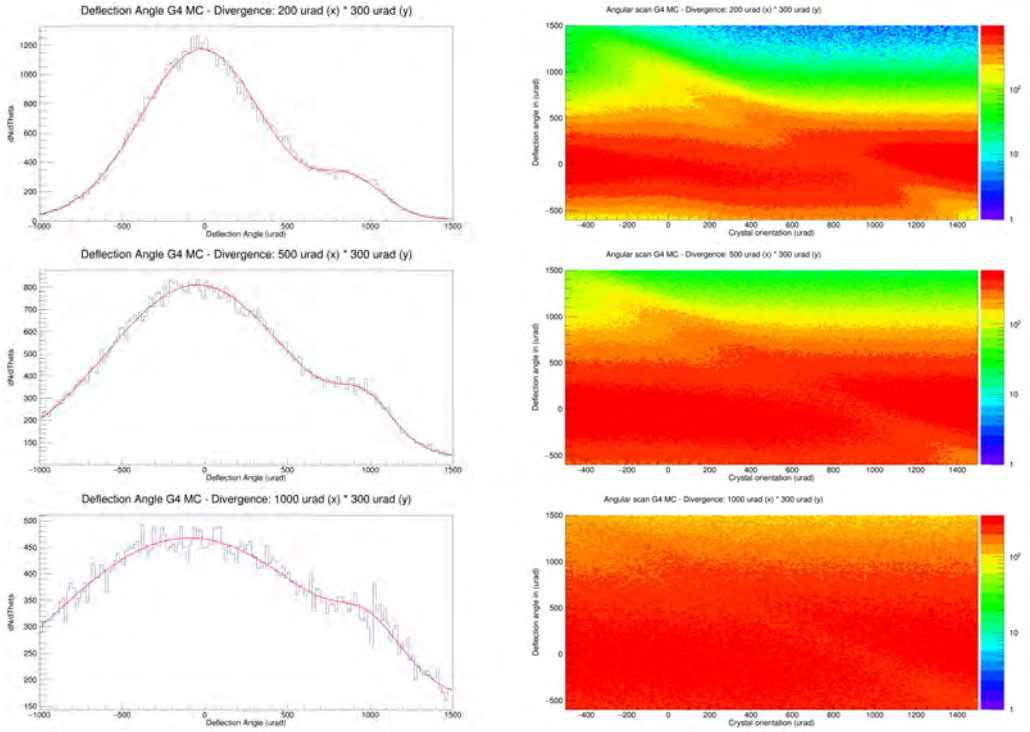

Figure 4.21. (Left column) Deflection Angle Histogram and (Rigth column) 2D-Plot Deflection Angle VS Crystal orientation Angle. Simulation performed with $\sigma'_y = 300$ μrad 511 MeV electron beam in SHERPA LNF BTF configuration. (First row) $\sigma'_x = 200$ μrad; (Second row) $\sigma'_x = 500$ μrad; (Third row) $\sigma'_x = 1000$ μrad.

4.1).

$$\mathcal{E}(\sigma')^{max}_{Rech} = Acc \times \mathcal{E}(\sigma'_x = 0\ \mu rad) \times C_{Rech} = \frac{\int_{-\theta_c}^{+\theta_c} g(x|\mu,\sigma')dx}{\int_{-\infty}^{+\infty} g(x|\mu,\sigma')dx} \times 0.12 \times 1.5 \quad (4.2)$$

$$\mathcal{E}(\sigma')^{max}_{NoRech} = Acc \times \mathcal{E}(\sigma'_x = 0\ \mu rad) = \frac{\int_{-\theta_c}^{+\theta_c} g(x|\mu,\sigma')dx}{\int_{-\infty}^{+\infty} g(x|\mu,\sigma')dx} \times 0.12 \quad (4.3)$$

The Acceptance, defined earlier, takes the following values reported in Table 4.2. The detection efficiencies $\mathcal{E}(\sigma')^{max}_{NoRech}$ renormalized by the Acceptance are reported aside. The tabulated value of the detection efficiencies are reported in a Scatter-Plot, in Figure 4.22 at the end of the chapter. Red points on the plot represent electrons simulations, green points are the maximal detection efficiencies computed according to the eq. (4.3), without considering Rechanneling.

Also in this case the difference between the detection efficiency obtained via the fits and the one obtained multiplying the zero-divergence efficiency by the corrective factor (Acc) is due to the Multiple Scattering which can change the acceptance itself of the channeled particles and their Channeling detection efficiency. The simulation shows that the Channeling detection efficiency for electrons are slightly lower (6-7 times) than the positron ones, as expected [2].

$\sigma'_x[\mu rad]$	Det. Ch. Eff. $\mathcal{E}$ [%]	Acc= $\frac{\int_{-\theta_c}^{+\theta_c} g(x\|\mu,\sigma')dx}{\int_{-\infty}^{+\infty} g(x\|\mu,\sigma')dx}$	$\mathcal{E}^{max}_{NoRech}(\sigma')$ [%]
0	12.11 ± 1.36	1	12.11
100	12.90 ± 1.32	0.9973	12.08
200	10.47 ± 1.45	0.8664	10.49
300	8.24 ± 1.62	0.6827	8.27
400	7.29 ± 1.72	0.5467	6.62
500	5.95 ± 1.89	0.4515	5.47
600	4.66 ± 2.12	0.3829	4.64
700	5.24 ± 2.00	0.3318	4.02
800	3.28 ± 2.51	0.2923	3.54
1000	2.83 ± 2.70	0.2358	2.86

Table 4.2. Channeling detection Efficiency for electrons. In the second column, the detection efficiency obtained fitting the angXout histogram. In the third column, the geometrical acceptance corrective factor. In the third column, the renormalized maximal detection efficiency computed according to the Equation 4.3. In order to consider Rechanneling, it is necessary to multiply those values by 1.5, as reported in Section 4.1

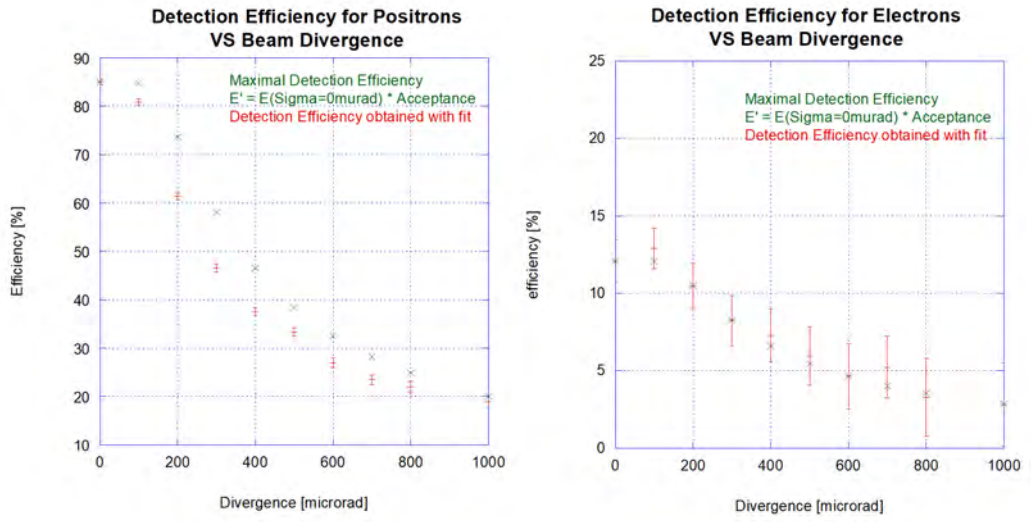

Figure 4.22. In green: Renormalized maximal detection efficiency VS beam divergence for positrons and electrons. In red, detection efficiency obtained with the fits for positrons and electrons. (Left panel): positrons $\mathcal{E}^{max}(\sigma')$. (Rigth panel): electrons $\mathcal{E}^{max}_{NoRech}(\sigma')$.

4.6 Positron channeling in the SHERPA at LNF setup

In this section we will try to simulate the images that the SHERPA TimePiX3 detector should see during a test at the LNF BTF facility with ∼500 MeV positrons. We will simulated different spot size and beam divergence along the bending coordinate x, and observe the obtained images in order to understand if the channeling peak will be visible enough to check the crystal alignment online. The divergence along the Y coordinate will be fixed at 300 μm.

In the present SHERPA setup there is no measurement of the incoming particle

direction and of the position impact point at the crystal surface. In fact, at so low energies, measuring the particle position introduces significant Multiple Scattering contribution on the particle direction. The direction information will then be in any case useless, because the particle will impact the crystal with an angle significantly different from the measured one. Moreover the fraction of particle in the Channeling angular acceptance will be reduced by the additional divergence introduced by the sensors, worsening the Channeling probability. Just to give an idea of the effect, using an 100 μm thick silicon sensor the multiple scattering contribution to the angle will be $\sim$900 μrad at the LNF energies, while for 400 GeV protons it is just 1 μrad. Moreover the size of the BTF experimental hall doesn't allow the distance in between crystal and the imaging sensor to be greater than $\sim$2-3 m.

Under this conditions the size of the beam spot at crystal position plays a crucial role in the capability of the experiment to observe the Channeling peak online. This aspect will be crucial when aligning the crystal with the beam.

To understand the limits on the spot size needed for SHERPA to work, a reconstruction of the coordinates of the particle at the TimePix3 plane has been introduced in the simulation. The aim of this procedure is to determine the position distribution of the particles after the interaction with the crystal.

To simulate the imaging obtained using the TimePix3 the histogram used to store the reconstructed coordinates has been mapped with the same geometry of the detector pixels, i.e. 256 bins in 14 mm on each coordinate. Figures 4.23 and 4.24 shows the results obtained for 2 m crystal to sensor distance (D), for the beam spot after the crystal and its X,Y projections.

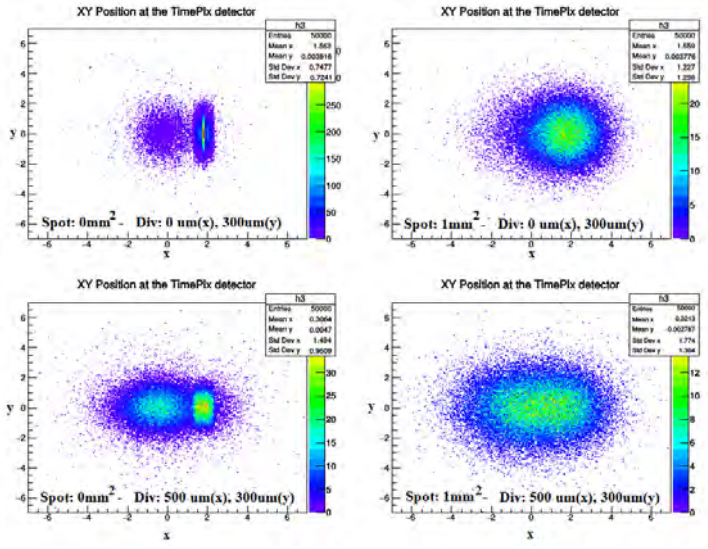

Figure 4.23. Beam spot at the TimePix3 plane for a detector to crystal distance of 2 m.

The first simulation was carried out using different beam conditions. Each of the four plot is obtained using the following beam setup:

- Top Left: Point-like spot with no divergence $\sigma'(x) = 0$ μrad.

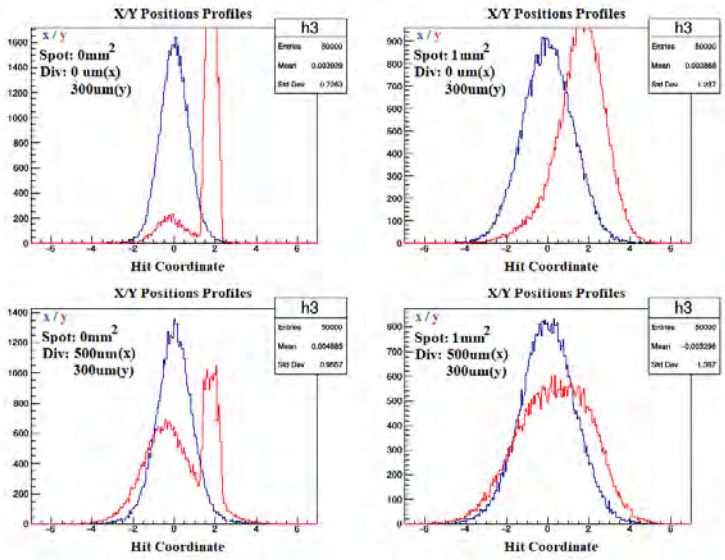

Figure 4.24. X-projection (in blue) and Y-projection (in red) of the beam spot at the TimePix3 plane for a detector to crystal distance of 2 m.

- Bottom Left: Point-like spot with $\sigma'(x) = 500$ μrad divergence.
- Top Right: Beam spot RMS size 1×1 mm^2 with divergence $\sigma'(x) = 0$ μrad.
- Bottom Right: Beam spot RMS size 1×1 mm^2 and divergence $\sigma'(x) = 500$ μrad.

It's clear that the crucial parameter is the beam spot. At short distances, just 2 m from the crystal, the channeling peak is barely visible for a beam with 500 μrad divergence and 1×1 mm^2 RMS beam spot. On the contrary if the spot size is very small the Channeling can be clearly observed even at short distance from the crystal.

To mitigate the effect of the spot size, we tried to move the detector 1 m downstream at 3 m from the crystal. Moving it further downstream wouldn't be realistic given the BTF hall dimensions constraints. Figures 4.25 and 4.26 shows the results of the 3 m distance simulation, respectively for the Beam-Spot and its X,Y projection. In this configuration the channeling peak can be identified even with a bean divergence of 500 μrad.

To simulate the effect of the beam optics, we also tried a configuration with higher values of angular divergence $\sigma'(x) = 800$ μrad, $\sigma'(x) = 1000$ μrad and smaller beam spot size of just 0.5 mm radius. This could be obtained by acting on quadrupoles of BTF. Figure 4.27 shows the results for the 2 m crystal to sensor distance simulation, respectively for the Beam-Spot and the X,Y projection of the Beam-Spot.

Figures 4.28 shows the results with the 3 m crystal to sensor distance simulation, respectively for the Beam-Spot and its X,Y projections.

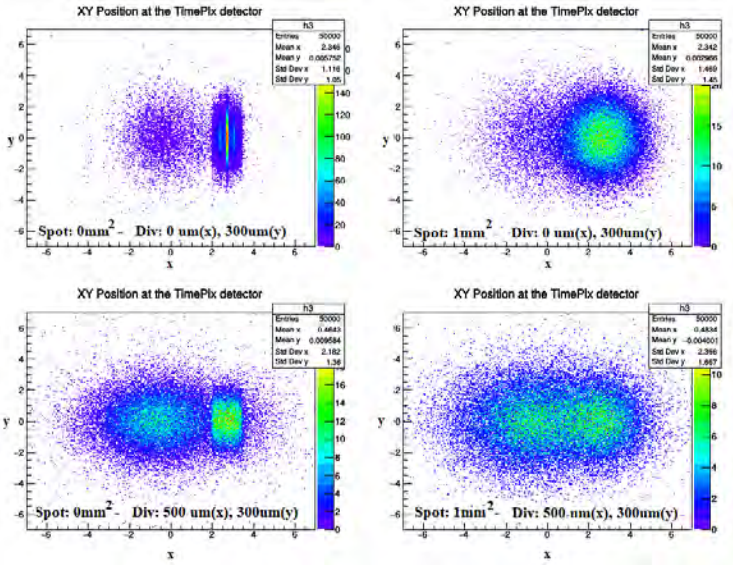

Figure 4.25. Beam spot at the TimePix3 plane for a detector to crystal distance of 3 m.

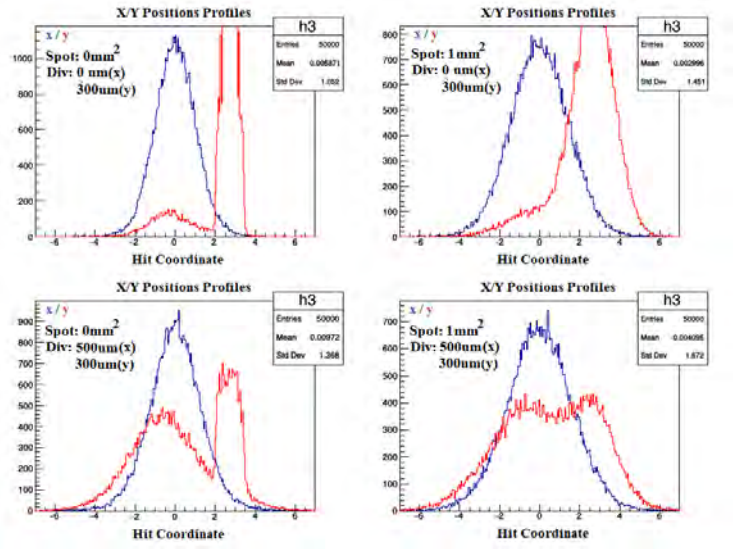

Figure 4.26. X-projection (in blue) and Y-projection (in red) of the beam spot at the TimePix3 plane for a detector to crystal distance of 2 m.

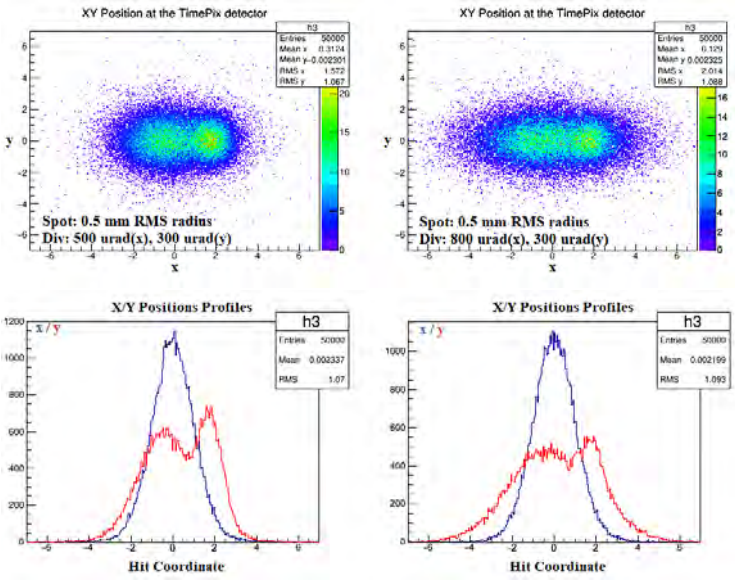

Figure 4.27. (Top): Beam spot at the TimePix3 plane and (Bottom): X-projection (in blue) and Y-projection (in red) of the beam spot at the TimePix3 plane. The detector to crystal distance is 2 m.

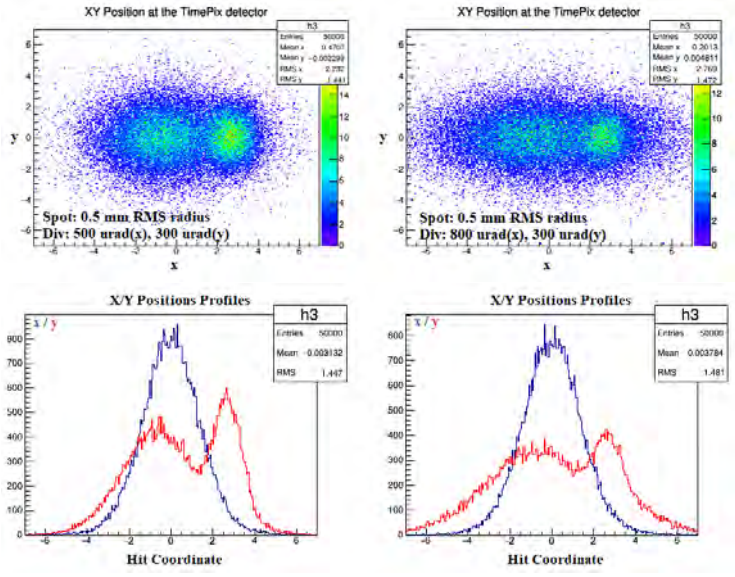

Figure 4.28. (Top): Beam spot at the TimePix3 plane and (Bottom): X-projection (in blue) and Y-projection (in red) of the beam spot at the TimePix3 plane. The detector to crystal distance is 3 m.

Chapter 5

Study of the TimePix3 Advacam Advapix detector

In this chapter I describe briefly a typical Pixel detector working principle and main characteristics. Then I'll focus on the ADVACAM AdvaPix camera, based on the Silicon Pixel detector TimePix3, and its characterization via radioactive sources performed at the Frascati National Laboratories. I'll finally describe some early test performed at BTF during the PADME test in beam December 2^{nd} 2021.

5.1 Silicon detector types

Before describing the TimePix3 silicon pixel sensor I'll give a short description of the drawbacks and the advantages of two of the most used types of Silicon detectors types:

- Double-Sided Silicon strip detectors (see Figure 5.1)
  Advantages: those detectors are sufficient in order to measure the x-y coordinates of the impinging particles.
  Drawbacks: due to their geometry, these detectors suffer from *ghost hits*. They also need a special insulation of the n-doped side. This configuration is very expensive, due to the lithographic process needed in order to build those detectors.

- Hybrid Pixel Silicon Detector (see Figure 5.2)
  Advantages: those detectors don't produce ghost hits. Due to the small pixel area and volume, the capacitance is very tiny (order of fF per pixel), the SNR is very high ($\approx 150:1$) and the leakage currents are very low if compared to the Double-Sided Silicon Detector, they are order of pA per pixel.
  Drawbacks: due to the high segmentation, the front-end electronics requires more power, there are more electrical connections and a large bandwidth is required.

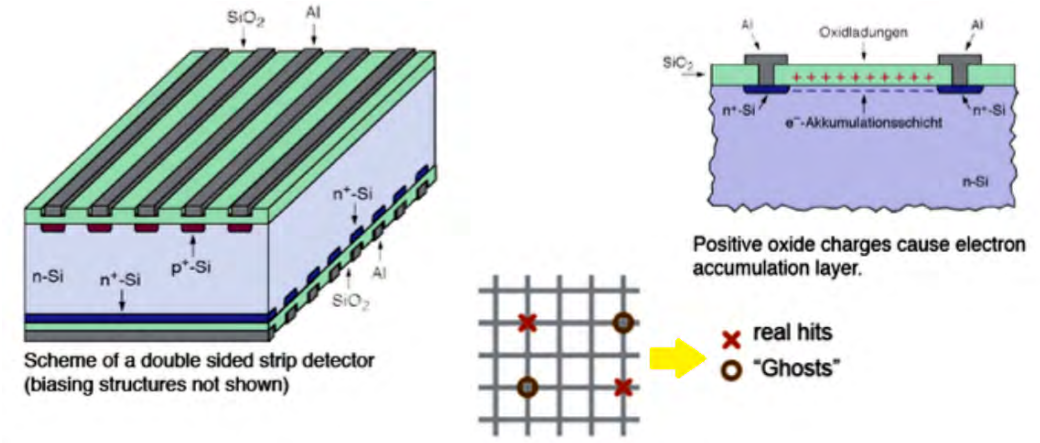

Figure 5.1. Double Sided Silicon Detector configuration.
On the left: perspective view of the detector. On the right, side view and *ghost hits* illustration.

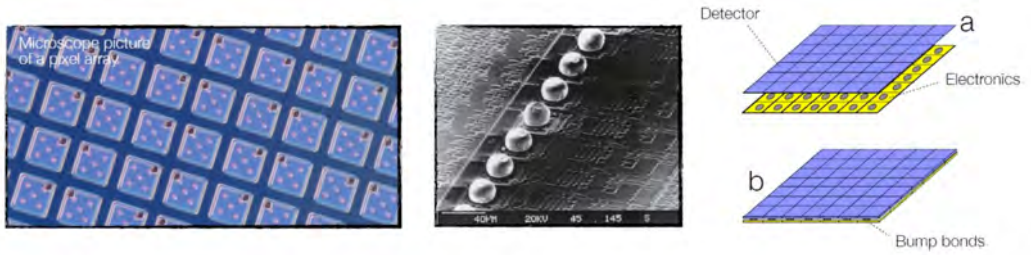

Figure 5.2. Hybrid Pixel Silicon Detector configuration.
On the left: microscope picture of a Pixel Array. On the center: SEM picture of solder connections. On the right: schematic diagram of the detector and front-end electronics

5.2 TimePix3 Silicon Pixel detector

The TimePix3 is a Hybrid Pixel Silicon Detector with an active area of 14×14 mm^2 and 100 μm thickness. The pixels are arranged in a 256×256 array of 55 μm-pitch squared pixels. The sensor and the camera are shown in Figure 5.3

Timepix3 is a general-purpose integrated circuit suitable for readout of both semiconductor detectors and gas-filled detectors. Compared to Timepix1 the circuit has more functionality, better time resolution and more advanced architecture for continuous sparse data readout with zero-suppression. In Fig. 5.4 the main characteristics of the two chips are compared.

Timepix3 can be used in a wide range of applications varying from X-rays imaging to particle track reconstruction. Depending on the application requirements user can choose one out of three data acquisition modes available in the Timepix3.
In the data driven mode both arrival time information and charge deposit information are sent off chip for each hit together with the coordinates of the active pixel. The chosen architecture allows for continuous and trigger-free readout of sparsely distributed data with the rate up to 40 Mhits/s/cm^2. For imaging applications and for calibrations the possibility exists of operating in frame-based (non-continuous)

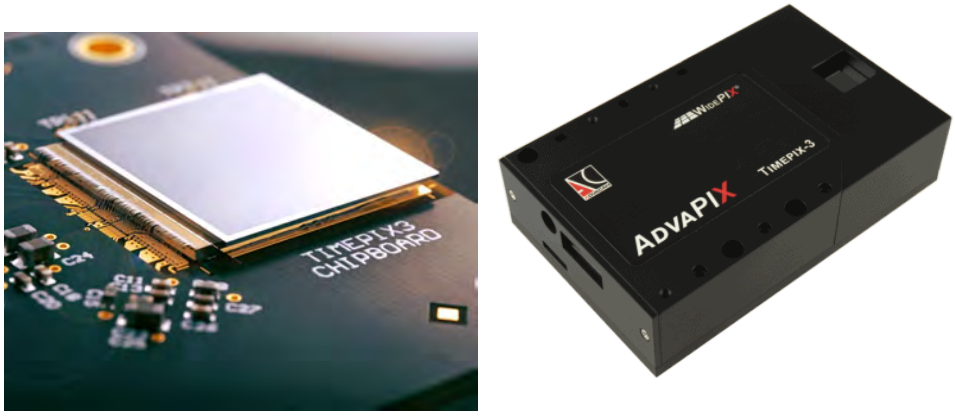

Figure 5.3. (a) TimePix3 Silicon chip die and (b) ADVACAM AdvaPix camera based on the TimePix3 detector.

data readout mode.
The module uses USB 3.0 communication channel, which assures a fast readout of the system and has a 10-pin socket through which can be triggered via external device. The TimePix3 chip has been used with different sensors material and thickness to optimize it's performance for different applications. The ionizing radiation particle

	Timepix (2006)	Timepix3 (2013)
Pixel arrangement	256 x 256	
Pixel size	55 x 55 µm²	
Technology	250nm CMOS - 6Metals	130nm CMOS - 8Metals
Acquisition modes	1) Charge (iTOT) 2) Time (TOA) 3) Event counting (PC)	1) Time (TOA) AND Charge (TOT) 2) Time (TOA) 3) Event counting (PC) AND integral charge (iTOT)
Readout Type	1) Full-Frame	1) Data driven (DD) 2) Frame (FB)
Zero suppressed readout	NO	YES
Dead time per pixel	> 300µs readout time of one frame	> 475ns ~600x Pulse measurement time + packet transfer time
Minimum timing resolution	10ns	1.562ns 6.4x
On-chip Power pulsing (PP)	NO	YES
Minimum detectable charge	~750e-	>500e- 1.5x
Output bandwidth	1 LVDS ≤200Mbps 32 CMOS ≤3.2Gbps	1 to 8 SLVS @640Mbps DDR ≤5.2Gbps 1.6x

Figure 5.4. Comparison of TimePix and TimePix3 main characteristics.

interacts with the sensor material creating an electric charge. This charge is collected by electric field and brought to pixel preamplifier where it is amplified and shaped forming triangular voltage pulse. The amplitude and duration of this pulse is proportional to energy deposited by particle within the pixel. The situation when the voltage pulse amplitude in particular pixel exceeds preselected threshold value is called "event" or "hit".
Each pixel contains three digital counters (10, 14 and 4 bits). These counters are

used differently according to measurement type and mode. There are four basic values which can be measured and stored in counters of each pixel:

- Number of events: number of events hits in the pixel during exposure time. This mode is suitable mainly for frame type readout.

- Time-over-Threshold (ToT): measured as number of periods of 40 MHz clock signal (25 ns step) when amplifier output signal stays over the energy threshold. The ToT can be transformed to energy in keV using per-pixel-calibration function. The coefficients for per-pixel-calibration are unique for each detector pixel and they are stored in configuration file delivered with device. The energy calibration is valid only for given values of other detector parameters as delivered in configuration file, especially threshold.

- Time-of-Arrival (ToA): number of periods of 40 MHz clock signal, or 25 ns step, from start of exposure until the event is registered by pixel , i.e. pulse in pixel crosses the threshold. The range is 409.6 μs. Additional 16 bits are added in FPGA in readout electronics so that the total range is 26.8 s. The additional bits are usable only if the pixel hit rate is below maximal value.

- Fast-Time-of-Arrival (FToA): time difference between event detection and next clock signal measured with step of 1.5625 ns. Range is 4 bits. The combination of ToA and FToA gives precise time of event detection in nanoseconds using the following formula:

$$Time[ns] = ToA \cdot 25 - FToA \cdot 1.5625$$

  ToA and FTOA are combined together by software. If saved then ToA and FToA are stored as separate items.

Instead, TimePix3 can do acquisition in two different manners:

- Frame type measurement
  No data is sent out of device during the exposure time. All measured events are accumulated in counters of pixels. Event counter is incremented and ToT is integrated for all events. The measured data is read-out after end of exposure time for all pixels with nonzero content. No measurement can be performed during readout process.

- Pixel type measurement
  Information about all hit pixels is read-out immediately and continuously during exposure time. If hit rate is below maximal value then there is virtually no deadtime.

All those features (for example: measuring mode and type, thresholds, polarizing bias, intensity levels of the pixels, file export, python scripting, external and internal trigger operation, etc...) can be easily set via PixetPro, the software that ADVACAM provides with its detectors.

5.3 Radioactive source characterization at LNF

In order to operate correctly the TimePix3, an accurate calibration process must be performed via radioactive sources. The most used low-intensity source available at Frascati National Laboratory is a pure β emitter ^{90}Sr source. Its decaying scheme is reported in Figure 5.5.

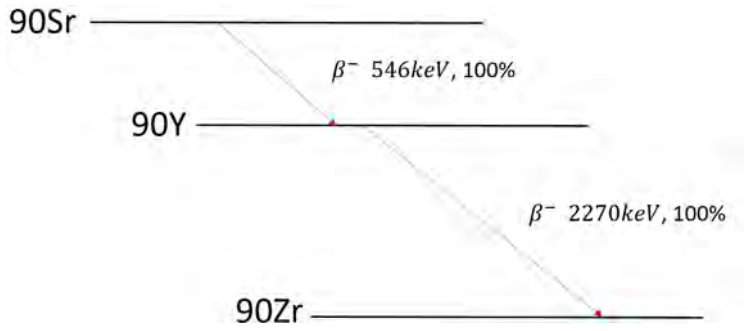

Figure 5.5. Decay chain of a typical ^{90}Sr radioactive source. The first β decay has an energy of 546 keV, the second β decay has an energy of 2270 keV.

The source used (ID number: E1345) has a proper half-lifetime of 28.6 years, with a measured activity of 3.7 MBq at 18 October 1996.
In order to increase the number of detectable particles, the radioactive source is put directly onto the Si active area of the detector. In the first configuration the distance between the source and the TimePix3 chip is ∼2 cm (see Figure 5.6a); then the surce is put at ∼10 cm from the sensor (see Figure 5.6b).

(a) First configuration. **(b)** Second configuration.

Figure 5.6. Two configurations used to make preliminary extimations of the number of detectable particles. The distance between the source and the TimePix3 chip is (a) ∼2 cm in the first configuration and (b) ∼10 cm in the second configuration.

From the layout, reported in Figure 5.7, the solid angle underlying the source in the two configurations can be estimated.

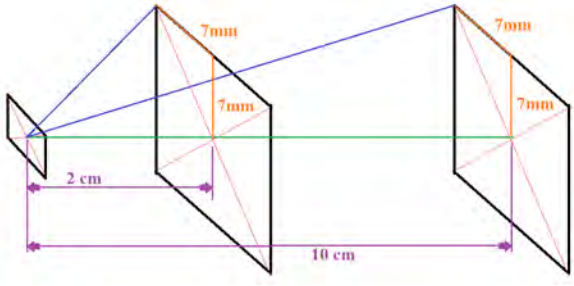

Figure 5.7. Layout of the two configurations. NOTE: the Figure is NOT to scale

The source is isotropic, so the ratio of the number of particles impinging on the TimePix3 in the first configuration with respect to the number of particles impinging on the TimePix3 in the second configuration can be evaluated simply by taking the ratio between the solid angles underlying those configurations.
The solid angle is defined as $\Omega = \frac{A}{d^2}$, where A is the area of the sensor and d is the maximal distance between the sensor and the radioactive source.
The ratio of the solid angle int the first configuration over the solid angle in the second one is the following:

$$\frac{\Omega_2}{\Omega_{10}} = \frac{\frac{A}{(d_2)^2}}{\frac{A}{(d_{10})^2}} = \frac{(d_{10})^2}{(d_2)^2} = \frac{(100\ mm)^2 + 2 \cdot (7\ mm)^2}{(20\ mm)^2 + 2 \cdot (7\ mm)^2} = \frac{10098\ mm^2}{498\ mm^2} = 20.27$$

So, assuming that the detector works in the same dynamical conditions and assuming isotropic emissions of radiation from the source; in the first configuration (Figure 5.6a) the number of detected particles is 20 times greater than the number of detected particles in the second configuration (Figure 5.6b). Due to this considerations, *all the data acquisitions will be performed with the first experimental setup (Figure 5.6a).*

The aim of this characterization is to perform multiple high-statistics acquisitions for different threshold values and different time-intervals for the acquisitions. With the PixetPro Software the detector threshold levels are set respectively to 1, 2, 3 and 4 eV. The time intervals Δt used to perform this characterization are set respectively to 10^{-2} s, 10^{-3} s, 10^{-4} s and 10^{-5} s. All the measurements are listed below: (1k stands for 1000, 10k for 10000)

- N° 1k DAQ; $\Delta t = 10^{-2}$ s, threshold = 1,2,3,4 eV
- N° 1k DAQ; $\Delta t = 10^{-3}$ s, threshold = 1,2,3,4 eV
- N° 1k DAQ; $\Delta t = 10^{-4}$ s, threshold = 1,2,3,4 eV
- N° 10k DAQ; $\Delta t = 10^{-5}$ s, threshold = 1,2,3,4 eV

Using the threshold scan functionality available in the software PixetPro we performed a threshold scan in order to establish the minimum value of the threshold allowing to collect zero pixel fired in absence of any radiation.

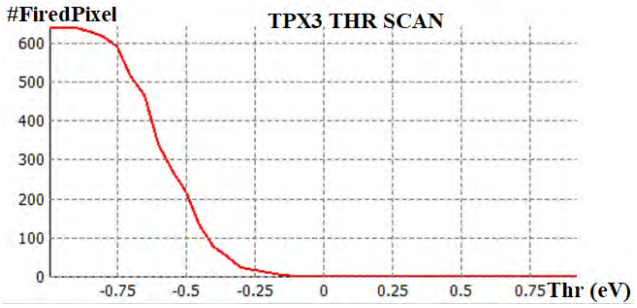

Figure 5.8. Threshold Scan. The TimePix3 PixetPro SW assumes 0 eV as -1 eV. The endpoint of the spectrum is 0 fired pixel because this characterization is not performed with radioactive sources.

The results of the scan are shown in Fig. 5.8. A threshold of 1 eV is sufficient to reduce the noisy pixels to zero.

After this first test we exposed the AdvaPix camera to the ^{90}Sr radioactive source, in order to observe the electrons produced by the beta decay. The results of the exposure are shown in Fig. 5.9 for two different values of the threshold. The higher threshold image shows less contribution from delta rays produced on the sensor surface, without spoiling the source image. In Fact given the thickness of the Silicon sensor, $\sim$100 μm, we expect an energy depositions of the order of 40 KeV from a MIP. (dE/dX=3.876 MeV/cm for Si [20]).

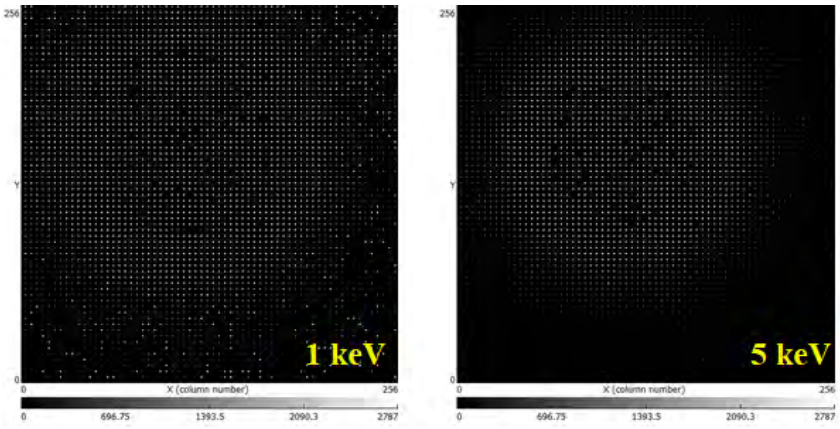

Figure 5.9. TimePix3 radioactive source characterization with 1 keV and 5 keV thresholds.

5.4 First results with positron beam at LNF

On December 2nd 2021, a preliminary test-beam was performed in order to asses the correct working condition for the detector while triggered.
During the previous week, the Beam Test Facility was reserved for the PADME Small Angle Calorimeter (SAC) calibration. In order to perform the first beam imaging with our ADVAPIX camera, we decided to share the beam-time with the PADME group. The Beam Test Facility line was operating in "parasitic" mode (and

thus the beam was optimized for DAΦNE operation). Electrons and positrons were both delivered to BTF, switching between the two charges every 30 minutes. The BTF staff measured a beam energy of ∼440 MeV.

The linac can provide 50 Hz of Single Particle bunches, but in order to check "by eye" the beam imaging in real-time on the ADVAPIX detector, the BTF trigger rate was pushed down to 1 Hz, and the BTF line was setup for Single Particle mode. In this regime, the probability to have n particles on target given the rate λ is given by the Poisson distribution.

$$\mathcal{P}_n(\lambda) = \frac{\lambda^n}{n!} e^{-\lambda}$$

The experimental setup was arranged just downstream the straight pipe exiting from the DHSTB002 dipole magnet, indicated in Fig. 5.10.

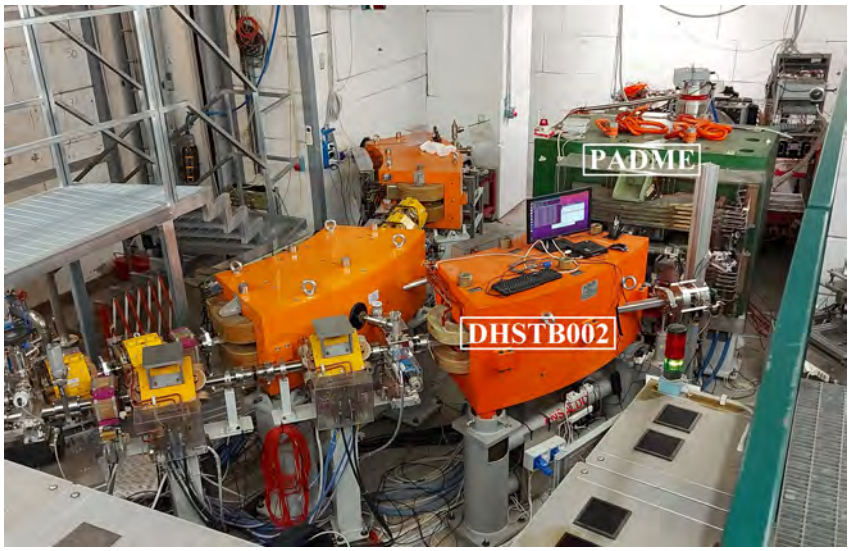

Figure 5.10. BTF hall configuration. The DHSTB002 magnet is off.

A FitPix detector was placed just downstream the straight vacuum tube exiting from DHSTB002. It is a Si pixel detector, quite similar to the our ADVAPIX camera described earlier. The PADME SAC and our ADVAPIX camera were placed ∼60 cm downstream the FitPix. The experimental setup is described in Fig. 5.11. The 50 Hz BTF trigger signal was connected directly to the ADVAPIX External trigger input.

After the beam alignment, performed with the PADME SAC center of gravity coordinate and refined using the ADVAPIX camera itself we started some acquisition tests. The image of the beam spot obtained with the FitPix and our ADVAPIX camera are shown in Figure 5.12.

The ADVAPIX recorded beam is broader with respect to the FitPix image because the FitPix is mounted on a 1 mm thick Aluminium plate, thus the impinging particles are subjected to Multiple Scattering. The MS angle on the FitPix and the Al plate can be estimated as [20]:

$$\theta_{0,Si}^{MS} = \frac{13.6\ MeV}{\beta cp} \cdot \sqrt{\frac{x}{X_0}} \approx 1.7\ mrad$$

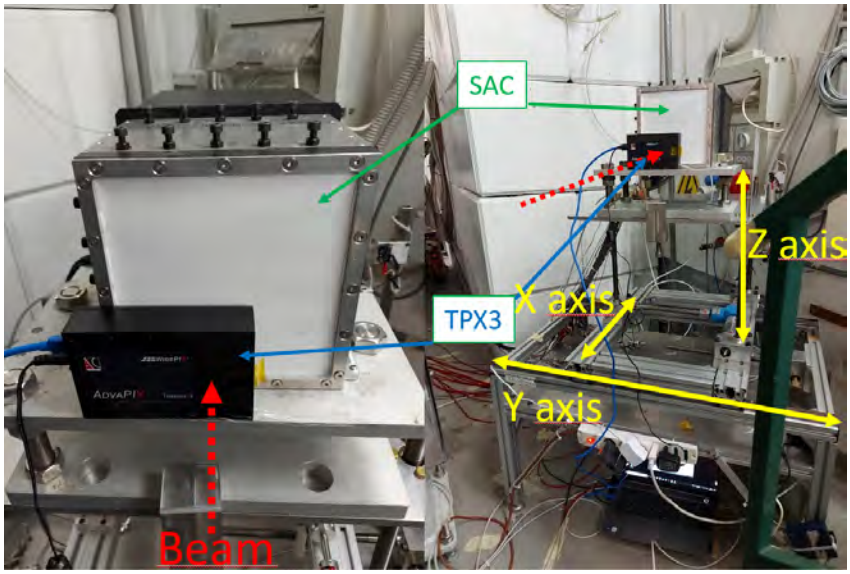

Figure 5.11. Experimental configuration of BTF on the preliminary test beam.

$$\theta_{0,Al}^{MS} = \frac{13.6\ MeV}{\beta cp} \cdot \sqrt{\frac{x}{X_0}} \approx 3.2\ mrad$$

where $X_0 = 9.7$ cm is the Si radiation length [20], $X_0 = 8.89$ cm is the Al radiation length [20], $p = \sqrt{E^2 - m^2}$ and $c = 1$ in natural units. The Multiple Scattering angle due to the FitPix and Aluminium plate is given by the sum in quadrature of the two contributions [20]:

$$\theta_{Si,Al}^{MS} = \sqrt{(\theta_{0,Si}^{MS})^2 + (\theta_{0,Al}^{MS})^2} \approx 3.7 mrad$$

And this explain why the imaged beam on TimePix3 is broader than the imaged beam on FitPix.

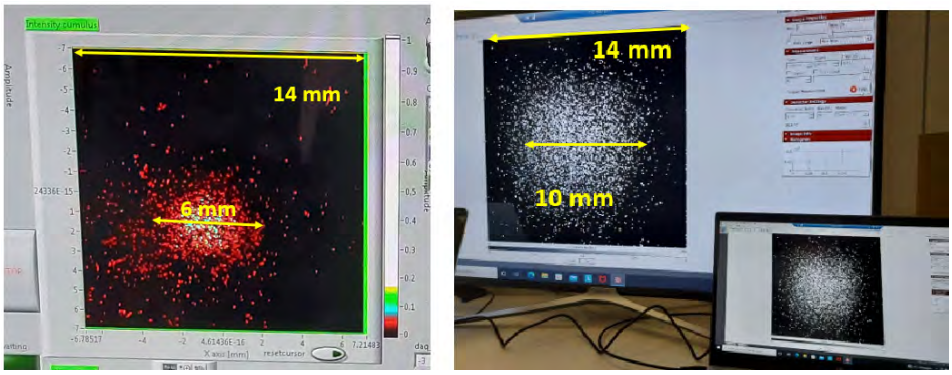

Figure 5.12. (Left): Beam spot imaged by the FitPix detector, 10cm downstream the endpoint of the vacuum pipe. (Right): Beam spot imaged by the TimePix3.

Being the acquisition trigger driven, the appearance of the image on the ADVAPIX monitor program was proving that the triggered acquisition mode was working properly and the detector was correctly synchronised with the beam bunches. The

data analysis on this first data acquisition, and the implementation of the online reconstruction software, will be performed in the following months, in preparation for MAMI and CERN test beams.

Chapter 6

Conclusions

In this thesis we have studied the reliability of the Geant4 release 10.05.p01 channeling routine, developed by Bagli et al. [3]. As a first step, we compared the Geant4 simulation results with different set of experimental data. The UA9 test with positron at H8 has been used to cross check the behaviour of the original example included in the Geant4 release for protons at high energies. After some modification to the original code we simulated the Mainz Mikrotron setup used by Mazzolari et al. [14] to study the channeling with low energy electrons. In this case we also compared the results with independent simulations obtained privately from Prof. V. Biryukov. We discovered an important discrepancy in between the Geant4 results and the simulations in [14]. The discrepancy is mostly due to the absence of the Rechanneling effect in the Geant4 implementation.

After this first phase of validation of the Geant4 routine, we started the study of the channeling of low energy positrons. This study is completely new and no data to compare with exist to date. For this reason we compared again our results with independent analytical calculation of Prof. V. Biryukov. In this case the agreement was found to be very good, to the level of few percent. This result was expected given the reduced importance of the Rechanneling effect for positrons with respect to the electron case.

Finally we used the simulation to study the capability of the SHERPA setup of observing channeling with positrons at ∼500 MeV at the DAΦNE Beam Test Facility at the INFN Laboratori Nazionali di Frascati. In particular we tried to assess limits on beam spot size and divergence to allow observation of the Channeling online during the crystal alignment procedure. After the Monte Carlo study we established that, with a crystal to sensor distance of ∼3m, the maximum X dimension for the beam spot size is ∼0.5mm RMS and the maximum X divergence is ∼500 μrad.
The dimension and divergence of the beam in the Y coordinate can exceed the previous values. These numbers seem to be from a first analysis in within reach for the BTF transport line. Further studies on how to tune the beam optics and the line to reach the SHERPA desired values will be in the future performed by the BTF staff.

In order to prepare the actual test beam for the channeling measurement at LNF with the bent crystal preliminary work has been made to setup the ADVAPIX detector which will be used in the SHERPA at BTF setup.

Appendix A

Figures of 511 MeV electrons and positrons simulations

In order not to make the discussion of Chapter 4 too heavy, the Figures showing the results of the simulations both with positrons and electrons are reported below. As said in Chapter 4, the simulations have been performed with difference divergence values and for each value the angular scan changing the crystal orientation has also been made. In order to reproduce the angular scan, we performed and extensive simulation campaign, changing the relative angle in between the crystal and the beam in the ranges form -500 μrad to +1500 μrad, in steps of 10 μrad. Each configuration of the simulations consist of 50000 events, both for positrons and electrons.

- Positrons Geant4 Channeling Simulations
  For σ'_x =0, 100, 200, 300, 400, 500, 600, 700, 800, 1000 μrad, the Deflection Angle Histogram and the Deflection Angle VS Crystal Orientation 2D-Plot are shown in Figure A.1, A.2, A.3, A.4, A.5, A.6, A.7, A.8, A.9, A.10, (a) and (b) respectively.

- Electrons Geant4 Channeling Simulations
  Forσ'_x =0, 100, 200, 300, 400, 500, 600, 700, 800, 1000 μrad, the Deflection Angle Histogram and the Deflection Angle VS Crystal Orientation 2D-Plot are shown in Figure A.11, A.12, A.13, A.14, A.15, A.16, A.17, A.18, A.19, A.20, (a) and (b) respectively.

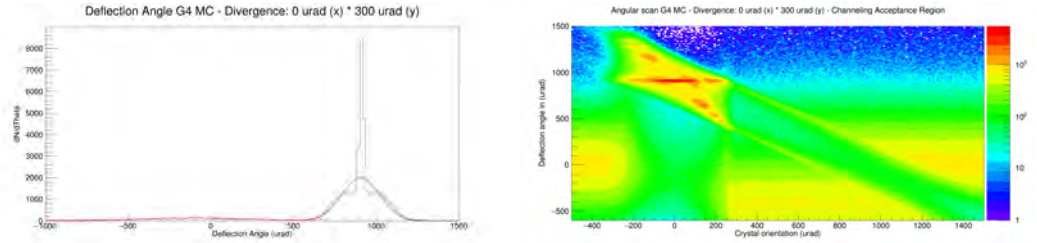

Figure A.1. (a) Deflection Angle Histogram and (b) 2D-Plot Deflection Angle VS Crystal orientation Angle. Simulation performed with $\sigma'_x = 0\ \mu rad$ and $\sigma'_y = 300\ \mu rad$ 511 MeV positron beam in SHERPA LNF BTF configuration.

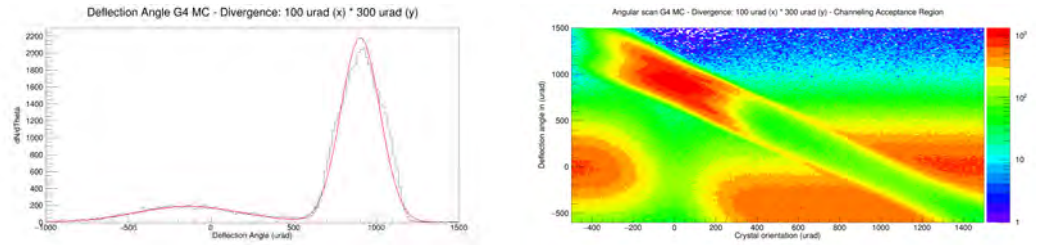

Figure A.2. (a) Deflection Angle Histogram and (b) 2D-Plot Deflection Angle VS Crystal orientation Angle. Simulation performed with $\sigma'_x = 100\ \mu rad$ and $\sigma'_y = 300\ \mu rad$ 511 MeV positron beam in SHERPA LNF BTF configuration.

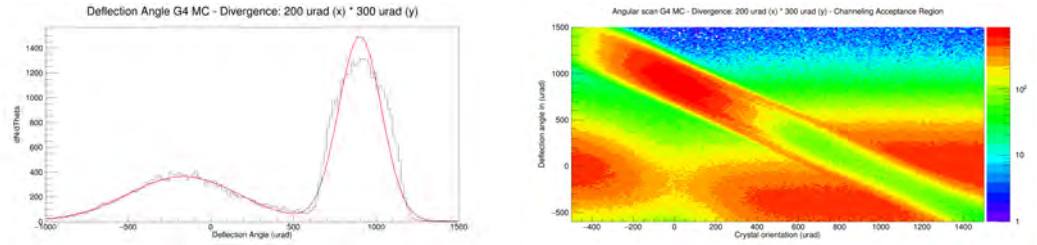

Figure A.3. (a) Deflection Angle Histogram and (b) 2D-Plot Deflection Angle VS Crystal orientation Angle. Simulation performed with $\sigma'_x = 200\ \mu rad$ and $\sigma'_y = 300\ \mu rad$ 511 MeV positron beam in SHERPA LNF BTF configuration.

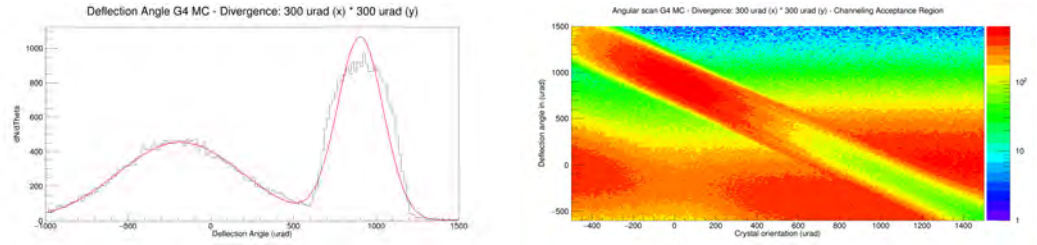

Figure A.4. (a) Deflection Angle Histogram and (b) 2D-Plot Deflection Angle VS Crystal orientation Angle. Simulation performed with $\sigma'_x = 300\ \mu rad$ and $\sigma'_y = 300\ \mu rad$ 511 MeV positron beam in SHERPA LNF BTF configuration.

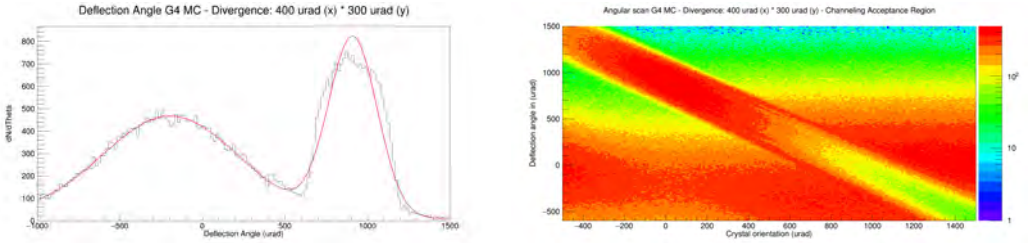

Figure A.5. (a) Deflection Angle Histogram and (b) 2D-Plot Deflection Angle VS Crystal orientation Angle. Simulation performed with $\sigma'_x = 400\ \mu rad$ and $\sigma'_y = 300\ \mu rad$ 511 MeV positron beam in SHERPA LNF BTF configuration.

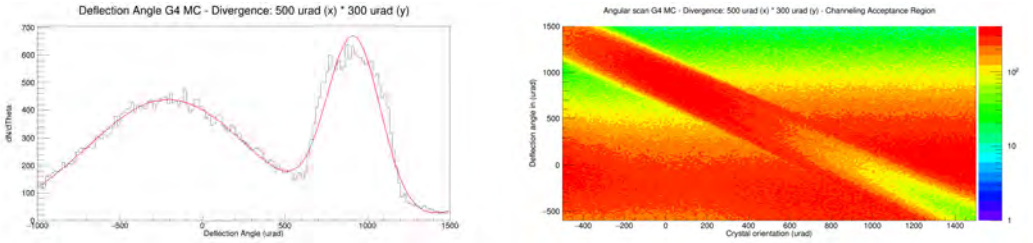

Figure A.6. (a) Deflection Angle Histogram and (b) 2D-Plot Deflection Angle VS Crystal orientation Angle. Simulation performed with $\sigma'_x = 500\ \mu rad$ and $\sigma'_y = 300\ \mu rad$ 511 MeV positron beam in SHERPA LNF BTF configuration.

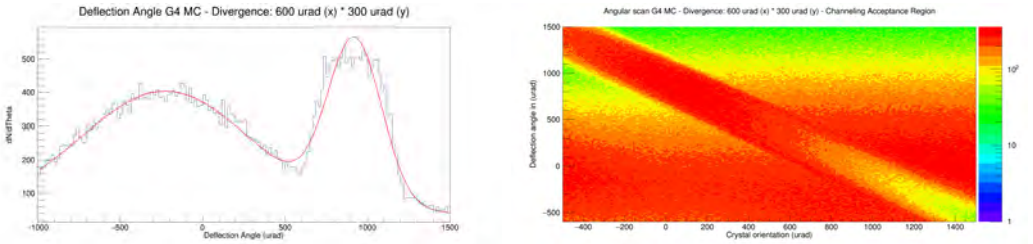

Figure A.7. (a) Deflection Angle Histogram and (b) 2D-Plot Deflection Angle VS Crystal orientation Angle. Simulation performed with $\sigma'_x = 600\ \mu rad$ and $\sigma'_y = 300\ \mu rad$ 511 MeV positron beam in SHERPA LNF BTF configuration.

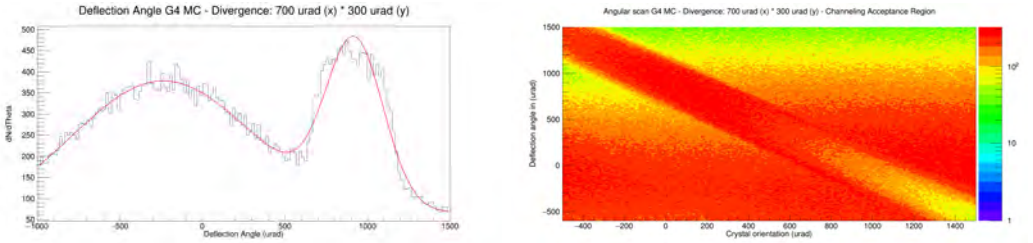

Figure A.8. (a) Deflection Angle Histogram and (b) 2D-Plot Deflection Angle VS Crystal orientation Angle. Simulation performed with $\sigma'_x = 700\ \mu rad$ and $\sigma'_y = 300\ \mu rad$ 511 MeV positron beam in SHERPA LNF BTF configuration.

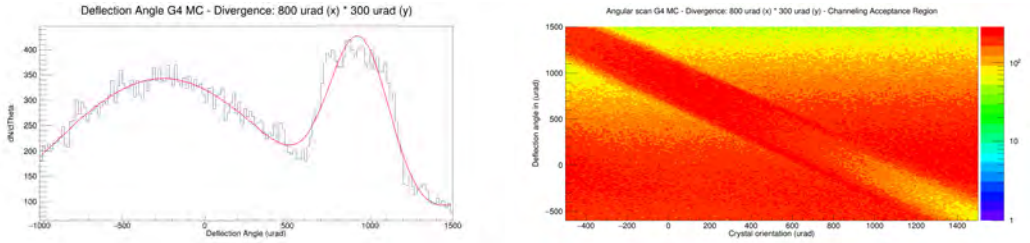

Figure A.9. (a) Deflection Angle Histogram and (b) 2D-Plot Deflection Angle VS Crystal orientation Angle. Simulation performed with $\sigma'_x = 800\ \mu rad$ and $\sigma'_y = 300\ \mu rad$ 511 MeV positron beam in SHERPA LNF BTF configuration.

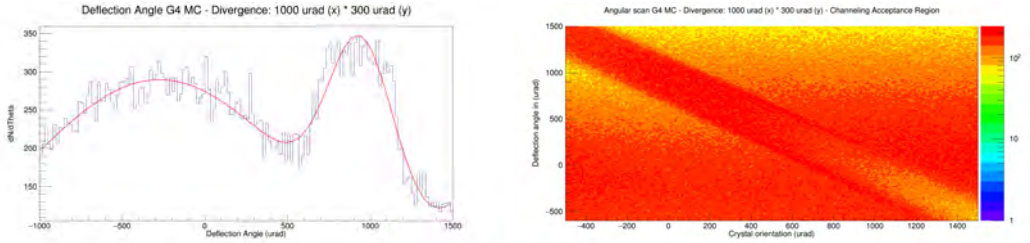

Figure A.10. (a) Deflection Angle Histogram and (b) 2D-Plot Deflection Angle VS Crystal orientation Angle. Simulation performed with $\sigma'_x = 1000\ \mu rad$ and $\sigma'_y = 300\ \mu rad$ 511 MeV positron beam in SHERPA LNF BTF configuration.

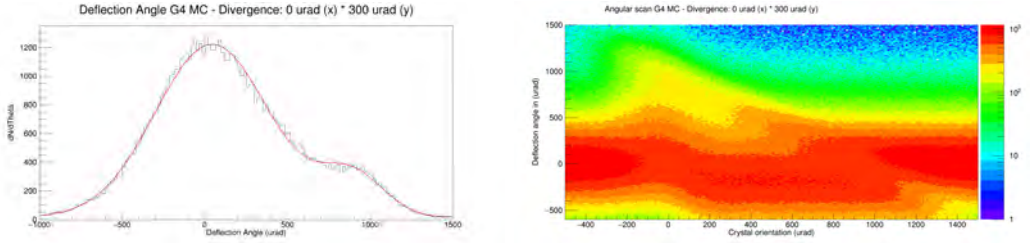

Figure A.11. (a)Deflection Angle Histogram and (b) 2D-Plot Deflection Angle VS Crystal orientation Angle. Simulation performed with $\sigma'_x = 0\ \mu rad$ and $\sigma'_y = 300\ \mu rad$ 511 MeV electron beam in SHERPA LNF BTF configuration.

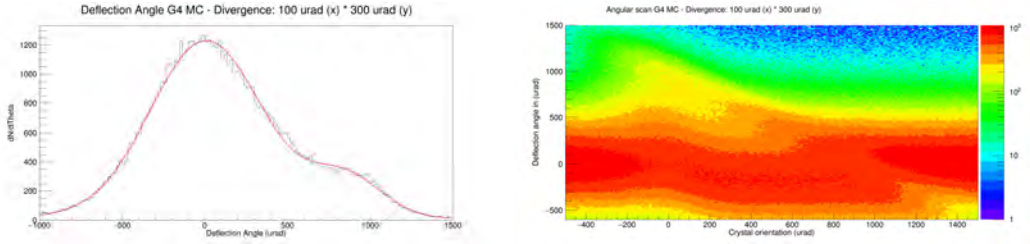

Figure A.12. (a) Deflection Angle Histogram and (b) 2D-Plot Deflection Angle VS Crystal orientation Angle. Simulation performed with $\sigma'_x = 100\ \mu rad$ and $\sigma'_y = 300\ \mu rad$ 511 MeV electron beam in SHERPA LNF BTF configuration.

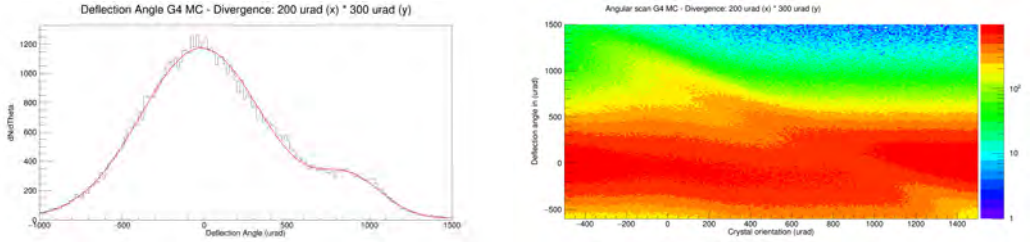

Figure A.13. (a) Deflection Angle Histogram and (b) 2D-Plot Deflection Angle VS Crystal orientation Angle. Simulation performed with $\sigma'_x = 200\ \mu rad$ and $\sigma'_y = 300\ \mu rad$ 511 MeV electron beam in SHERPA LNF BTF configuration.

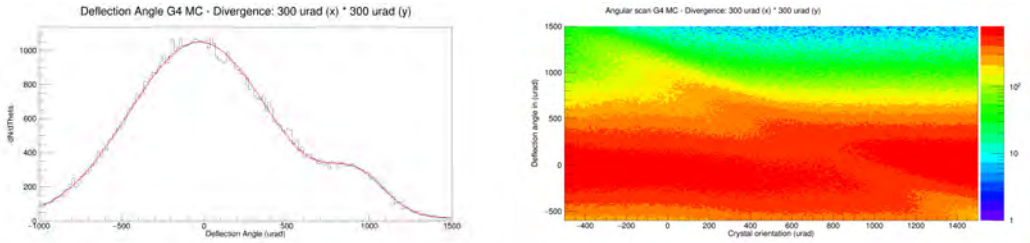

Figure A.14. (a) Deflection Angle Histogram and (b) 2D-Plot Deflection Angle VS Crystal orientation Angle. Simulation performed with $\sigma'_x = 300\ \mu rad$ and $\sigma'_y = 300\ \mu rad$ 511 MeV electron beam in SHERPA LNF BTF configuration.

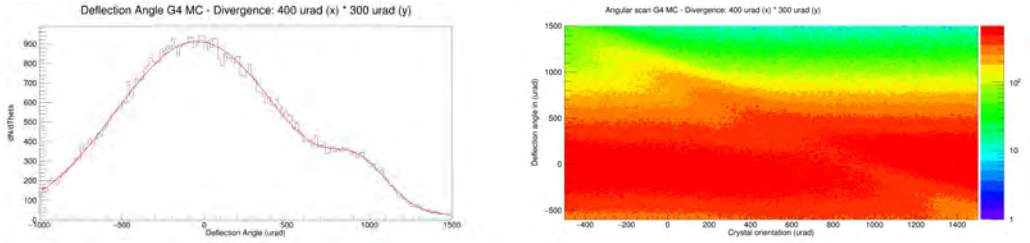

Figure A.15. (a) Deflection Angle Histogram and (b) 2D-Plot Deflection Angle VS Crystal orientation Angle. Simulation performed with $\sigma'_x = 400\ \mu rad$ and $\sigma'_y = 300\ \mu rad$ 511 MeV electron beam in SHERPA LNF BTF configuration.

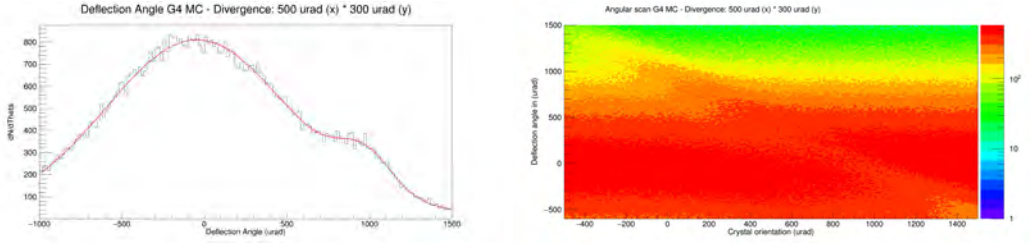

Figure A.16. (a) Deflection Angle Histogram and (b) 2D-Plot Deflection Angle VS Crystal orientation Angle. Simulation performed with $\sigma'_x = 500\ \mu rad$ and $\sigma'_y = 300\ \mu rad$ 511 MeV electron beam in SHERPA LNF BTF configuration.

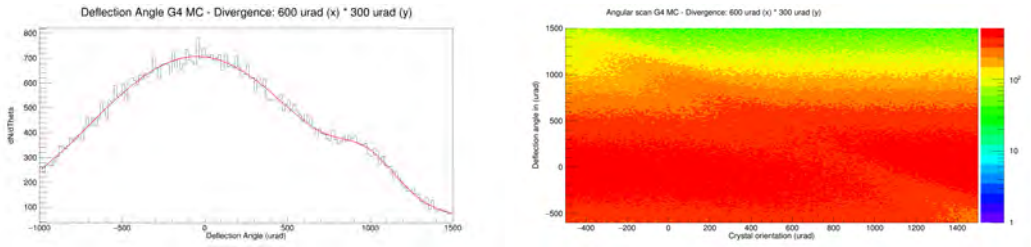

Figure A.17. (a) Deflection Angle Histogram and (b) 2D-Plot Deflection Angle VS Crystal orientation Angle. Simulation performed with $\sigma'_x = 600\ \mu rad$ and $\sigma'_y = 300\ \mu rad$ 511 MeV electron beam in SHERPA LNF BTF configuration.

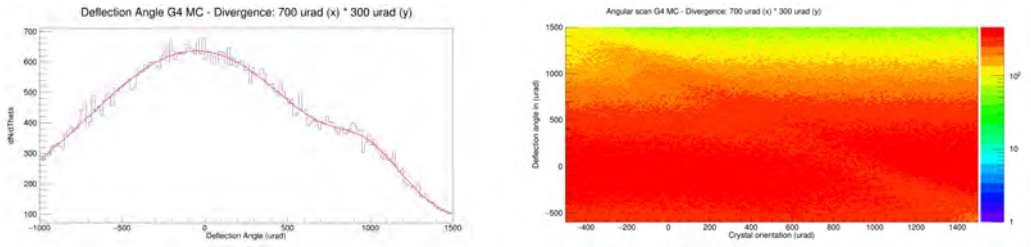

Figure A.18. (a) Deflection Angle Histogram and (b) 2D-Plot Deflection Angle VS Crystal orientation Angle. Simulation performed with $\sigma'_x = 700\ \mu rad$ and $\sigma'_y = 300\ \mu rad$ 511 MeV electron beam in SHERPA LNF BTF configuration.

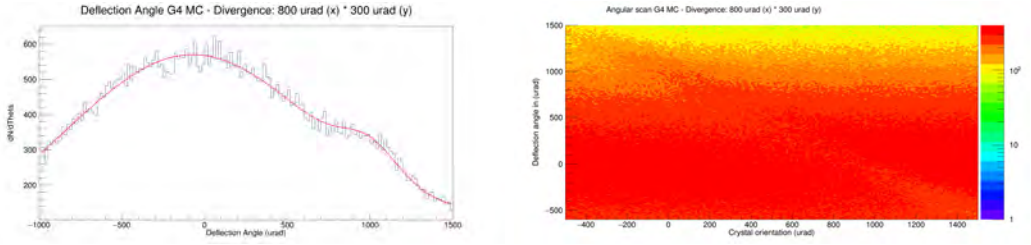

Figure A.19. (a) Deflection Angle Histogram and (b) 2D-Plot Deflection Angle VS Crystal orientation Angle. Simulation performed with $\sigma'_x = 800\ \mu rad$ and $\sigma'_y = 300\ \mu rad$ 511 MeV electron beam in SHERPA LNF BTF configuration.

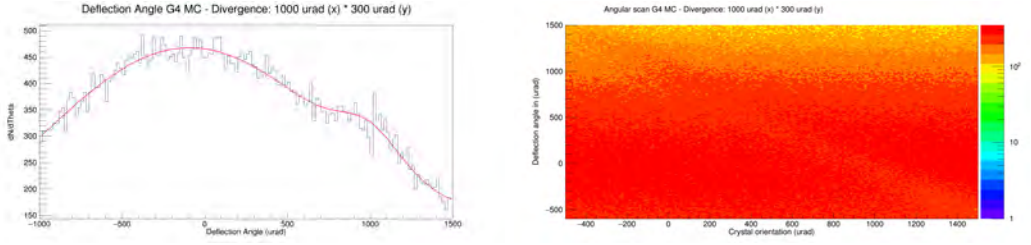

Figure A.20. (a) Deflection Angle Histogram and (a) 2D-Plot Deflection Angle VS Crystal orientation Angle. Simulation performed with $\sigma'_x = 1000\ \mu rad$ and $\sigma'_y = 300\ \mu rad$ 511 MeV electron beam in SHERPA LNF BTF configuration.

Bibliography

[1] Ashcroft, N. W. and Mermin, N. D. *Solid State Physics*. Holt-Saunders (1976).

[2] Bagli, E. Geant4 channeling [slides] (2014). Available from: https://agenda.infn.it/event/7409/contributions/67641/attachments/49055/58000/Bagli.pdf.

[3] Bagli, E., Asai, M., Brandt, D., Dotti, A., Guidi, V., and Wright, D. H. A model for the interaction of high-energy particles in straight and bent crystals implemented in geant4. *The European Physical Journal C*, **74** (2014). Available from: http://dx.doi.org/10.1140/epjc/s10052-014-2996-y, http://dx.doi.org/10.1140/epjc/s10052-014-2996-y doi:10.1140/epjc/s10052-014-2996-y.

[4] Barnes, M. J., Ducimetiére, L., Fowler, T., Senaj, V., and Sermeus, L. Injection and extraction magnets: kicker magnets (2011). http://arxiv.org/abs/1103.1583 arXiv:1103.1583.

[5] Biryukov, V. Computer simulation of beam steering by crystal channeling. *Phys. Rev. E*, **51** (1995), 3522. Available from: https://link.aps.org/doi/10.1103/PhysRevE.51.3522, http://dx.doi.org/10.1103/PhysRevE.51.3522 doi:10.1103/PhysRevE.51.3522.

[6] Biryukov, V. M. Catch 1.4 user's guide (2001). http://arxiv.org/abs/hep-ex/0110046 arXiv:hep-ex/0110046.

[7] Biryukov, V. M., Chesnokov, Y. A., and Kotov, V. I. *Crystal Channeling and Its Application at High-Energy Accelerators*. Springer-Verlag (1997).

[8] Buonomo, B., Di Giulio, C., Foggetta, L. G., and Valente, P. The Frascati LINAC Beam-Test Facility (BTF) Performance and Upgrades. In *5th International Beam Instrumentation Conference*, p. TUPG29 (2017). http://dx.doi.org/10.18429/JACoW-IBIC2016-TUPG29 doi:10.18429/JACoW-IBIC2016-TUPG29.

[9] Buonomo, B., Foggetta, L. G., and Piermarini, G. New Gun Implementation and Performance of the DAΦNE LINAC. In *6th International Particle Accelerator Conference*, p. TUPWA056 (2015). http://dx.doi.org/10.18429/JACoW-IPAC2015-TUPWA056 doi:10.18429/JACoW-IPAC2015-TUPWA056.

[10] Garattini, M., Annucci, D., Blanco-Garcia, O. R., Gianotti, P., Guiducci, S., Liedl, A., Raggi, M., and Valente, P. Crystal slow extraction of positrons from dafne: the sherpa project (2021). http://arxiv.org/abs/2110.02816 arXiv:2110.02816.

[11] Jim, A. Mmaps: Missing-mass a-prime search. *EPJ Web Conf.*, **142** (2017), 01001. Available from: https://doi.org/10.1051/epjconf/201714201001, http://dx.doi.org/10.1051/epjconf/201714201001 doi:10.1051/epjconf/201714201001.

[12] Leonardi, E., Kozhuharov, V., Raggi, M., and Valente, P. GEANT4-based full simulation of the PADME experiment at the DA{*upPhi*NE BTF. *Journal of Physics: Conference Series*, **898** (2017), 042025. Available from: https://doi.org/10.1088/1742-6596/898/4/042025, http://dx.doi.org/10.1088/1742-6596/898/4/042025 doi:10.1088/1742-6596/898/4/042025.

[13] Lietti, D., Berra, A., Prest, M., and Vallazza, E. A microstrip silicon telescope for high performance particle tracking. *Nuclear Instruments and Methods in Physics Research Section A: Accelerators, Spectrometers, Detectors and Associated Equipment*, **729** (2013), 527. Available from: https://www.sciencedirect.com/science/article/pii/S0168900213010784, http://dx.doi.org/https://doi.org/10.1016/j.nima.2013.07.066 doi:https://doi.org/10.1016/j.nima.2013.07.066.

[14] Mazzolari, A., et al. Steering of a sub-gev electron beam through planar channeling enhanced by rechanneling. *Phys. Rev. Lett.*, **112** (2014), 135503. Available from: https://link.aps.org/doi/10.1103/PhysRevLett.112.135503, http://dx.doi.org/10.1103/PhysRevLett.112.135503 doi:10.1103/PhysRevLett.112.135503.

[15] Raggi, M., Kozhuharov, V., and Valente, P. The padme experiment at lnf (2015). http://arxiv.org/abs/1501.01867 arXiv:1501.01867.

[16] Rossi, R. Experimental assessment of crystal collimation at the large hadron collider (2018).

[17] Scandale, W. and Taratin, A. Channeling and volume reflection of high-energy charged particles in short bent crystals. crystal assisted collimation of the accelerator beam halo. *Physics Reports*, **815** (2019). http://dx.doi.org/10.1016/j.physrep.2019.04.003 doi:10.1016/j.physrep.2019.04.003.

[18] Sytov, A., et al. First design of a crystal-based extraction of 6 gev electrons for the desy ii booster synchrotron (2021). Available from: https://arxiv.org/abs/2110.10102, http://arxiv.org/abs/2110.10102 arXiv:2110.10102.

[19] Valente, P. Poseydon - converting the dafne collider into a double positron facility: a high duty-cycle pulse stretcher and a storage ring (2017). http://arxiv.org/abs/1711.06877 arXiv:1711.06877.

[20] Zyla, P. et al. Review of Particle Physics. *PTEP*, **2020** (2020), 083C01. http://dx.doi.org/10.1093/ptep/ptaa104 doi:10.1093/ptep/ptaa104.